

FUNCTIONALLY GRADED MARTENSITIC STAINLESS STEEL

Functionally Graded Martensitic Stainless Steel Obtained Through Partial
Decarburization

By

Sean Crawford, B. Eng.

A Thesis

Submitted to the School of Graduate Studies

In Partial Fulfillment of the Requirements

for the Degree

Masters of Applied Science

McMaster University

©Copyright by Sean Crawford, April 2011

Masters of Applied Science (2011)

(Department of Materials Science and Engineering)

McMaster University

Hamilton, Ontario

TITLE: Functionally Graded Martensitic Stainless Steel

AUTHOR: Sean Crawford, B. Eng.

SUPERVISOR: Dr. Hatem S. Zurob

NUMBER OF PAGES: xvi, 147

Abstract

Functionally graded materials offer a way of obtaining materials with superior properties. Decarburization has been used in other steels to create graded materials. These materials offer high strength and improved ductility when compared homogeneous materials of the same type. In this thesis, graded martensitic stainless steel was explored as a way to provide a very high strength material with medium ductility by partially decarburizing the materials. Different processing treatments were tried and the resulting materials characterized and mechanically tested to compare homogeneous and graded martensitic stainless steels. Mechanical testing demonstrated that decarburization has a positive effect on the tensile, rolling and Charpy impact properties. A model was also developed that attempted to capture the deformation behaviour of graded materials. Present data was not available to verify the models validity but the model was used to predict trends of how different gradients affect fracture stresses and strains. These trends were used in an attempt to find optimum carbon distributions and maximize strength or ductility, as examples.

Acknowledgements

This thesis would not have been possible without the support and guidance of my supervisor, Hatem Zurob. His ever present enthusiasm and willingness to help is the biggest reason for the completion of this work. From weekly meetings and seminars, Hatem ensures that all of his students have a solid background in their research topic and provides any necessary assistance in understanding any material that his students have questions with.

Bechir Chehab at Aperam provided guidance, ideas, and materials for this project. He provided valuable information about the materials, their processing and testing, without which this work would not have been possible. I would like to thank him for all of his help and guidance. I would also like to thank Bechir and Aperam for having me over to visit their plant facility in Isbergues, France. Their hospitality made my stay very comfortable and the knowledge of their staff was a great assistance in obtaining the impact results used in this thesis.

I would also like to thank Doug Culley, John Rodda, Ed McCaffery, Dr. Steve Koprach and Chris Butcher for their knowledge and expertise in the field. Without them many of the technical issues I had would not have been overcome and this work would not be completed. I would personally like to thank them, on behalf of all the graduate students, for taking the time out of their day to assist us with training and technical issues we may have had while performing experiments or analysis.

I am grateful to fellow students Damien Radisson, Md. Kashif Rehman, Brick Kung and Mark Wemekamp whose advice and support on this project helped overcome some key roadblocks in my research and also provided work and data of their own to help me with this project.

I would also like to thank my loving parents, Rod and Judy, and my brother Steve for their support during my Masters. Without them this would not have been possible. Their support and encouragement was a huge reason for me having the strength to finish writing this thesis.

Table of Contents

Abstract	iii
Acknowledgements	iv
List of Figures	ix
List of Tables	x
Chapter 1 Preface	1
1.1 Introduction	1
1.2 List of Acronyms	6
Chapter 2 Literature Review	7
2.1 Functionally Graded Materials	7
2.2 Martensitic Stainless Steel	13
2.3 Decarburization in the Fe-C System	26
2.3.1 Overview	26
2.3.2 Decarburization Methods	27
2.3.3 Case 1: $\alpha + \text{Fe}_3\text{C} \rightarrow \alpha$	28
2.3.4 Case 2: $\alpha + \gamma \rightarrow \alpha$	34
2.3.5 Case 3: $\gamma \rightarrow \alpha + \gamma \rightarrow \alpha$	35
2.3.6 Case 4: Decarburization of Austenite	40
2.3.7 Diffusion Profiles	41
2.3.8 Decarburization on Fe-M-C	42

Chapter 3	Experimental Procedure	45
3.1	Experimental	45
3.1.1	Material	46
3.1.2	Materials Processing	47
3.1.3	Microstructure Characterization	48
3.1.4	Tensile Testing	51
3.1.5	Cold Rolling	53
Chapter 4	Results	55
4.1	Characterization	55
4.1.1	0.13% Carbon (MA1)	55
4.1.2	Higher Carbon Content Grades	61
4.1.3	Transmission Electron Microscopy	66
4.2	Tensile Testing	68
4.2.1	Lower Carbon Grade (MA1)	69
4.2.2	Higher Carbon Grades	74
4.3	Rolling	82
4.4	Charpy Impact Testing	83
Chapter 5	Discussion	91
5.1	Characterization	91
5.2	Tensile Testing	94
5.3	Rolling	99
5.4	Charpy Impact	101
5.5	Model	103

5.5.1 Sharp Interface	106
5.5.2 Continuous Profile	114
5.5.3 Results and Discussion	121
Chapter 6 Conclusions and Future Work	138
6.1 Conclusions	138
6.2 Future Work	141

Table of Figures

2.1	“Banana Chart” of steel Ductility versus Strength	8
2.2	(a) shows a gradual change in microstructure while (b) is the sharp interface microstructure	10
2.3	(a) stress-strain curve for spherodite and CGM spherodite, (b) stress-strain curve for pearlite and CGM pearlite., (c) Micrograph of CGM spherodite showing a gradual transition zone, (d) CGM Pearlite micrograph with gradual transition from pearlite to ferrite	11
2.4	Engineering stress-strain curve comparing a martensitic steel and decarburized steel	12
2.5	Diagram that shows how Chromium content closes off the austenite loop in stainless steel	13
2.6	Phase Diagram of a martensitic steel with 16%Cr, 2% Ni	14
2.7	0.05%C Phase Diagram as a function of %Cr	15
2.8	0.1% Phase Diagram as a function of %Cr	15
2.9	0.1% Phase Diagram as a function of %Cr	15
2.10	Plot of Vickers hardness versus austenitizing temperature in two Fe-Cr-C alloys .	17

2.11 Amount of retained austenite present after quenching as a function of austenitizing temperature in Fe-Cr-C steels	18
2.12 TEM microscopy (Bright and Dark Field) and diffraction patterns of a Fe-Cr-C steel	19
2.13 Plots that show hardness of a quenched martensitic steel is dependent on the austenitizing temperature, with a clear maximum at a certain temperature that is dependent on carbon content	21
2.14 Plots of the average grain size of austenite that results as a function of heating temperature	22
2.15 Plot of yield strength as a function austenite grain diameter at various testing temperatures	22
2.16 Relates the percentage of carbides formed as a function of heating temperature. At a carbon content of 0.45%C the optimum temperature is 1393 K and at a carbon content of 0.3%C the optimum temperature to austenitize at, in terms of carbide formation is 1423K	23
2.17 Phase diagram labeling the four different cases of decarburization in Fe-C alloys	24
2.18 Carbon profiles of the four decarburization cases in an Fe-C alloy	39
2.19 Local equilibrium with partitioning assumption in Fe-M-C system	40

2.20	Local equilibrium, no partitioning assumption in Fe-M-C system	41
2.21	Para-equilibrium assumption in Fe-M-C system	42
3.1	Details the dimensions of 2 different tensile samples used and how it was cut for metallographic analysis	51
4.1	Vickers hardness vs. austenitization times for MA1 material	54
4.2	How quenching media affects the microhardness of the quenched material in MA1 alloy	55
4.3	Micrographs of a sample austenitized for 5 minutes. (a) is the centre of the sample and (b) for the edge of the sample	56
4.4	(a) Microhardness profiles of 3 decarburized samples under different conditions, (b) Optical micrograph of the centre of a sample decarburized for 15 minutes, (c) Edge of the same sample showing growth of ferrite grains	57
4.5	(a) Microhardness profile of an austenitized (homogeneous) MA3 sample and decarburized (graded) sample, (b) and (c) were both etched with Kalling's Reagent. (b) is the core and (c) is the edge of the decarburized sample	59
4.6	Microhardness profile of an MA3 samples that were quenched in oil	60
4.7	(a) GDOES profile with microhardness profile superimposed over it [28], (b) Core of the GDOES sample, (c) Surface of the GDOES sample	

4.8	(a) Core of MA4 graded and (b) Surface of MA4 graded	63
4.9	(a) and (b) are TEM micrographs of the MA3 sample showing carbide formations and twinning	64
4.10	(a) and (b) are TEM micrographs of the MA4 sample showing twinning. No retained austenite was observed	65
4.11	(a) Tensile curves comparing austenitizing times of 5 and 10 minutes, (b) and (c) are the fracture surfaces of the tensile samples for austenitizing times of 5 and 10 minutes, respectively	67
4.12	(a) 5 min. austenitization vs. decarburization, (b) 10 min. austenitization vs. Decarburization, (c) 15 min wet H ₂ decarb, 5 min. re-austenitization and (d)10 min wet H ₂ decarburized fracture surfaces	69
4.13	(a) Tensile curves comparing graded, polished and as- quenched samples, (b) Graded, (c) Polished (1620x mag.), (d) Oil Quenched (1550x mag.)	70
4.14	(a)Tensile curves comparing homogeneous MA3 alloy to graded MA3 under 2 different decarburizing conditions , (b) Micrograph of the microstructure of a typical MA3 air quenched sample, (c) Micrograph of the tensile sample fracture surface (3240x)	72
4.15	Tensile curves for the MA3 homogeneous and graded oil quenched samples	73

4.16 (a) Stress-strain curves for air quenched MA4 homogeneous and graded material, (b) Typical fracture surface of homogeneous and core of graded samples, (c) Fracture surface of the edge of the graded sample	75
4.17 Tensile curves for MA4 oil quenched samples	77
4.18 (a) and (b) are SEM images of the rolled MA1 samples at 1200x and 9600x magnification, respectively	79
4.19 Microhardness vs. deformation plot of homogeneous MA1 cold rolled to a high strain	80
4.20 Microhardness profiles of the MA1 Charpy impact samples	83
4.21 Microhardness profiles of the MA3 Charpy impact samples	83
4.22 (a) MA1 austenitized, (b) MA1 H ₂ Decarburized 15 min austenitized 5 mins 1000°C centre, (c) MA1 H ₂ decarburized 15 min austenitized 5 mins 1000°C edge, (d)MA1 H ₂ decarburized 30 mins 1000°C centre, (e) MA1 H ₂ decarburized 30 mins 1000°C edge	84
4.23 (a) aust 5min 1000C, (b) MA1 H ₂ decarburized for 15 mins at 1000°C aust. 5 min 1000°C core, (c) MA1 H ₂ decarburized for 15 mins at 1000°C aust. 5 min 1000°C surface, (d) MA1 H ₂ Decarb 30 mins core (e) MA1 H ₂ decarb 30 mins surface .	85
4.24 (a) aust 5min 1000°C, (b) MA1 H ₂ decarburized for 15 mins at 1000°C aust. 5 min	

1000°C core, (c) MA1 H ₂ decarburized for 15 mins at 1000°C aust. 5 min 1000°C Surface, (d) MA1 H ₂ decarb 30 mins. at 1000°C Core (e) MA1 H ₂ decarb 30 mins. at 1000°C surface	86
4.25 (a) MA3 Austenitized, (b) MA3 Decarburized 15 mins Aust. 5 mins, (c) MA3 Decarburized 30 mins	87
5.1 Quench crack in forged AISI 403 martensitic stainless steel	94
5.2 Phase diagram of the balance Fe-12.33%Cr-C system	101
5.3 (a) Sharp interface profile and (b) is an example of a continuous interface profile	103
5.4 (a) Surface crack completely contained within a ductile ferrite layer, (b) Surface crack extending through ferrite layer and into the brittle martensitic core	107
5.5 Schematic of how the offset method of calculating the yield stress of a material from its stress-strain curve works	114
5.6 (a) and (b) are schematics of two different decarburization regimes	116
5.7 Failure strain as a function of volume fraction of martensite for a sharp interface	121
5.8 Failure stress as a function of volume fraction of martensite, assuming a sharp interface profile	121
5.9 Absorbed energy at critical strain as a function of volume fraction of martensite	122

5.10 Absorbed energy at prescribed strain as a function of volume fraction of martensite	122
5.11 Carbon distributions of the different simulations run for a continuous profile	124
5.12 Fracture strain as a function of surface concentration for a continuous carbon distribution	125
5.13 Fracture stress as a function of fracture strain	126
5.14 Absorbed energy as a function of surface concentration for a continuous profile .	127
5.15 Fracture stress vs. fracture strain for the different surface concentrations modeled	127
5.16 Carbon distribution profile for $C_s = 0.2\%C$	128
5.17 Global stress vs. strain for the optimum carbon content	129
5.18 Fracture strain as a function of decarburization of width	130
5.19 Fracture stress as a function of decarburization width	131
5.20 Absorbed energy as a function of decarburization width	131
5.21 Failure strain as a function of the bulk carbon content	133
5.22 Failure stress as a function of the bulk carbon content	133

5.23 Absorbed energy as a function of the bulk carbon concentration 134

List of Tables

2.1 Shows how the hardening temperature affects hardness after the material has
been quenched 16

2.2 Martensite morphology expected based on carbon content, as calculated by
Thermo-Calc 20

2.3 Shows the compositions of the steels used in the studies 20

3.1 Typical values of alloying compositions in the MA grades provided from
Arcelor Mittal 44

4.1 Summarizes the fracture stress and strains of the MA1 material for different
austenitizing times 68

4.2 Summary of the results of cold-rolling oil quenched and air quenched
samples 79

4.3 Summary of the Charpy impact tests performed on homogeneous samples and
graded samples of the MA1 and MA3 alloys 81

5.1 List of values for constants used in the sharp interface profile 106

.

Chapter 1

Preface

1.1 Introduction

Materials engineers are constantly trying to develop materials that have high strength and high ductility. This is a central problem in materials science and new and exciting classes of materials have been and are being developed to meet the ever changing needs of modern engineering applications. For example, the recent development of Transformation Induced Plasticity (TRIP) and Twinning Induced Plasticity (TWIP) steels has made it possible to obtain materials with excellent ductility and moderate strength (~ 1 GPa) but these materials suffer from poor corrosion resistance [1]. In order to increase the strength further, that is beyond 1.5 GPa while maintaining a reasonable ductility, it is necessary to develop a new class of materials. Graded materials are non homogeneous materials in which the composition and/or properties vary in such a way as to produce combinations of

properties that could not be achieved through homogeneous/monolithic materials. In this work, the possibility of using graded martensitic stainless steels to develop ultrahigh strength steels with reasonable ductility is examined.

Historically, graded materials have involved a mixing of ceramics and metals. These graded materials were mostly used in thermal applications. Present research, however, is looking to extend this concept to steels. By controlling the carbon distribution within a material, its properties can be controlled and tailored to achieve a desired mechanical response. This is one of many ways to make a graded material, as heat treating and control of nitrogen distribution can also be used as methods to produce graded. This present work will look at how this can be achieved in three different classes of martensitic stainless steels, each with different bulk concentrations of carbon content.

In other areas of research adding alloying elements, such as Niobium [2], to martensitic steels has been explored as way to increase the ductility of the steels at room and cold temperatures. This approach has several drawbacks such as the formation of carbonitrides, which can be detrimental to material properties and the cost of the alloying elements. Industrially, the control of carbon content in steels is something that is cheaply and easily controlled through the process of decarburization. Decarburization allows for the removal of interstitial carbon from the surface of the material while still retaining the bulk carbon concentration, if done for short periods of time.

One of the issues that this work examined was whether the protective chromium oxide layer responsible for the corrosion resistance stainless steels prevented the diffusion of carbon from the bulk of material into the atmosphere. Another issue involved with decarburization is the temperature at which it is carried out. $M_{23}C_6$ can form if decarburization is carried out at lower temperatures. This has a negative effect on the properties of the steel in two ways. The first is that carbides are detrimental to the ductility of the material and the second is that the formation of carbides, chromium carbide in these grades of steel studied, pulls chromium out of solid solution. This has a negative impact the corrosion resistance of the material.

The purpose of this work is to investigate the processing and properties of graded martensitic steel. Three different alloys will be explored and a comparison between the homogenous steels and graded steels will be presented. Decarburization at high temperature was the mechanism that was used to achieve the desired carbon content gradient in the materials. The microstructures generally sought through decarburization were a layer of ferrite on the surface with a martensitic core. The core retains the high strength of the martensite while the ductile ferrite provides extra ductility during deformation.

Stainless steels are used in a wide variety of applications and as such are in high demand in many industries, especially the food, chemical, energy and automotive industries due to the high level of corrosion resistance required for these applications [17, 18]. The addition of chromium as an alloying element to the basic Fe-C alloy is what makes these alloys stainless. It does this by forming a protective

layer of chromia on the surface of the steel. This prevents further oxidation of the Iron beneath. The types of iron oxide that form in non-stainless alloys are wustite (FeO), hematite (Fe₂O₃) and magnetite (Fe₃O₄) are the main components of rust and are detrimental to the properties of an Fe based alloy. This is especially true of wustite. However, just adding Chromium during the steel making process is not enough. There is a threshold of 12 wt.% Cr that determines whether an alloy will be stainless. Any alloy with a bulk Chromium content of 10.5 wt.% or higher will be stainless. Another necessity for the formation of the protective Cr₂O₃ layer is the presence of oxygen. Without oxygen the layer will not form because the chromium will not oxidize.

This layer is also very resilient. It is impervious to water and other potentially corrosive agents. It will also instantaneously reform if the alloy is scratched on the surface, preventing further oxidation of the interior of the material [35]. Its stability is also the cause of concern for its eligibility as a graded material through the decarburization method. In non-stainless Fe alloys, decarburization is performed in a controlled atmosphere. The partial pressure of oxygen in this atmosphere can be controlled to levels below those of the formation of the three different types of iron oxides. However, chromium oxide is so stable that this level of oxygen control is not possible, even in controlled environments. Therefore, chromium oxide is always present on the surface of a stainless steel.

Martensitic stainless steel is very strong steel that does not achieve high levels of strain. It is commonly classified as a 400 series alloy in AISI naming convention.

The 400 series is a mixture of martensitic and ferritic stainless steels. These steels contain Carbon and Chromium as their main alloying elements, as well as manganese and small amounts of other alloying elements such as nickel, niobium and titanium. Their corrosion resistance and toughness are inferior to those of austenitic stainless steels but they are stronger.

1.2 List of Acronyms

FGM Functionally Graded Material

MA1 Martensitic Stainless Steel Alloy with 13 wt.% Chromium and 0.13 wt.% Carbon

MA3 Martensitic Stainless Steel Alloy with 13wt.% Chromium and 0.33 wt.% Carbon

MA4 Martensitic Stainless Steel Alloy with 13 wt.% Chromium and 0.44 wt.% Carbon

RD Rolling Direction

OM Optical Microscopy

SEM Scanning Electron Microscopy

TEM Transmission Electron Microscopy

EBSD Electron Back Scatter Diffraction

XRD X-Ray Diffraction

Chapter 2

Literature Review

2.1 Functionally Graded Materials

Compositionally graded materials are an interesting development and a new area of interest amongst steel researchers. These new materials allow for superior combinations of strength and ductility when compared to traditional high strength (HS) steels. The diagram in Figure 2.1 [2] offers some insight into why these new types of steels are so exciting to the materials science community. Figure 2.1 does not show graded materials, which typically have strength of over 1.5 GPa and ductility better than 10%. These new materials can fill an area on the chart that no other steel can.

In addition, martensitic stainless steels are attractive because of their lower cost when compared to austenitic stainless steels. While austenitic stainless steels

have a good combination of strength and ductility, as can be seen from Figure 2.1, the nickel added to the steel to achieve these properties is relatively expensive when compared to martensitic steels.

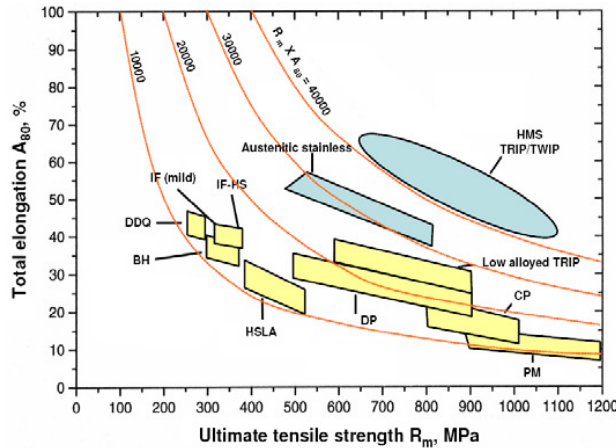


Figure 2.1- “Banana Chart” of steel Ductility versus Strength

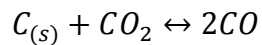
To combat this lack of ductility in martensitic steels partially decarburizing the material has been proposed by Chehab et al. [4]. This has been done in other steels, particularly in spheroidite and pearlite [5]. What makes stainless steel different from other grades of steel is the passivated chromia layer that forms on its surface. This is the reason why stainless steel is stainless but there is also a possibility that the protective layer could inhibit diffusion of carbon when gaseous decarburization is used. Fortunately, Cao [6] disproved this. Cao found “that at low temperatures Cr_2O_3 constitutes a barrier for carbon diffusion into the specimens” (Cao, 2003 pg. 65). However, at higher temperatures diffusion kinetics are so fast that this effect of diffusion inhibition is reduced.

A possible mechanism that allows for decarburization is proposed by

Adharapurapu et al. [44]. They describe a mechanism in which the carbon present in solid solution in the steel helps to reduce the chromia layer at the surface. The resulting oxygen then reacts with carbon to form CO because it is a highly favourable reaction. This mechanism would persist until the carbon content at the surface of the steel dropped below a certain level, at which point chromia forms again as it normally would.

The removal of carbon is the key to making the surface softer. This can be done in many ways but the fastest and cheapest is through using gases, primarily, wet hydrogen and CO/CO₂ atmospheres. The time of decarburization must not be long enough as to remove all the carbon or change the bulk carbon concentration in the middle of the sample, but must also be long enough to decarburize the sample to a certain depth in order to achieve the desired properties. The wet hydrogen method works by controlling the partial pressure of oxygen in the atmosphere [4]. In the correct range the partial pressure is low enough to not oxidize the iron but high enough to remove carbon from the sample.

The second method is much more popular, as it can be used to achieve any desired carbon content one wishes [3]. Using an atmosphere of CO and CO₂, any activity of carbon can be achieved by varying the ratio of CO to CO₂. This reaction follows LeChatelier's Principle, which is known from basic chemistry:



Increasing the amount CO pushes the reaction to the left and increases the carbon at the surface of the steel. Increasing the amount CO₂ pushes it the right and the reaction consumes carbon, which decreases the amount of carbon in the material.

The resulting microstructures of these graded materials can be classified in two categories. The first is a continuous, gradual change in microstructure and the second is a sharp interface with a very definitive boundary between the different phases in the material. The micrographs below are taken from Lefevre-Schlick, et al. [5]

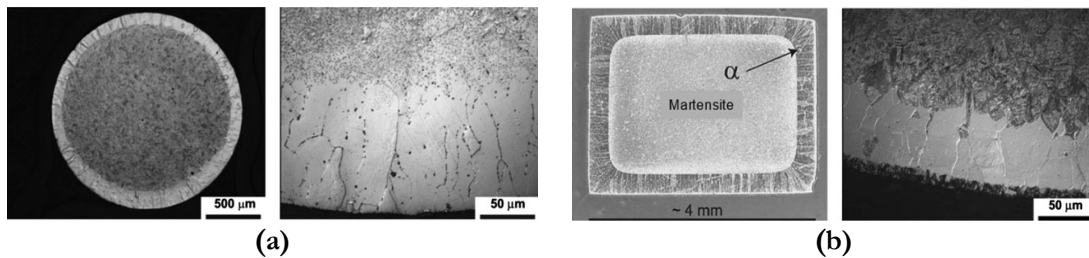


Figure 2.2 (a) shows a gradual change in microstructure while (b) is the sharp interface microstructure

Composite materials of this type can undergo two different types of failure modes, necking and fracture [4]. The necking failure mode cannot happen at only one part of the composite, as necking is a global phenomenon. Therefore, when dealing with necking as a failure mode, one must consider the bulk stress and work hardening rate of the material. Fracture on the other hand is different. Different parts of the material will have different stress concentrators or in the case of graded materials, different properties with different K_{IC} values. Therefore, fracture can initiate at the surface or in the core depending on impurities or cracks.

The mechanical properties of graded steels have been explored using an Fe-C alloy and 4340 grade steel, amongst others, which are shown below.

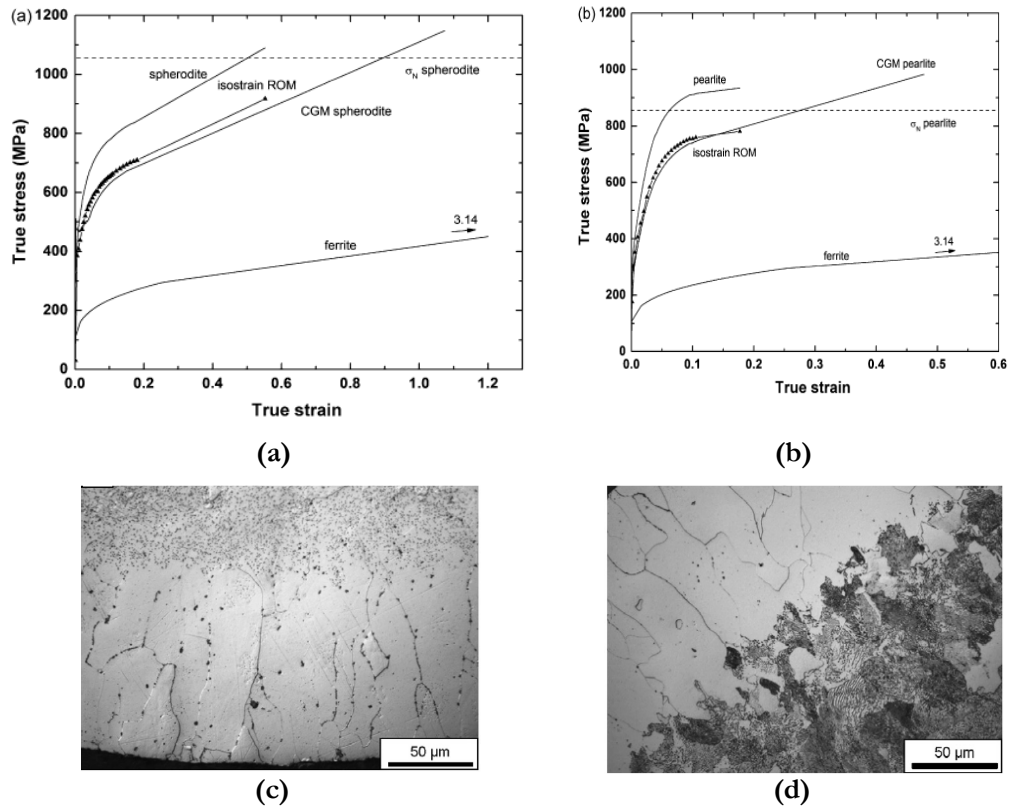


Figure 2.3 (a) stress-strain curve for spherodite and CGM spherodite, (b) stress-strain curve for pearlite and CGM pearlite., (c) Micrograph of CGM spherodite showing a gradual transition zone, (d) CGM Pearlite micrograph with gradual transition from pearlite to ferrite [5]

Figures 2.3 (a) and (b) are the stress-strain curves of the homogeneous and graded Fe-C alloys and resulting microstructures in the graded steels. Lefevre-Schlick prepared graded spherodite and pearlite samples and tested them against homogeneous samples of the same microstructures. The CGM materials perform much better than the homogeneous materials, specifically in terms of elongation but

not higher in over strength. This is due to the much greater elasto-plastic transition that occurs in the graded materials. Figures 2.3 (c) and (d) are the microstructures. Ferrite can be seen on the surface of both CGMs and both show a gradual interface between the phases.

Work done by Chehab et. al, [7] as seen in Figure 2.4, has shown a clear indication that decarburization does indeed have a positive effect on the tensile properties when comparing homogeneous and graded samples. The tensile curves below are for 43XX grade samples. The black curve is in the as-quenched condition, whereas the grey curve is the decarburized sample. The decarburized sample had a core carbon content of 0.4%C and a surface content of 0.1%C. This yielded an average carbon content of 0.26%C, which was then compared to a 4324 sample.

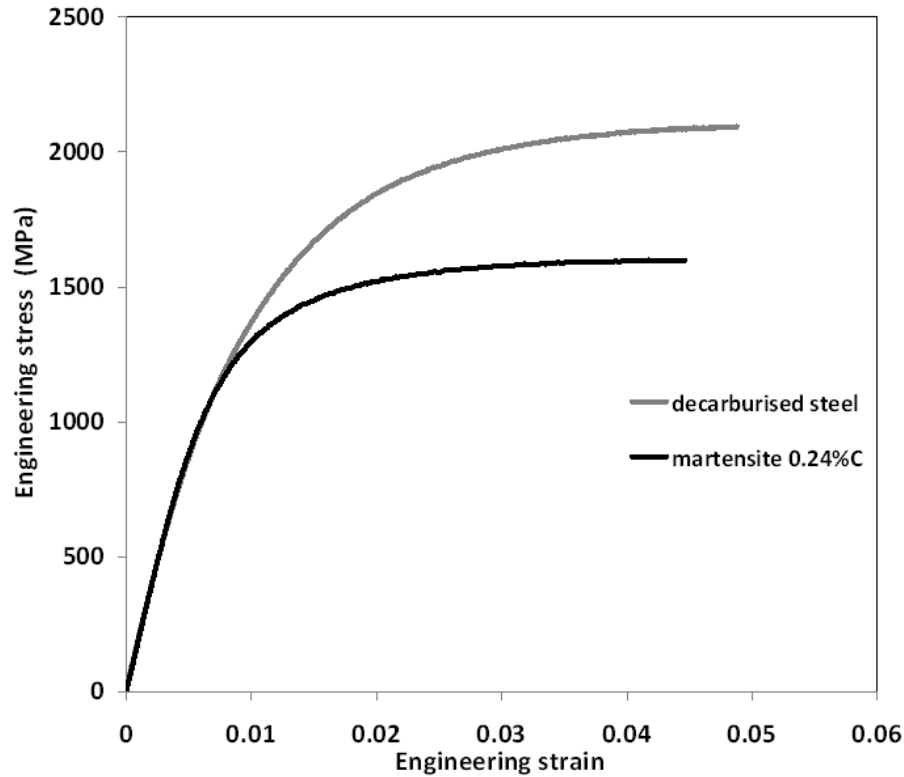


Figure 2.4- Engineering stress-strain curve comparing a martensitic steel and decarburized steel [8]

Former and current research by Bechir and Zurob are also exploring the development of martensite-bainite composite materials [8].

2.2 Martensitic Stainless Steel

There is extensive literature on martensitic stainless steels and their properties. Firstly, in order to achieve a fully martensitic structure, the steel must have austenite as a phase at high temperature. The size of this field is controlled by the alloying elements. The interest here is in how chromium controls the width of this field on the phase diagram, which is shown in Figure 2.5 [9]. Nitrogen and nickel also have a large impact on the size of the austenitic region of a steel and are of less concern in

this work.

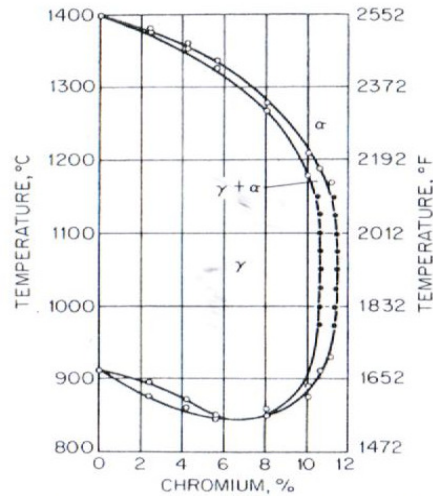


Figure 2.5- diagram that shows how Chromium content closes off the austenite loop in stainless steel [9]

Figure 2.6 [10] is a phase diagram for 16Cr+2Ni alloy as a function of wt.% C. It is of similar composition to the material studied in this work and can be used to infer what kinds of phases are possible in the range of carbon contents of interest, which are 0 to 0.44 wt.% C. From this diagram it can be seen that alpha ferrite, austenite and cementite can be expected to form at different temperatures. This will have a big effect on the type of heat treatment used, as some phases are more desirable than others, in terms of mechanical properties.

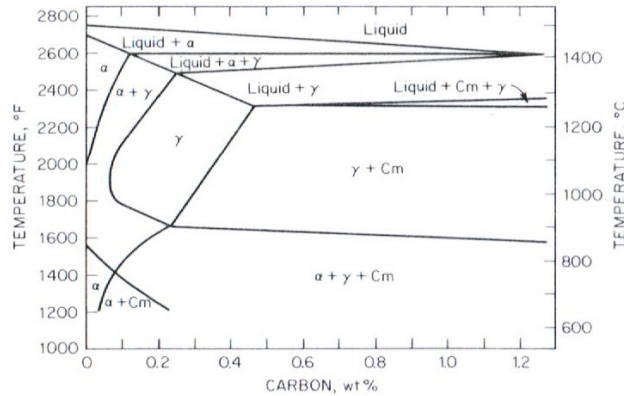


Figure 2.6- Phase Diagram of a martensitic steel with 16%Cr, 2% Ni

Figures 2.7, 2.8 and 2.9 [11] provide more realistic phase diagrams, with respect to the materials used in this study, and are for carbon contents of an Fe-Cr-C alloys at 0.05wt.%, 0.1wt.% and 0.2wt.% respectively. These diagrams show that the same phases are expected to be present in the steel at different temperatures but there is one key difference. Three different phases of carbides, namely Fe_3C , $(Fe,Cr)_{23}C_6$ and $(Fe,Cr)_7C_3$ are present depending on Cr and C wt.%. The effect these carbides have on steel and how processing parameters can be changed to avoid the formation of these carbides will be discussed later.

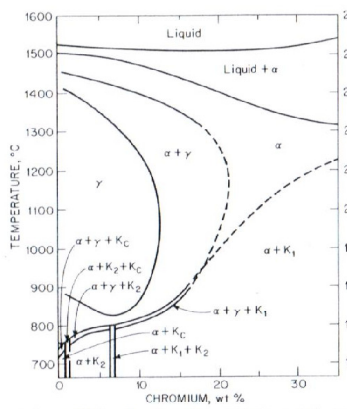


Figure 2.7- 0.05% C Phase

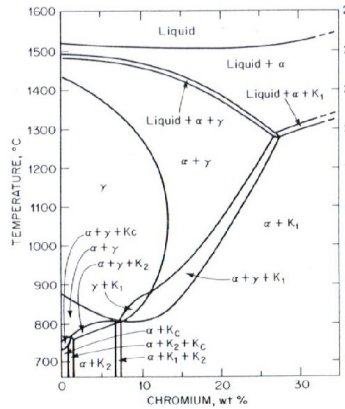


Figure 2.8- 0.1% C Phase

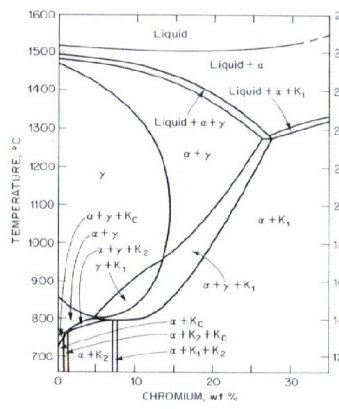


Figure 2.9- 0.2% C Phase

Diagram as a function of %Cr Diagram as a function of %Cr Diagram as a function of %Cr

Martensitic stainless steels can be strengthened in a number of ways. Strengthening is important to hardness and resistance to abrasion [12]. The most important strengthening mechanism, besides the martensitic transformation itself, is carbon content. It is common knowledge that increasing the amount of carbon in any steel generally increases its hardness and decreases its ductility. Table 2.1 [12] shows typical values of hardness for different martensitic stainless steels with varying carbon content. It can be seen from this table that carbon content increases the hardness of the steel. Other things such as heat treatment temperature, time and quenching medium all have an important impact on the hardness and general properties of the material and will be discussed in a later section.

Table 2.1 shows how the hardening temperature affects hardness after the material has been quenched [12]

Alloy AISI	Carbon %	Hardening temperature	As-quenched hardness, R _c
410	0.115	1700°F (927°C) ½ h	44
		1850°F (1010°C) ½ h	44.5
414	0.13	1700°F (927°C) ½ h	44
		1900°F (1038°C) ½ h	44
431	0.14	1700°F (927°C) ½ h	42
		1900°F (1038°C) ½ h	41
420	0.31	1700°F (927°C) ½ h	49
		1875°F (1024°C) ½ h	52
440C	1.0	1700°F (927°C) 1 h	52
		1900°F (1038°C) 2 h	55

The table also shows a levelling off in hardness above a certain carbon content. According to [12] this plateau is generally reached at a carbon content of around 0.6 wt.%C but can vary from grade to grade. It states “At this level, the austenite is saturated in carbon and further carbon is precipitated from the melt as primary carbides.” [12]. Many of the other elements that are added to martensitic stainless steels do not have the same cause and effect impact as carbon does. In other words, carbon is the only alloying element that directly increases the hardness of the steel. The other elements produce other effects, such as stabilizing a phase in the metal that causes the increase in hardness.

The microstructure of a material is very important to the properties of a material. In martensitic steels the carbon content of the steel has a strong effect on the type of martensite that is observed after quenching and, therefore, has a strong influence on the resulting properties. According to the Handbook of Stainless Steel [12] there are three classes of microstructures, which are low carbon, medium carbon and, high carbon martensitic steels. These classes have a needle-like structure, a very

fine needle-like structure and an ultra fine structure that contains primary carbides, respectively. The austenitizing temperature also has a big impact on the morphology of the martensite that forms upon quenching.

Figure 2.10 [13] demonstrates the effect of austenitizing temperature on the Vickers hardness of a Stainless steel. This graph shows decrease in the hardness of the material up until a temperature of around 1050°C. After this temperature there is a large drop off in the hardness because at higher temperatures the carbides dissolve back into the matrix and the pinning effects that these carbides have on controlling prior austenite grain growth is lost [13].

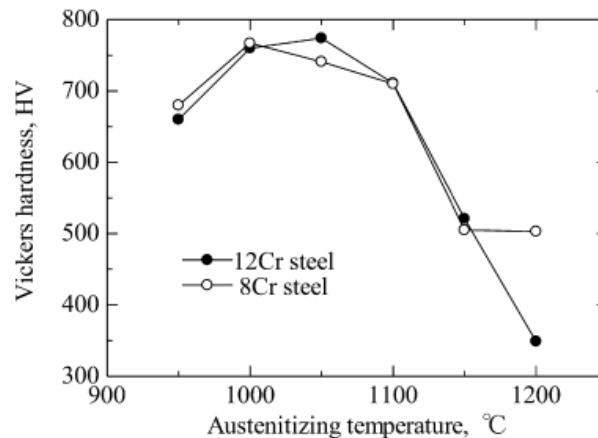


Figure 2.10 is a plot of Vickers hardness versus austenitizing temperature in two Fe-Cr-C alloys

The amount of retained austenite present after quenching, shown in Figure 2.11 [13] is also affected by the austenitizing temperature. At higher austenitizing temperatures, as was stated in the previous paragraph, carbides dissolve. This increases the wt.% of carbon in solid solution. Because martensitic start and finish (M_s and M_f , respectively) temperatures of steels are inversely proportional to the

amount of carbon in the material, this higher carbon content lowers the M_f temperature and all the retained austenite does not transform to martensite, upon quenching.

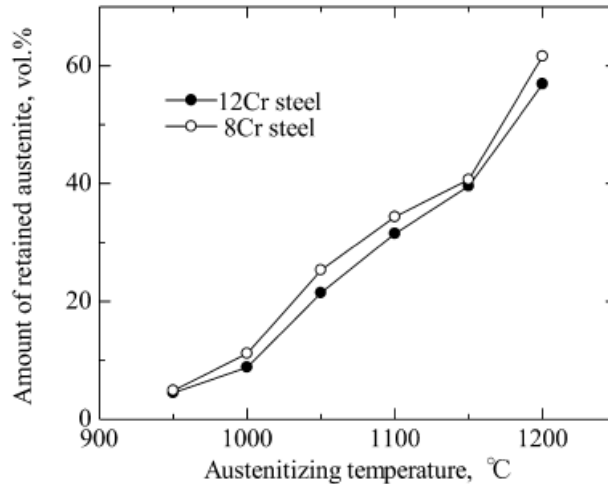


Figure 2.11- Amount of retained austenite present after quenching as a function of austenitizing temperature in Fe-Cr-C steels.

Figures 2.12 (a), (b), and (c) [13] is a TEM bright field, diffraction pattern and dark field image taken of a 12%Cr, 1.4%C Fe-Cr-C alloy, respectively. This demonstrates that there is retained austenite present in the material due to the high carbon content of the alloy. Little to no retained austenite is to be expected in lower carbon content steels, such as 0.12%C.

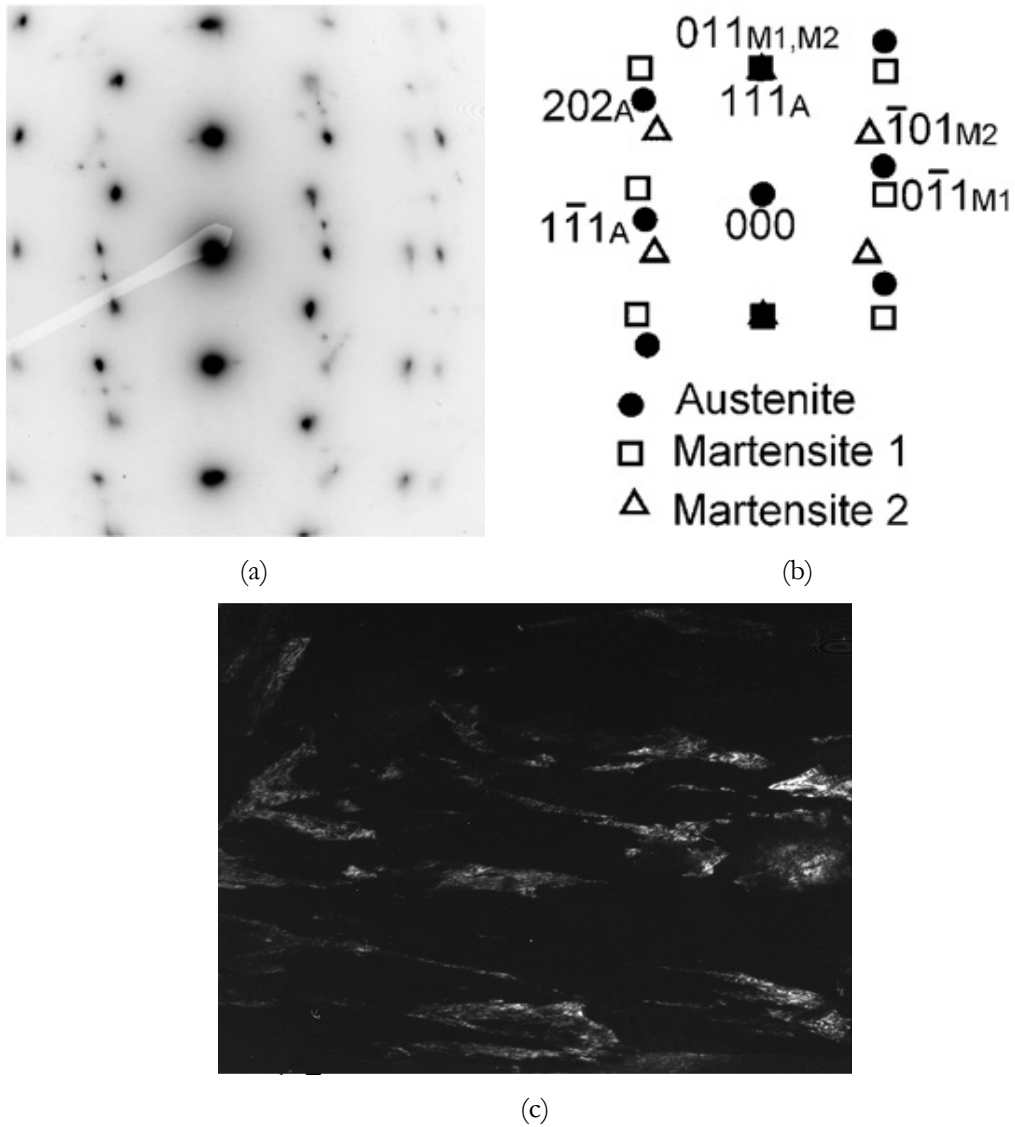


Figure 2.12- TEM microscopy (Bright and Dark Field) and diffraction patterns of a Fe-Cr-C steel [13]

Table 2.2 [13] shows results of Thermo-Calc calculations of how wt.%C in solid solution and martensite morphology varies with austenitizing temperature. It should be noted that there is a change in martensite morphology when the amount of carbon in solid solution is between 0.64 and 0.75wt.%C. This change in morphology could result in a change of mechanical properties at higher carbon

contents. Assuming no other change takes place at lower carbon contents, the morphology that will be dealt with in this work is lath martensite.

Table 2.2- Martensite morphology expected based on carbon content, as calculated by Thermo-Calc

Morphology of martensite and solution-carbon contents [mass%] in matrix calculated with Thermo-Calc

Austenitizing temperature [°C]	950	1000	1050	1100	1150
Sol.-C contents [mass%]					
12Cr steel	0.43	0.53	0.64	0.75	0.88
8Cr steel	0.45	0.55	0.65	0.79	0.92
Morphology	Lath	Lath	Lath	Lenticular	Lenticular

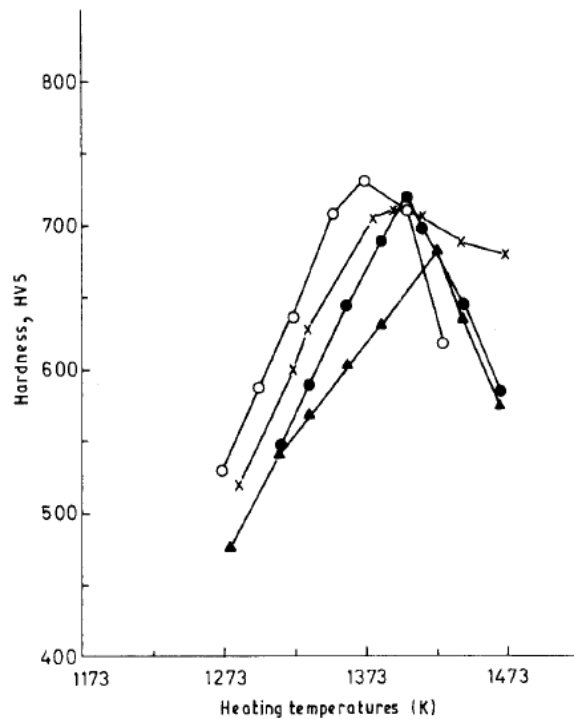
Other work done by de Alvarez et. al [14 and 15] at the CENIM laboratory in Spain looked into how quenching , carbide growth and microstructure morphology affected the amount of retained austenite, hardness, and other physical properties martensitic stainless steels very similar to the ones used in this work. The microhardness of martensitic stainless steels is very important in many applications. This measurement also allows an estimate of the tensile strength and ductility. It is therefore, very important to know how heating temperatures, quenching rates, etc. affect the microhardness of the material. De Alvarez et al. performed a study on how heating temperature affects the microhardness of quenched stainless steels, whose compositions are given in Table 2.3 [14].

Table 2.3 shows the compositions of the steels used in the studies

Chemical composition (mass %)

Steel	C	Si	Mn	P	S	Cr	Ni	Mo	V
X60CrMoV14	0.61	0.30	0.47	0.016	0.015	14.1	0.17	0.52	0.19
X45CrMoV14	0.46	0.46	0.44	0.018	0.003	14.3	0.16	0.51	0.13
X45Cr13	0.45	0.32	0.44	0.030	0.016	13.0	0.38		
X30Cr13	0.27	0.26	0.40	0.015	0.007	13.4	0.10		

Figure 2.13 is a diagram of Vickers hardness versus heating temperature. This diagram shows that there is a clear temperature, depending on the carbon content, that maximizes the hardness of the material and therefore the strength. The strength and ductility can be changed by changing the austenitizing temperature. There is a maximum hardness at a certain austenitizing temperature because if the temperature is too low there will be a higher amount of carbide formation, which pulls carbon out of solid solution and softens the martensite that forms. If the temperature is too high the austenite grains that form during the heat treatment will grow too large and this results in a decrease in hardness.



Influence of heating temperature on quenching hardness.
 (○) X60CrMoV14, (●) X45CrMo14, (x) X45Cr13, (▲) X30Cr13.

Figure 2.13 shows that the hardness of a quenched martensitic steel is dependent on the austenitizing temperature, with a clear maximum at a certain temperature that is dependent on carbon content [14]

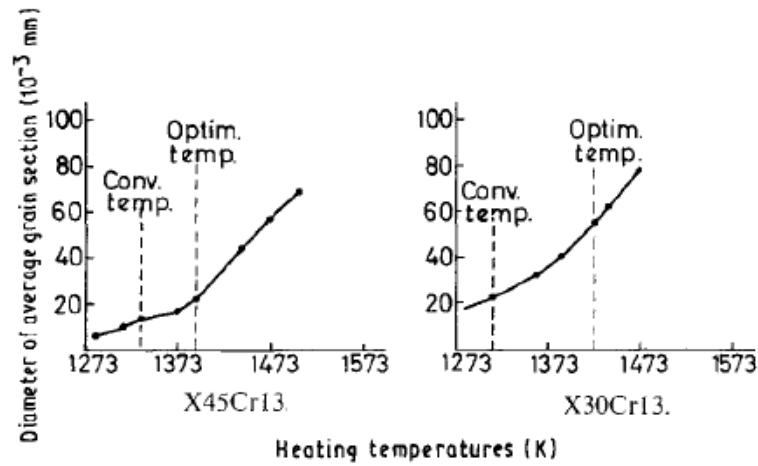


Figure 2.14- Plots of the average grain size of austenite that results as a function of heating temperature [14]

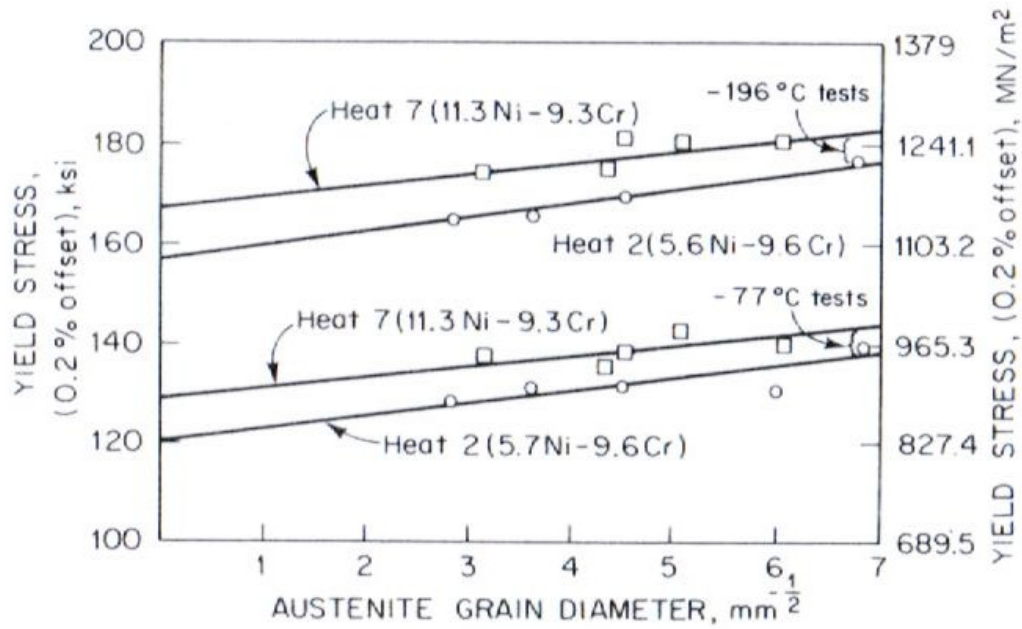


Figure 2.15- plot of yield strength as a function austenite grain diameter at various testing temperatures [16]

Figure 2.14 shows how heating temperature affects austenitic grain growth while Figure 2.15 plots the yield stress of martensitic steels as a function of grain

diameter. These two plots can be used together to predict and choose heat treating conditions that maximize the yield stress of the martensitic steels being studied. Figure 2.14 shows that the relationship between the yield stress and the square root of the diameter of the austenite grains is linear at low and room temperatures.

Figure 2.16 below relates how heating temperature impacts carbide growth. In order to make a martensitic steel more ductile, the amount of carbides in the microstructure should be kept as low as possible. This means heating to a higher temperature to dissolve carbides. But Figure 2.14 also shows heating to a very high temperature will cause the austenite grain size to be too large in size, which is also detrimental to mechanical properties. Therefore, a compromise between limiting carbide precipitation and austenite grain growth must be found.

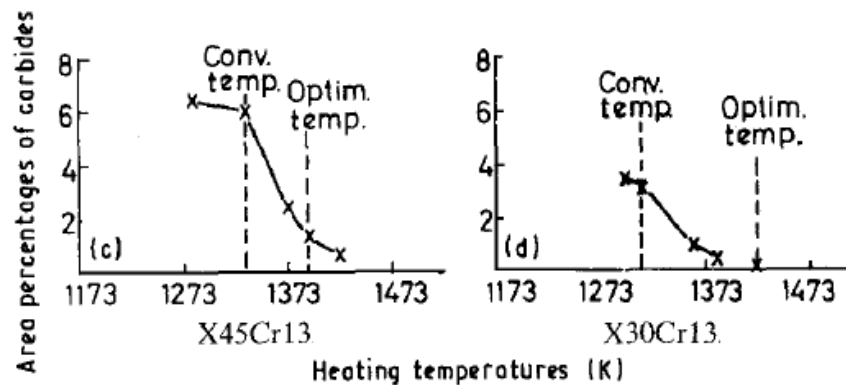


Figure 2.16- relates the percentage of carbides formed as a function of heating temperature. At a carbon content of 0.45%C the optimum temperature is 1393 K and at a carbon content of 0.3%C the optimum temperature to austenitize at, in terms of carbide formation is 1423K [14]

2.3 Decarburization in the Fe-C System

2.3.1 Overview

Isothermal decarburization is one avenue that is currently being explored by engineers to create functionally graded materials. A steel that has high carbon content can be partially decarburized at the edges of the material which should increase the ductility of the alloy, while retaining the high strength of the core.

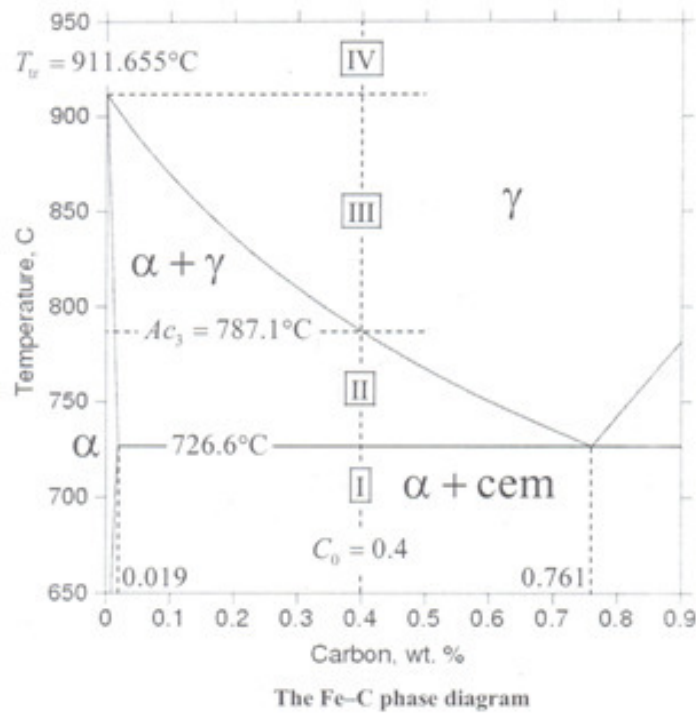


Figure 2.17- Phase diagram labeling the four different cases of decarburization in Fe-C alloys

Figure 2.17 [19] is the basic metastable iron-carbon phase diagram in a relatively low temperature range. From observation of the diagram, 4 different situations can be seen when decarburizing this system. The first situation occurs at a

low temperature when the material contains ferrite (α) and Cementite (Fe_3C). Isothermally decarburizing in this region, which exists at temperatures 727°C and below, causes the alpha and cementite to transform to pure alpha around a carbon content of 0.019%C. Above 727°C (region 2), at relatively lower carbon contents (i.e. 0 to 0.761), the cementite transforms to austenite (γ). Decarburization causes the alpha and gamma to decompose to pure alpha. Region three is the most complicated of the four regions. Two phase transformations occur in this region. The first is the transformation of austenite to a mixture of austenite and ferrite and then the transformation of the austenite and ferrite to pure ferrite. The other possibility is region 4, in which there is no transformation but just a composition gradient of carbon in the γ -phase.

The binary Fe-C alloy system can be considered in two ways. The first is in which the diffusion coefficients of carbon in the different phases are constant and the other is in which the diffusion coefficients are not constant. The former has analytical solutions while the latter has to be solved through numerical methods [21]. The former case will be studied and is based on a conference paper at the 5th ASM Heat Treatment and Surface Conference in Europe presented by Drs. Purdy and Malakhov [20].

2.3.2 Decarburization Methods

Imagine a piece of steel that has a homogeneous composition of carbon. Gases, either a mixture of CO and CO_2 or wet hydrogen, are passed along the

surface of the material, decarburizing it. The activity of carbon in wet hydrogen is the same as the activity of carbon in a vacuum. But a piece of steel will not decarburize in a vacuum, even though there is a large difference in chemical potential between the two atmospheres. The difference here is that the wet hydrogen acts as a catalyst for the removal of carbon from the material; no such catalyst exists in a vacuum. From thermodynamics, an activity of unity for carbon in steel means equilibrium with the pure carbon phase, or soot [6]. Therefore, the activity of carbon in steel is generally less than one.

When decarburization begins, ferrite starts to form at the surface due to the removal of carbon. An interface forms between the newly formed alpha and the original phase. Each case will now be examined. Modelling Decarburization [21] and a final report at McMaster [31] provide a nice descriptions and background on the equilibrium calculations of the different methods of decarburization of steels in different gases. References [22] and [23] also provide more information on the process of decarburization in ternary systems and the mathematics behind it but Malakhov and Purdy's treatment of the Fe-C system is more straightforward.

2.3.3 Case 1: $\alpha + \text{Fe}_3\text{C} \rightarrow \alpha$

In this situation, the carbon has been pulled out of solid solution to form the Iron carbide (cementite) phase.

Defining $z^*(t)$ the original position of the interface, after an infinitesimal

amount of time the position of the interface is now $z^*(t+dt)-z^*(t)$. This is also the thickness of the ferrite after time dt . At the time dt , the concentration $\mu_C^{steel} = \mu_C^{gas}$ [19]. The movement of this interface is due to the migration of carbon atoms from the $\alpha+Fe_3C$ to α -phase. The number of moles of carbon in the volume $[z^*(t+dt)-z^*(t)] \cdot A$ is equal to $(C^{\alpha|\alpha+cem} - C_0) \cdot dz^* \cdot A$. Because carbon atoms are migrating across an interface, this situation can be described in terms of a flux. Therefore:

$$-|J_C^\alpha| \cdot A \cdot dt = (C^{\alpha|\alpha+cem} - C_0) \cdot dz^* \cdot A$$

$$|J_C^\alpha| \cdot dt = (C_0 - C^{\alpha|\alpha+cem}) \cdot dz^*$$

Using Fick's first law, $J_C^\alpha = -D^\alpha \frac{\partial C^\alpha}{\partial z}$. The flux in this situation is the flux of carbon atoms from the boundary to the ferrite. Substituting Fick's Law into the above equation yields:

$$D^\alpha \frac{\partial C^\alpha}{\partial z} \cdot dt = (C_0 - C^{\alpha|\alpha+cem}) \cdot dz^* \rightarrow \frac{dz^*}{dt} = \frac{D^\alpha}{(C_0 - C^{\alpha|\alpha+cem})} \frac{\partial C^\alpha}{\partial z}$$

$\frac{dz^*}{dt}$ is the interface velocity, C_0 is the original composition and $C^{\alpha|\alpha+cem}$ is the composition at the interface.

During decarburization the carbon concentration at the surface of the steel is fixed and the carbon concentration at the interface of $\alpha/\alpha+cem$ is always the same since the decarburization is isothermal and the transformation always occurs at the

same composition. Using this knowledge, boundary conditions can be formulated that will allow a solution to this problem. These conditions can be represented mathematically as:

$$C^\alpha(z = 0) = C^{gas/\alpha} \quad \text{and} \quad C^\alpha(z^* = 0) = C^{\alpha|\alpha+cem}$$

To see how the concentration profile varies with position and time one can write Fick's second law:

$$\frac{\partial C^\alpha}{\partial t} = D^\alpha \frac{\partial^2 C^\alpha}{\partial z^2}$$

An equation is derived that satisfies Fick's second law using a plane initial source [2]:

$$C(z, t) = \frac{C^* \Delta x}{2\sqrt{\pi D t}} \exp\left(-\frac{(z - x_i)^2}{4 D t}\right)$$

If the slab that is being considered has an initial concentration of 0 and the surface concentration is fixed at C_0 then equation can be written as a sum using the principle of superposition [24] or the thin film problem [25]:

$$C(z, t) = \sum_0^\infty \frac{C_0 \Delta x}{2\sqrt{\pi D t}} \exp\left(-\frac{(z - x_i)^2}{4 D t}\right)$$

Hoyt states the solution by the thin film method is not “rigorously proven here that this summation of thin film behaviour constitutes a solution to the problem at hand, but qualitatively the procedure makes sense.” (Hoyt, 2010 pg. 20)

The summation can be replaced with an integral if Δx is infinitesimal:

$$\frac{C_0}{2\sqrt{\pi Dt}} \int_0^\infty \exp\left(-\frac{(z-x)^2}{4Dt}\right) dx \rightarrow \text{Make the substitution } \eta = \frac{z-x}{2\sqrt{Dt}} \text{ and}$$

$$\frac{d\eta}{dx} = -\frac{1}{2\sqrt{Dt}}$$

And the new limits of the integral become:

$$\eta_1 = \frac{z-\infty}{2\sqrt{Dt}} = -\infty \quad \text{and} \quad \eta_2 = \frac{z-0}{2\sqrt{Dt}} = \frac{z}{2\sqrt{Dt}}$$

Substituting η, dx, η_1 and η_2 into the above integral equation yields:

$$\frac{C_0}{2\sqrt{\pi Dt}} \int_{-\infty}^{\frac{z}{2\sqrt{Dt}}} \exp\left(-\frac{(z-x)^2}{4Dt}\right) (-2\sqrt{Dt}) d\eta = \frac{C_0}{\sqrt{\pi}} \int_{\frac{z}{2\sqrt{Dt}}}^{-\infty} \exp\left(-\frac{(z-x)^2}{4Dt}\right) d\eta$$

Using the error function definition and splitting the integral into two integrals by changing limits up from $-\infty$ to zero and zero to $\frac{z}{2\sqrt{Dt}}$ gives:

$$\frac{C_0}{\sqrt{\pi}} \left[\frac{\sqrt{\pi}}{2} + \frac{\sqrt{\pi}}{2} \operatorname{erf}\left(\frac{z}{2\sqrt{Dt}}\right) \right] = \frac{C_0}{2} + \frac{C_0}{2} \operatorname{erf}\left(\frac{z}{2\sqrt{Dt}}\right)$$

If diffusion from a fixed surface concentration with an initial concentration of C_0 , is considered then the above equation can be changed to:

$$C(z, t) = C_0 + (C_s - C_0) \operatorname{erf}\left(\frac{z}{2\sqrt{Dt}}\right)$$

Since C_o and C_s are constants, one can rewrite the solution as below and substitute any boundary conditions that are desired:

$$C(z, t) = C_1 + C_2 \operatorname{erf}\left(\frac{z}{2\sqrt{D\alpha t}}\right),$$

Where C_1 and C_2 are constants of integration. Applying the first boundary condition, $C^\alpha(z = 0) = C^{gas/\alpha}$, causes the error function to equal zero, leaving $C_1 = C^{gas/\alpha}$. If wet hydrogen is used as the decarburizing atmosphere, the carbon concentration at the surface is equal to zero. Any surface concentration can be chosen by using a mixture of CO and CO₂ but the transformation from $\alpha+cem$ to α would not occur since a carbon content of essentially zero is required for the transformation to ferrite. Applying the second boundary condition, $C^\alpha(z^* = 0) = C^{\alpha|\alpha+cem}$, yields:

$$C^{\alpha|\alpha+cem} = C_2 \operatorname{erf}\left(\frac{z^*}{2\sqrt{D\alpha t}}\right) \rightarrow C_2 = \frac{C^{\alpha|\alpha+cem}}{\operatorname{erf}\left(\frac{z^*}{2\sqrt{D\alpha t}}\right)}$$

Substitution of C_1 and C_2 provides:

$$C^\alpha(z, t) = C^{\alpha|\alpha+cem} \cdot \frac{\operatorname{erf}\left(\frac{z}{2\sqrt{D\alpha t}}\right)}{\operatorname{erf}\left(\frac{z^*}{2\sqrt{D\alpha t}}\right)}$$

To see how the composition changes with position, the derivative of the above expression can be taken with respect to z .

$$\frac{\partial C^\alpha}{\partial z} = \frac{\partial}{\partial z} \left(C^{\alpha|a+cem} \cdot \frac{\operatorname{erf}\left(\frac{z}{2\sqrt{D^\alpha t}}\right)}{\operatorname{erf}\left(\frac{z^*}{2\sqrt{D^\alpha t}}\right)} \right)$$

The error function definition can be used to differentiate the expression. The error function in the denominator of the above equation is constant since z^* the position of the interface at a given time.

$$\operatorname{erf}(z) = \frac{2}{\sqrt{\pi}} \int_0^z e^{-\eta^2} d\eta \quad \rightarrow \quad \frac{d}{dz} \operatorname{erf}(z) = \frac{2}{\sqrt{\pi}} (e^{-z^2})$$

Using the fact that the substitution method was used to integrate the exponential function in the course of solving of Fick's second law, it can be determined what the original function was in the exponent by squaring the term in the error function. This is due to the fact that the substitution made requires one to take the square root of the original function in the exponential. This makes sense because mathematically integration reverses differentiation and vice versa. Differentiating the error function yields:

$$\frac{d}{dz} \left(\operatorname{erf}\left(\frac{z}{2\sqrt{D^\alpha t}}\right) \right) = \frac{2}{\sqrt{\pi}} \left(\frac{1}{2\sqrt{D^\alpha t}} \right) \exp\left(-\frac{z^2}{4D^\alpha t}\right) = \left(\frac{1}{\sqrt{\pi D^\alpha t}} \right) \exp\left(-\frac{z^2}{4D^\alpha t}\right)$$

Therefore the concentration derivative becomes:

$$\frac{\partial C^\alpha}{\partial z} = \frac{C^{\alpha|a+cem}}{\sqrt{\pi D^\alpha t}} \cdot \frac{\exp\left(-\frac{z^2}{4D^\alpha t}\right)}{\operatorname{erf}\left(\frac{z^*}{2\sqrt{D^\alpha t}}\right)}$$

Substitution of the interface position, z^* , into the above equation provides the concentration gradient of carbon across the interface of $\alpha/\alpha+\text{cem}$. This completes case one for an isothermal decarburization in the $\alpha+\text{cem}$ phase.

2.3.4 Case 2: $\alpha+\gamma\rightarrow\alpha$

In this case Purdy and Malakhov make a substitution of cementite for austenite to derive the equations for composition profile and composition gradient. This results in the following equations:

$$C^\alpha(z, t) = C^{\alpha|\alpha+\gamma} \cdot \frac{\text{erf}\left(\frac{z}{2\sqrt{D^\alpha t}}\right)}{\text{erf}\left(\frac{z^*}{2\sqrt{D^\alpha t}}\right)}$$

and

$$\frac{\partial C^\alpha}{\partial z} = \frac{C^{\alpha|\alpha+\gamma}}{\sqrt{\pi D^\alpha t}} \cdot \frac{\exp\left(-\frac{z^2}{4D^\alpha t}\right)}{\text{erf}\left(\frac{z^*}{2\sqrt{D^\alpha t}}\right)}$$

This substitution can be made because the activity of the carbon is constant in a two phase region at a given composition. For example in the $\alpha+\gamma$ phase, $a_c^\alpha = a_c^\gamma$. However, any literature on whether the activity of carbon is constant regardless of whether the system is in the $\alpha+\text{cem}$ or $\alpha+\gamma$ phases could not be found. Since the authors just switched the superscripts in their paper one would assume this to be the case.

2.3.5 Case 3: $\gamma \rightarrow \alpha + \gamma \rightarrow \alpha$

The analysis of this region will begin in the same way that the other regions were, by a derivation of the interface velocity during decarburization. In this situation there will be two fluxes present. The first is the flux of carbon from the γ to interface and the flux of carbon from the interface into the ferrite. In order to write the material balance, the movement of the interface at the $\alpha/\alpha + \gamma$ boundary will be considered. This is almost analogous to case one except for the fact that there are two fluxes present.

Material balance:

$$(C^{\alpha|\alpha+\gamma} - C^{\alpha+\gamma|\gamma}) \cdot A \cdot dz^* = (J^\alpha - J^\gamma) \cdot A \cdot dt$$

$C^{\alpha|\alpha+\gamma} - C^{\alpha+\gamma|\gamma}$ is always a negative value since the composition of carbon at the $\alpha/\alpha + \gamma$ interface is less than the value at the $\alpha + \gamma/\gamma$ interface. Therefore, the C's or the J's can be flipped to get rid of the negative. In this case the C's will be flipped.

The equation becomes:

$$(C^{\alpha+\gamma|\gamma} - C^{\alpha|\alpha+\gamma}) dz^* = (J^\alpha - J^\gamma) dt \rightarrow \frac{dz^*}{dt} = \frac{J^\alpha - J^\gamma}{C^{\alpha+\gamma|\gamma} - C^{\alpha|\alpha+\gamma}}$$

Using Fick's first law again transforms the equation to:

$$\frac{dz^*}{dt} = \frac{1}{C^{\alpha+\gamma|\gamma} - C^{\alpha|\alpha+\gamma}} \left(D^\alpha \frac{dC^\alpha}{dz} - D^\gamma \frac{dC^\gamma}{dz} \right)$$

If the composition gradient in ferrite is greater than the composition gradient in austenite, then the ferrite interface will grow into the material. This should always be expected in this case because ferrite is a body centered cubic material while austenite is face centred cubic material. This means that the diffusion of carbon through ferrite is much higher than in the austenite because the ferrite is much less closely packed than the austenite which leaves more room for carbon to move to interstitial sites in the lattice. However, if the flux of carbon away from the interface into the ferrite is less than the flux of carbon from the austenite to the interface, then the interface velocity would be negative and retreat back towards the surface of the material. The effect of carbon content on decarburization kinetics is discussed in detail by Marder et al. [26].

Now equations that describe the composition of carbon as a function of position and time in both the austenite and the ferrite can be derived. The boundary conditions are more complicated in this case than in the previous cases. The boundary conditions for the austenite concentration can be formulated as follows: The concentration of carbon at the $\alpha+\gamma/\gamma$ interface will always be the concentration at which that transformation takes place, $C^{\alpha+\gamma|\gamma}$. The second boundary condition can be determined through determination of the composition of the austenite far away from the interface, i.e. the core of the steel. Far away from the interface the concentration of carbon is always the initial concentration of the sample, C_0 . These can be represented mathematically as $C^\gamma(z^*) = C^{\alpha+\gamma|\gamma}$ and $C^\gamma(z = \infty) = C_0$.

There is another complication that we must be mindful of in this case. This complication is the fact that diffusion in the ferrite begins as soon as the heat treatment begins while diffusion in the austenite starts when the material has reached the temperature at which the austenite forms. This is represented in Figure 2.18 as temperature A_{c_3} . At an initial carbon content of 0.4%C this temperature is 787°C. Purdy and Malakhov call this “the austenite clock”, denoted as t_0 and t is the time elapsed since the start of the heat treatment. Returning to the analytical solution for Fick’s second law:

$$C^\gamma(z, t) = C_1^\gamma + C_2^\gamma \operatorname{erf}\left(\frac{z}{2\sqrt{D^\gamma(t-t_0)}}\right)$$

Using boundary conditions one and two, C_1^γ and C_2^γ can be determined:

$$\text{B.C. 1:} \quad C^\gamma(z^*) = C^{\alpha+\gamma|\gamma} = C_1^\gamma + C_2^\gamma \operatorname{erf}\left(\frac{z^*}{2\sqrt{D^\gamma(t-t_0)}}\right)$$

$$\text{B.C. 2:} \quad C^\gamma(z = \infty) = C_0 = C_1^\gamma + C_2^\gamma \operatorname{erf}(\infty) = C_1^\gamma + C_2^\gamma$$

B.C. 2 can be solved for $C_1^\gamma = C_0 - C_2^\gamma$ and substituted into eq’n B.C. 1. This yields:

$$C^{\alpha+\gamma|\gamma} = C_0 - C_2^\gamma + C_2^\gamma \operatorname{erf}\left(\frac{z^*}{2\sqrt{D^\gamma(t-t_0)}}\right) \rightarrow C_2^\gamma = \frac{C^{\alpha+\gamma|\gamma} - C_0}{\operatorname{erf}\left(\frac{z^*}{2\sqrt{D^\gamma(t-t_0)}}\right) - 1}$$

This can be simplified further by using the definition of the complementary error function ($\operatorname{erfc}(z) = 1 - \operatorname{erf}(z)$). C_2^γ finally equals $\frac{C_0 - C^{\alpha+\gamma|\gamma}}{\operatorname{erfc}\left(\frac{z^*}{2\sqrt{D^\gamma(t-t_0)}}\right)}$ and

$$\begin{aligned}
C_1^\gamma &= C_0 - \frac{C_0 - C^{\alpha+\gamma|\gamma}}{\operatorname{erfc}\left(\frac{z^*}{2\sqrt{D^\gamma(t-t_0)}}\right)} \\
&= \frac{C_0\left(\operatorname{erfc}\left(\frac{z^*}{2\sqrt{D^\gamma(t-t_0)}}\right) - 1\right) + C^{\alpha+\gamma|\gamma}}{\operatorname{erfc}\left(\frac{z^*}{2\sqrt{D^\gamma(t-t_0)}}\right)} \\
&= \frac{C_0\operatorname{erf}\left(\frac{z^*}{2\sqrt{D^\gamma(t-t_0)}}\right) + C^{\alpha+\gamma|\gamma}}{\operatorname{erfc}\left(\frac{z^*}{2\sqrt{D^\gamma(t-t_0)}}\right)}
\end{aligned}$$

The final equation for the carbon concentration as a function of position and time is:

$$\begin{aligned}
C^\gamma(z, t) &= \frac{C^{\alpha+\gamma|\gamma} - C_0\operatorname{erf}\left(\frac{z^*}{2\sqrt{D^\gamma(t-t_0)}}\right)}{\operatorname{erfc}\left(\frac{z^*}{2\sqrt{D^\gamma(t-t_0)}}\right)} \\
&\quad + \frac{C_0 - C^{\alpha+\gamma|\gamma}}{\operatorname{erfc}\left(\frac{z^*}{2\sqrt{D^\gamma(t-t_0)}}\right)} \operatorname{erf}\left(\frac{z}{2\sqrt{D^\gamma(t-t_0)}}\right)
\end{aligned}$$

As done for the previous cases, the composition equation for γ can be differentiated with respect to z :

$$\frac{\partial C^\gamma}{\partial z} = \frac{C_0 - C^{\alpha+\gamma|\gamma}}{\sqrt{\pi D^\gamma(t-t_0)} \cdot \operatorname{erfc}\left(\frac{z^*}{2\sqrt{D^\gamma(t-t_0)}}\right)} \exp\left(-\frac{z^2}{4D^\gamma(t-t_0)}\right)$$

Purdy and Malakhov retain the diffusion coefficient of carbon in ferrite in the above equation. This is correct as the above equations determine the concentration profile of carbon in austenite.

The composition profile in the ferrite is exactly the same as case 2:

$$C^\alpha(z, t) = C^{\alpha|\alpha+cem} \cdot \frac{\operatorname{erf}\left(\frac{z}{2\sqrt{D^\alpha t}}\right)}{\operatorname{erf}\left(\frac{z^*}{2\sqrt{D^\alpha t}}\right)}$$

$$\frac{\partial C^\alpha}{\partial z} = \frac{C^{\alpha|\alpha+cem}}{\sqrt{\pi D^\alpha t}} \cdot \frac{\exp\left(-\frac{z^2}{4D^\alpha t}\right)}{\operatorname{erf}\left(\frac{z^*}{2\sqrt{D^\alpha t}}\right)}$$

$\frac{\partial C^\gamma}{\partial z}$ and $\frac{\partial C^\alpha}{\partial z}$ can be substituted into $\frac{dz^*}{dt}$. This substitution gives us the equation for

the interface velocity for this case:

$$\frac{dz^*}{dt} = \frac{1}{C^{\alpha+\gamma|\gamma} - C^{\alpha|\alpha+\gamma}} \left(D^\alpha \frac{C^{\alpha|\alpha+\gamma}}{\sqrt{\pi D^\alpha t}} \cdot \frac{\exp\left(-\frac{z^2}{4D^\alpha t}\right)}{\operatorname{erf}\left(\frac{z^*}{2\sqrt{D^\alpha t}}\right)} - D^\gamma \frac{C_0 - C^{\alpha+\gamma|\gamma}}{\sqrt{\pi D^\gamma (t - t_0)}} \cdot \operatorname{erfc}\left(\frac{z^*}{2\sqrt{D^\gamma (t - t_0)}}\right) \exp\left(-\frac{z^2}{4D^\gamma (t - t_0)}\right) \right)$$

2.3.6 Case 4: Decarburization of Austenite

Since there is no transformation in this case it is the most straightforward one to solve. Different “clocks” would not need to be retained in this case because the entire material is austenitic and the carbon would start diffusing at the same time throughout the material; Purdy and Malakhov retain the idea of the clocks in this case, although it is not intuitive to do so. Also, there is no interface in this case because there is no phase transformation that occurs. The problem thus becomes a straightforward diffusion problem and does not require a material balance.

One can start with the solution to Fick’s second law and apply the boundary conditions. The boundary conditions in case 4 are incredibly simple. At the surface of the material the carbon concentration is zero and in the bulk of the material it is C_0 for all times. These are represented mathematically as:

$$C^\gamma(z = 0) = C^{gas/\alpha} = 0 \quad \text{and} \quad C^\gamma(z = \infty) = C_0$$

Applying these to the same solution used in the previous cases yields:

$$C^\gamma(z, t) = C_0 \operatorname{erf}\left(\frac{z}{2\sqrt{D^\gamma t}}\right)$$

And differentiating $C^\gamma(z, t)$ results in:

$$\frac{\partial C^\gamma}{\partial z} = \frac{C_0}{\sqrt{\pi D^\gamma t}} \exp\left(-\frac{z^2}{4D^\gamma t}\right)$$

This short amount of work concludes case 4.

2.3.7 Diffusion Profiles

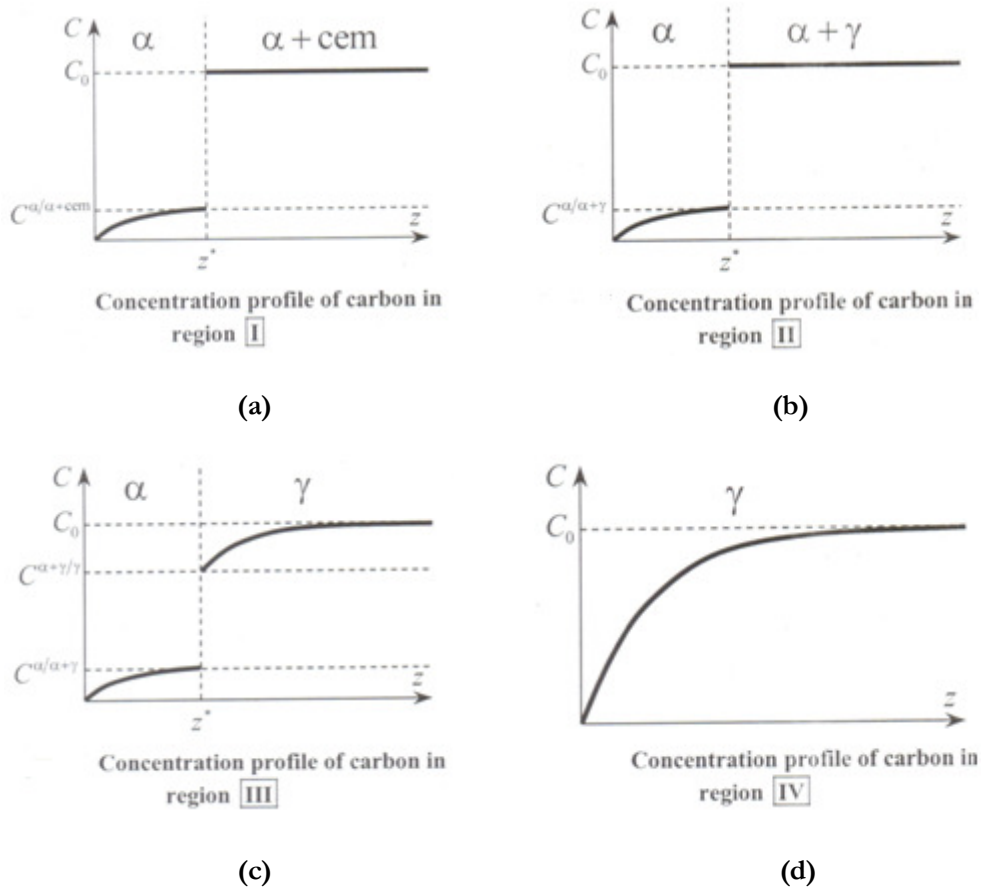


Figure 2.18- Carbon profiles of the four decarburization cases in an Fe-C alloy [19]

The above figures [19] show what the concentration profiles of carbon look like in all of the different cases. The profiles for cases three and four are very intuitive. A smooth decrease in carbon content on the right side of the interface, towards the interface indicates that diffusion is occurring. However in cases one and two, there is no diffusion on the right side of the interface. Malakohv [19] states that

the chemical potential of carbon in an alloy in the two phase region is constant, independent of composition and that is why diffusion does not occur on the right hand side of the interface in cases one and two.

2.3.8 Decarburization

Local Equilibrium, With Partitioning (LEP)

In the local equilibrium model, it is assumed that the interface is moving slowly enough that at the interface the material is in a state of equilibrium. When partitioning is assumed, the interface is said to move slow enough that all of the alloying elements can partition. According to Hasiguchi [42] LEP is a “limiting state defined by a uniform carbon chemical potential and a continuous substitutional element to iron mole fraction ratio at the transforming interface”. Figure 2.19 [31] is a diagram that explains this model. The diagram describes the situation when ferrite is transforming to austenite. This model does not work when carbon saturation is high and works well if diffusion times are long [31].

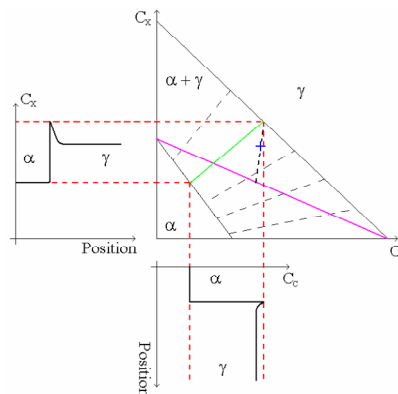


Figure 2.19- Local equilibrium with partitioning assumption in Fe-M-C system

Local Equilibrium No Partitioning (LENP)

This model works well for large supersaturations and assumes that only carbon can partition [43]. Because partitioning does not occur, the energy that is released when the austenite transforms to ferrite does not bring the total energy of the system to minimum but it is assumed that amount of energy released is large enough to cause the transformation to occur. Hasiguchi [42] describes LENP as “a kinetic state defined by a no-partition local equilibrium for all components at the interface which requires a corresponding steep diffusion profile spike of alloying elements ahead of the interface.” Figure 2.20 [31] below describes this model.

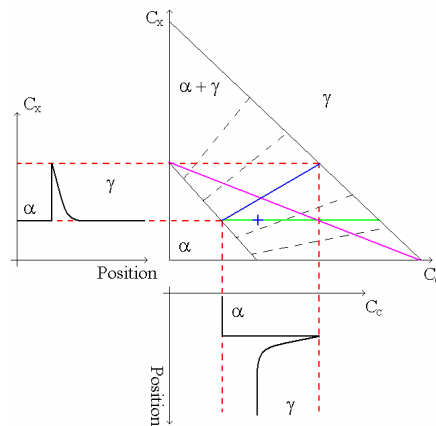


Figure 2.20- Local equilibrium, no partitioning assumption in Fe-M-C system

Para-Equilibrium(PE)

PE is used when the interface velocity is very fast. In this model the alloying elements cannot diffuse in the austenite because of this higher interface velocity. The situation is described by Figure 5 [5] on the next page.

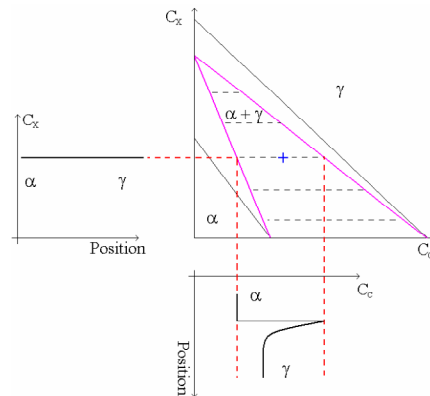


Figure 2.21- Para-equilibrium assumption in Fe-M-C system

Chapter 3

Experimental Procedure

This section describes the various experimental procedures and techniques used for the results in this work.

3.1 Experimental

Decarburization is a kinetically driven process. It can occur at moderate temperatures (700-900°C) but happens rapidly and readily at higher temperatures. However, as seen from the literature review, at temperatures above the optimum heat treating temperature there are high austenite grain growth kinetics and a decrease in hardness and strength. Microstructural characterization and mechanical testing was carried out to determine how decarburization affects the properties of martensitic stainless steel.

3.1.1 Material

The type of material used in this work was martensitic stainless steel. Three different alloys were compared. The compositions of the different steels used are shown in the table below. All samples were heated to sufficiently high temperature to ensure a fully austenitic structure that would transform to martensite upon quenching. The composition of the materials was determined through Glow Discharge Optical Emission Spectroscopy (GDOES). Bulk carbon content of the material was also determined through Carbon and Sulfur analysis. Table 3.1 shows typical values of the alloying components in the MA grades produced by Arcelor Mittal. These values were checked using Carbon and Sulfur analysis and the values obtained were found to be 0.13%C for the MA1, 0.33%C for the MA3 and 0.44%C in the MA4 grade.

Table 3.1- Typical values of alloying compositions in the MA grades provided from Arcelor Mittal [27]

Grade	Chemical compositions (typical values in wt.%)			
	C	Si	Mn	Cr
MA1	0.11	0.35	0.30	12.30
MA2	0.21	0.35	0.35	13.30
MA3	0.33	0.20	0.30	13.70
MA4	0.46	0.35	0.30	13.80

The material was received in the annealed and cold rolled condition, with an initial microstructure of ferrite and carbide. The as-received material was then heated to the austenitic region for 10 minutes in Ultra High Purity (UHP) Argon. The temperature of the austenitizing and decarburizing was dependent on the carbon

content of the original alloy. The MA1 alloy was austenitized or decarburized at 1000°C, the MA3 was austenitized or decarburized at 1100°C and the MA4 was austenitized or decarburized at 1120°C.

3.1.2 Materials Processing

Austenitization treatments were carried out in UHP Ar at the temperatures stated above for 10 minutes. UHP Ar was used to help minimize the amount of decarburization the material would experience at high temperatures. A heating time of 10 minutes was chosen to prevent austenite grain growth but also dissolve carbides.

The vast majority of the decarburizations that were carried out in an atmosphere of wet hydrogen, with a flow rate of 100 cc/min. The times were varied to achieve different decarburization profiles. The used most often were 10, 15, 20, 30, 60 and 120 minutes. An atmosphere of CO and CO₂ was also used in the higher carbon content alloys (MA3 and MA4). The atmosphere was adjusted to achieve surface carbon contents of 0.1%C and 0.15%C. CO and CO₂ were only used on MA3 and MA4 because 0.1%C and 0.15%C would not decarburize the MA1 grade. The ratio of CO to CO₂ required was calculated using Thermo Calc®.

The furnace that was used that had samples that were carburized/decarburized in an atmosphere of CO and CO₂ had to be specially modified because soot formation was observed when the CO and CO₂ were mixed at room temperature.

This was due to the fact that at lower temperatures than the one the heat carburizing/decarburizing was carried out at, the gas mixture had an activity higher than unity. Therefore, a smaller tube was inserted into the larger furnace tube. The larger tube carried CO₂ and the smaller tube carried CO. A temperature of 900°C was found in the furnace. It was at this point the gases were mixed so that soot formation would occur. Soot does not form at room temperature because the kinetics of the formation is much too low. However, between 300°C and 600°C the kinetics of the soot formation are fast enough that soot formation does occur. By mixing the gases at 900°C, this soot formation was avoided.

Samples that were deformed have also been tempered. Tempering was performed in a temperature range of 200-600°C to determine the optimum tempering temperature. The optimum tempering temperature was determined to be 500°C. This is also confirmed in literature [17].

Quenching media used were quenching oil and pressurized air. This was done to determine how quenching rate affects the properties of martensitic steels.

3.1.3 Microstructure Characterization

3.1.3.1 Polishing

Microstructure characterization is very important in determining why a material has given properties and behaves the way it does. Being able to clearly

observe microstructure is critical in properly analyzing mechanical testing and also allows engineers to make inferences about how heat treatments and materials processing affects microstructure and final properties. The following steps were performed to get a very smooth surface suitable for etching:

1. Grinding: SiC #320 for 1.5 minutes, water as a lubricant
2. Grinding: SiC #800 for 1.5 minutes, water as a lubricant
3. Grinding: SiC #2400 for 1.5 minutes, water as a lubricant
4. Grinding : SiC #4000 for 1.5 minutes, water as a lubricant
5. Polishing: Plan cloth -15 μm for 7.5 minutes, Blue solution as a lubricant and 15 μm diamond suspension.
6. Polishing: DAC cloth - 3 μm for 5 minutes, Blue solution as a lubricant and 3 μm diamond suspension.
7. Polishing: NAP cloth - 1 μm for 5 minutes, Blue solution as a lubricant and 1 μm diamond suspension.
8. Polishing: Chem cloth - 0.05 μm for 20 minutes, Alumina suspension.

The grinding and polishing steps were carried out on a Struers grinding machine. Grinding should be carried out for a maximum of 1.5 minutes because grinding with rougher grit paper for too long causes scratches to form below the surface of the material. The surface scratches disappear when the polishing steps are performed but will reappear when the material is chemically etched. The extra grinding steps also help to reduce this effect. If the material is only grinded with #320 grit paper the scratches will appear after etching but the finer etching steps reduce or eliminate these scratches. Another important note is that step 8 should only be carried out if the samples are being observed under SEM. Otherwise step 7 is sufficient for optical microscopy.

3.1.3.2 Etching

Stainless steel is specifically designed to resist chemical attack and corrosion. This makes etching stainless steel difficult. However, some etchants do work and the ones that were used during this research are listed below, along with their compositions. All etchants and information on those were taken from ASTM E7-T55 or received from Arcelor-Mittal internal documents [reference?].

Vilella's Reagent

1. 1 gram of Picric Acid
2. 10 mL of Hydrochloric Acid (HCl)
3. 100 mL of Ethanol

The samples were immersed in the reagent until the material darkened. The reagent can be made in mass quantity but will only keep for 1 week. This reagent is good for revealing martensite, ferrite and carbide structures

Kalling's Reagent

1. 12.5 grams of CuCl_2
2. 100 mL of HCl
3. 100 mL of Ethanol

The samples were immersed in the reagent until the material darkened. This reagent can be reused and has a long shelf life. It is good for differentiating between ferrite and martensite, which is why it is used for etching duplex stainless steel. The mechanism of etching is not removing surface material but depositing a copper film on the surface of the material which reveals the microstructure.

Lichtenegger-Bloech (3rd Variant)

1. 1 gram of Ammonium diFluoride (NH_4HF_2)
2. 0.5 grams of Potassium Metabisulfite ($\text{K}_2\text{S}_2\text{O}_5$)
3. 100 mL of distilled water

This solution was heated to 30°C and the material was immersed in the solution until it darkened. This etchant reveals the structure and size of the grains present but not the phases present.

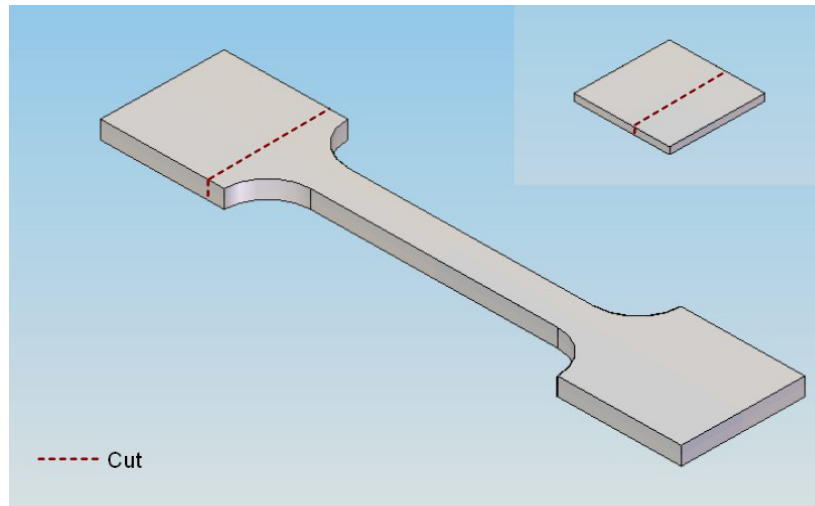
3.1.4 Tensile Testing

Tensile samples were cut using Electro-Discharge Machining to ensure a defect free surface in the gauge length. This would provide in consistent results, as well as provide accurate measurements of the materials properties without any surface defects amplifying stress during testing. Tensile testing was carried out on two different machines. The MA1 tensile samples were tested on the INSTRON 5566 Universal Testing Machine, whose load cell has a maximum capable load of 10 000 N. Because of the higher carbon contents of the MA3 and MA4, higher loads were expected so the MTS 810 Material Test System machine was used for these samples. The maximum allowable load on this machine is 100 000 N. The software used was Instron Wave Maker. All tensile tests were carried out at room temperature at a strain rate 1mm/minute. The strain was measured by a Strain Gauge extensometer, with a gauge length of 12.5 mm. The cross sectional area of the gauge length was carefully measured before each test and recorded. The area after fracture of the sample was measured using SEM and this area was used to calculate the fracture

stress and strain, as well as reduction of area. Equations 3.1 and 3.2 are for the fracture stress and fracture strain, respectively. A picture of a tensile sample is shown in the figure on the next page and the dimensions of the two different types of tensile samples are given in the table on the next page as well.

$$\sigma_f = \frac{P_f}{A_f} \quad \text{and} \quad \varepsilon_f = \ln\left(\frac{A_0}{A_f}\right) \quad (3.1)$$

Tensile tests were performed on austenitized and decarburized samples. They were also performed on deformed and tempered samples that were homogeneous and graded.



	Grip Width	Total Length	Gauge Length	Gauge Width	Curvature
Regular	12 mm	80 mm	15 mm	3 mm	R12
Deformed	12 mm	60 mm	10 mm	3 mm	R12

Figure 3.1- details the dimensions of 2 different tensile samples used and how it was cut for metallographic analysis [28]

3.1.5 Cold Rolling

Cold rolling experiments were carried out on austenitized and decarburized samples to determine whether decarburization improved the plane strain properties of the materials. Cold rolling also allowed a study of the microstructure and properties of materials at higher deformations than tensile tests allow. Cold rolling was also used to deform samples to be used in recovery/recrystallization experiments. These experiments involved sheets and tensile specimens. The von Mises equation was used to calculate the equivalent strain in the samples. This is given in the equation below [29]:

$$\varepsilon_{vM} = \left(\frac{2}{\sqrt{3}}\right) \ln\left(\frac{t_0}{t_f}\right) \quad (5.8)$$

Where ε_{vM} is the von Mises strain, t_0 is the original thickness and t_f is the final thickness.

Chapter 4

Results

This section describes the results from the various experiments, and mechanical testing that has been performed. It has been divided into the following sections:

1. Characterization of the homogeneous and graded steel
2. Tensile results
3. Rolling results
4. Charpy Impact testing

4.1 Characterization

4.1.1 0.13% Carbon (MA1)

Characterization of the samples was performed to determine properties of the homogeneous and graded materials. This was done in order to compare the properties between homogeneous and graded samples as well as to make inferences as to why the tensile, rolling, and impact properties behaved or changed the way they did in the graded samples.

Homogeneous MA1

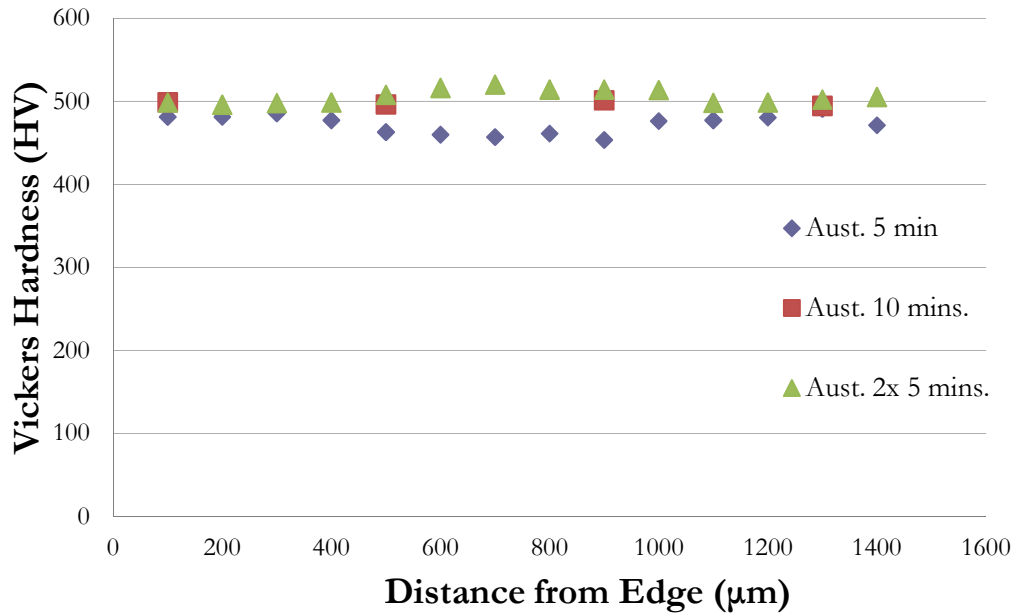


Figure 4.1- Vickers hardness vs. austenitization times for MA1 material

Figure 4.1 shows how the microhardness of the samples is affected by austenitization times. It can be seen that the time spent austenitizing the sample does

not affect the microhardness of the air quenched samples.

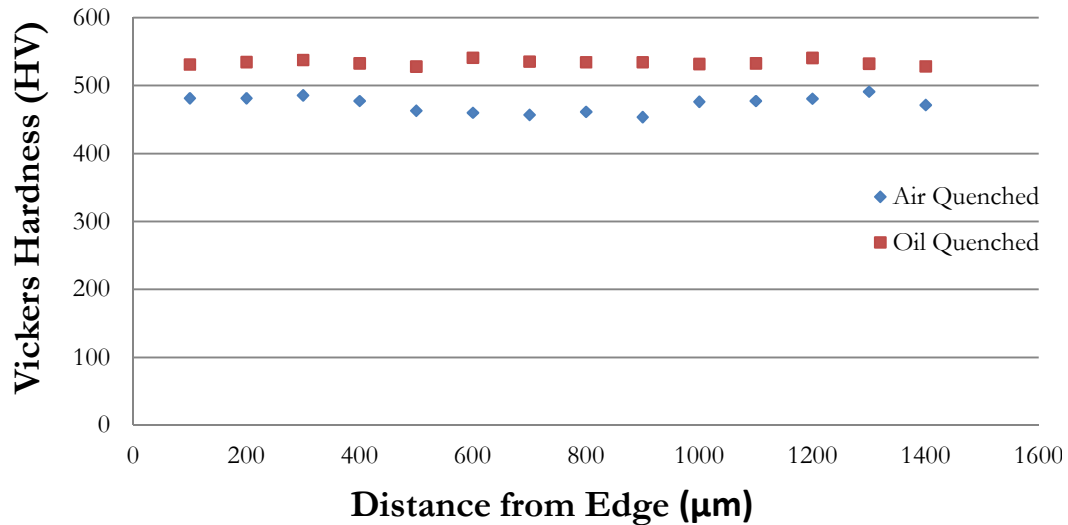


Figure 4.2- how quenching media affects the microhardness of the quenched material in MA1 alloy

Figure 4.2 shows how the hardness is affected by the quenching medium used. Two different quenchants were tried for austenitization times of 5 minutes. The first one that was tried was quenching oil. This was tried because in previous experiments performed by researchers at McMaster University, quenching oil provided smooth cooling curves. Pressurized air was also tried because pressurized air is what is used in industry to produce a more ductile as-quenched material. As can be seen in the microhardness profile, quenching in oil produced a material that was slightly harder.

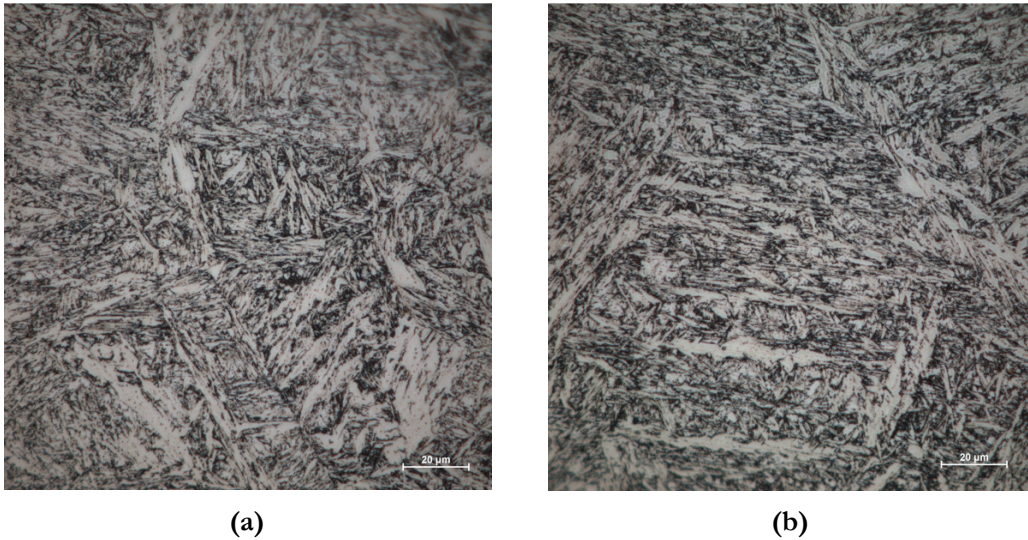
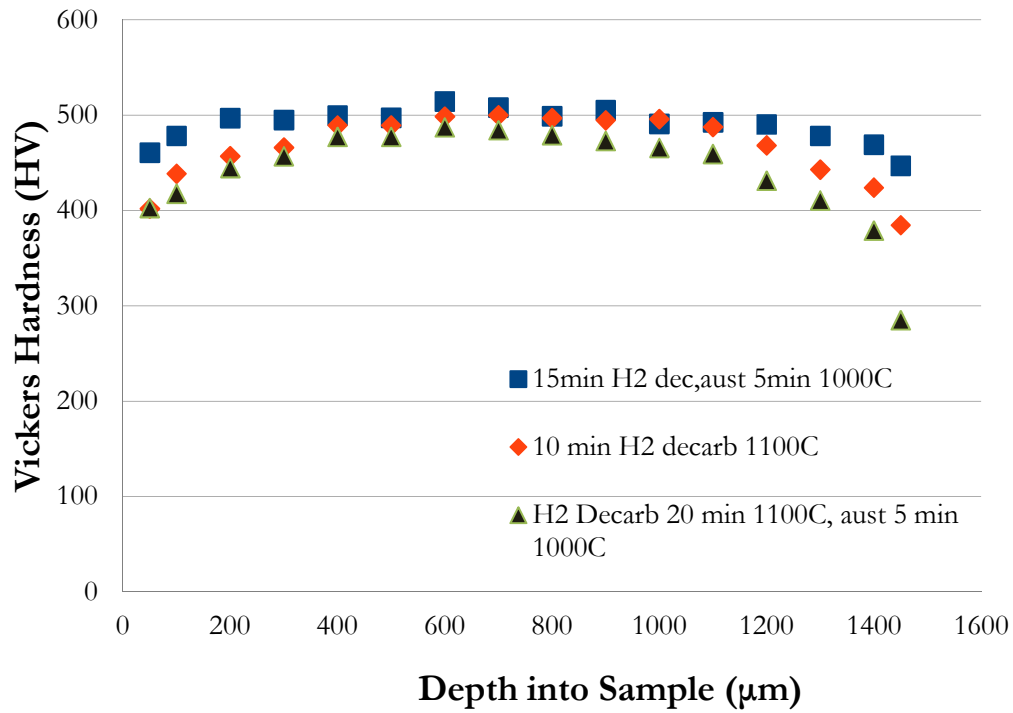


Figure 4.3- Micrographs of a sample austenitized for 5 minutes. (a) is the centre of the sample and (b) for the edge of the sample

The above micrographs show a MA1 sample that has been austenitized for 5 minutes. The microstructures are the same for the centre and the edge of the sample; it consists of lath martensite in both cases. These micrographs were etched using Kalling's Reagent

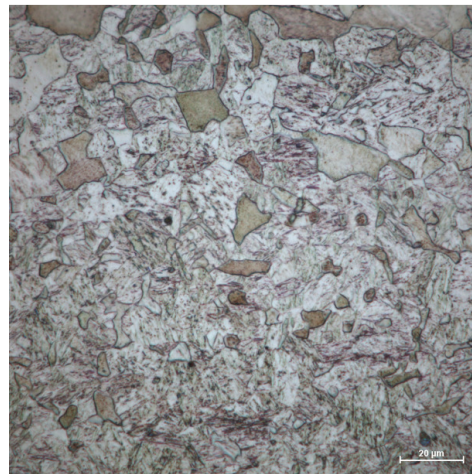
Graded MA1



(a)



(b)



(c)

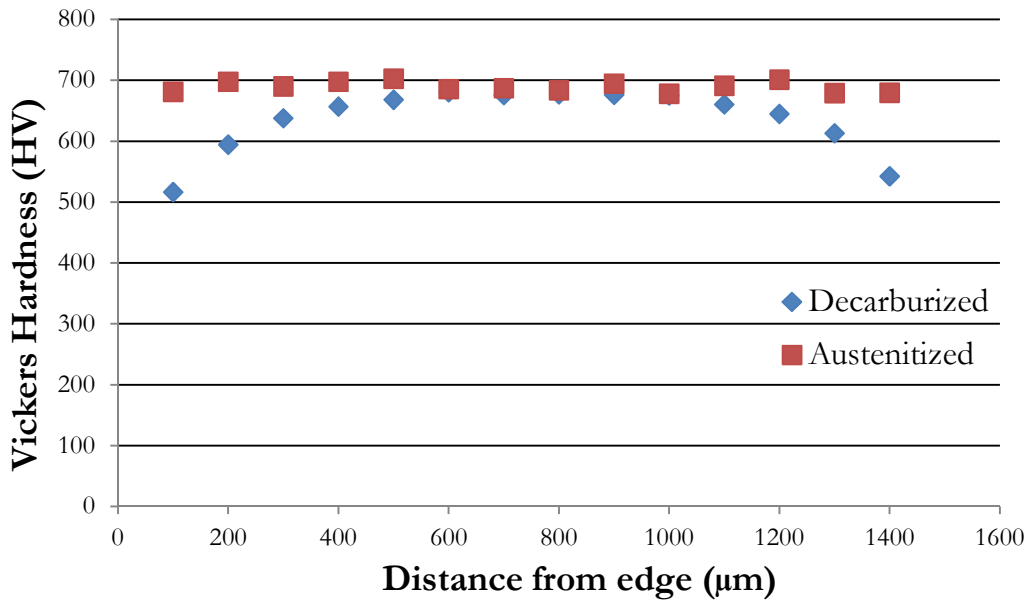
Figure 4.4- (a) Microhardness profiles of 3 decarburized samples under different conditions, (b) Optical micrograph of the centre of a sample decarburized for 15 minutes, (c) Edge of the same sample showing growth of ferrite grains

The above hardness profile and optical micrographs in Figure 4.4 show a clear

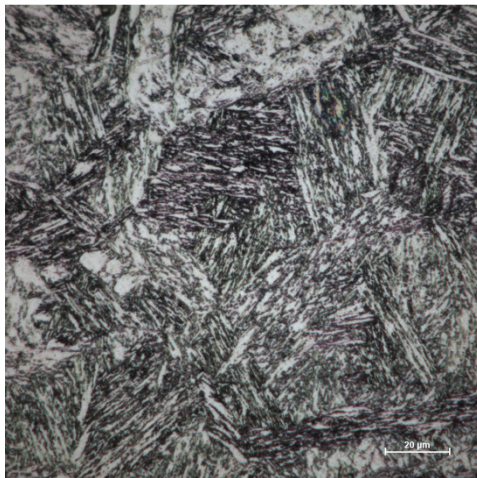
change in the material after decarburization has been performed. There are three hardness profiles, one with just a decarburization and two with a decarburization and re-austenitization. Re-austenitization after decarburization is shown to flatten out the hardness profile because of the diffusion of carbon from the centre of the material to the low carbon edge region at high temperature. The micrographs also indicate the presence of large grains of ferrite on the surface of the material, while the core is martensite. It was not possible to quantify the amount of ferrite using EBSD and XRD methods because of the very small tetragonality of martensite. However, based on morphology and based on the “Image Quality Index” of the EBSD patterns, it is possible to say with confidence that some ferrite was present on the surface.

4.1.2 Higher Carbon Content Grades

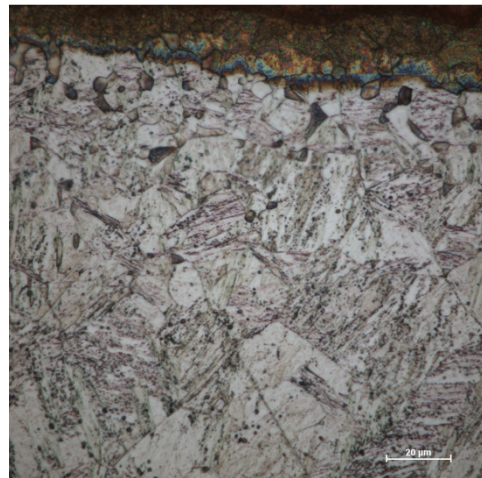
Higher carbon content grades were also characterized. The MA3 and MA4 materials had carbon contents of 0.33%C and 0.44%C respectively.



(a)



(b)



(c)

Figure 4.5- (a) Microhardness profile of an austenitized (homogeneous) MA3 sample and decarburized (graded) sample, (b) and (c) were both etched with Kalling's Reagent. (b) is the core and (c) is the edge of the decarburized sample

Figure 4.5 (a) is a comparison of the microhardness of homogeneous and graded samples. The micrographs show that the homogeneous and core of the graded samples consist of martensite whereas the surface of the graded material appears to be a mixture of ferrite and martensite.

The hardness profile and micrographs again show that decarburization did occur in the MA3 sample. There is ferrite present on the surface of the decarburized material whereas the homogeneous material was martensitic throughout the entire cross section of the sample. This sample was decarburized for 15 minutes at 1100°C.

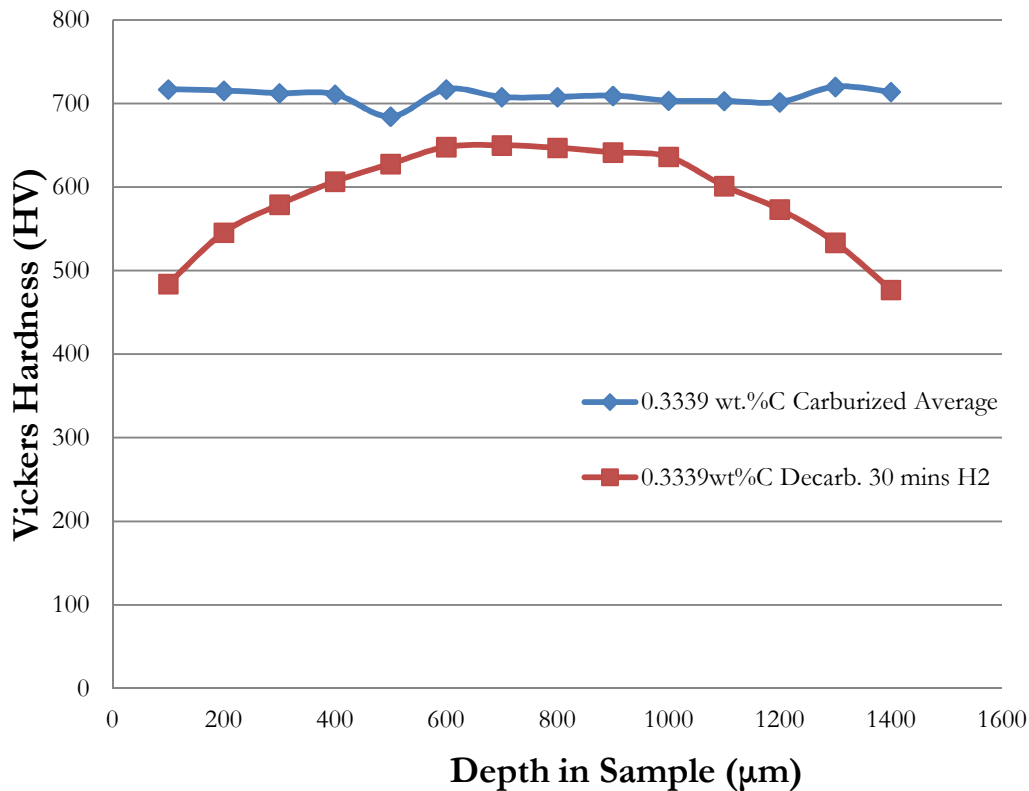


Figure 4.6- Microhardness profile of an MA3 samples that were quenched in oil

The above microhardness profile in Figure 4.6 shows a 0.33%C sample

decarburized for 30 minutes as well as an austenitized and quenched sample. The hardness of the graded material is less in the core than the homogeneous sample. This indicates that for this decarburization time that the core is starting to decarburize as well. This would cause a drastic change in properties, particularly the tensile and Charpy impact tests because the transition from a somewhat ductile material to very brittle occurs in the 0.2%C-0.3%C range.

0.44%C Hardness and Carbon content Profile

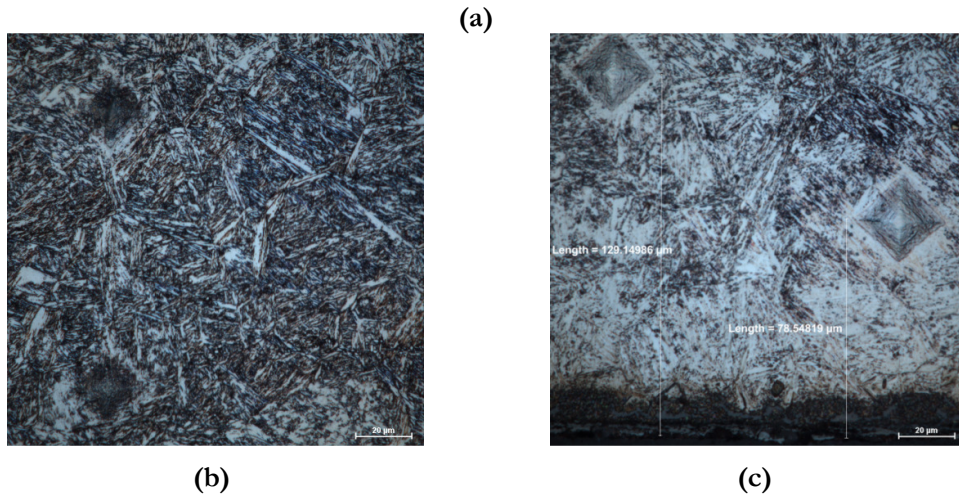
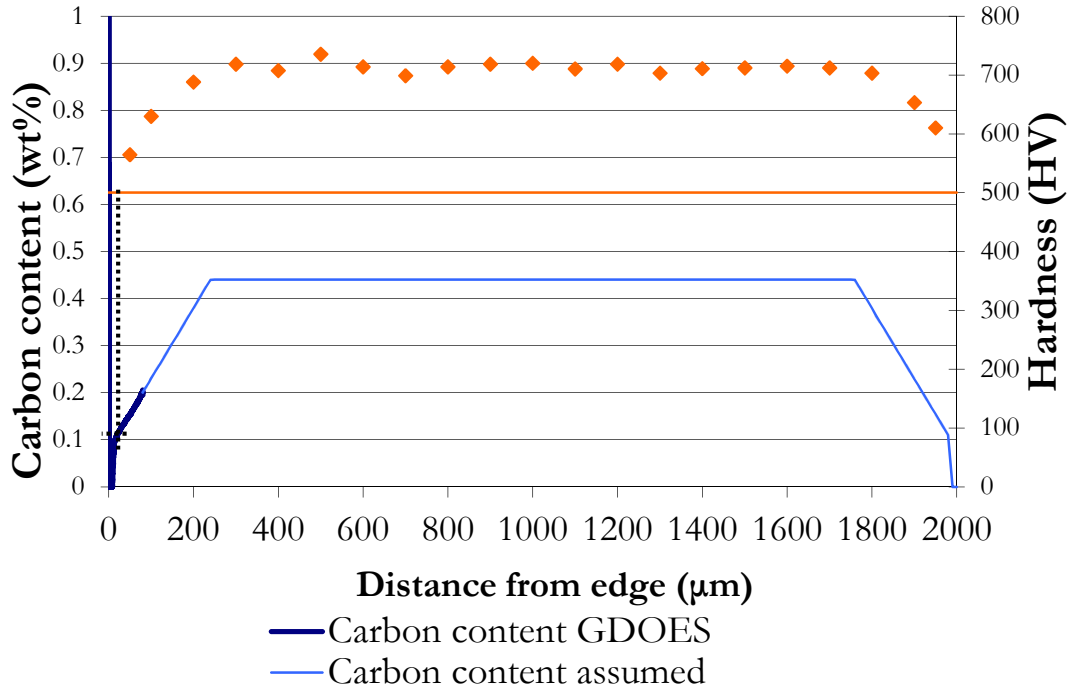


Figure 4.7- (a) GDOES profile with microhardness profile superimposed over it [28], (b) Core of the GDOES sample, (c) Surface of the GDOES sample

The microhardness and GDOES profiles in Figure 4.7 were performed on a sample that was decarburized for 15 minutes at 1100°C in wet hydrogen as can be

seen in Figure 4.7. Using GDOES analysis it can be seen that the sample did actually decarburize to a level of 0.1%C at 50 μ m into the sample. Ferrite and martensite can be seen at the surface of the sample.

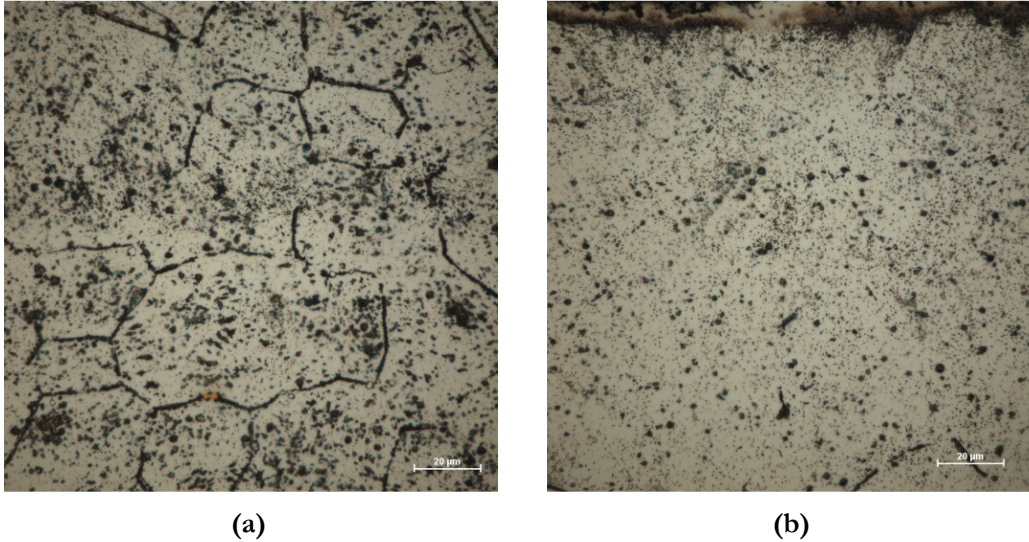


Figure 4.8- (a) Core of MA4 graded and (b) Surface of MA4 graded

The micrographs in Figure 4.8 show a MA4 sample decarburized for 30 minutes etched with Lichtenegger-Bloech 3 reagent. In the core of the material the prior austenite grains can be seen after etching. However, at the edge no grain boundaries are visible. This may be due to the fact that ferrite is the constituent phase. There are also many small carbides formations on the grain boundaries in the homogeneous and graded material.

4.1.3 Transmission Electron Microscopy

Transmission Electron Microscopy (TEM) was performed on MA3 and MA4 samples. This was done to determine whether there was carbide formation in the MA3 sample and whether there was any retained austenite in the MA4 samples due to the high carbon content of the MA4 grade. The MA3 sample was annealed at 1100°C for 24 hours and oil quenched and the MA4 sample was annealed at 1100°C for 24 hours in a glass tube filled with helium and then water quenched.

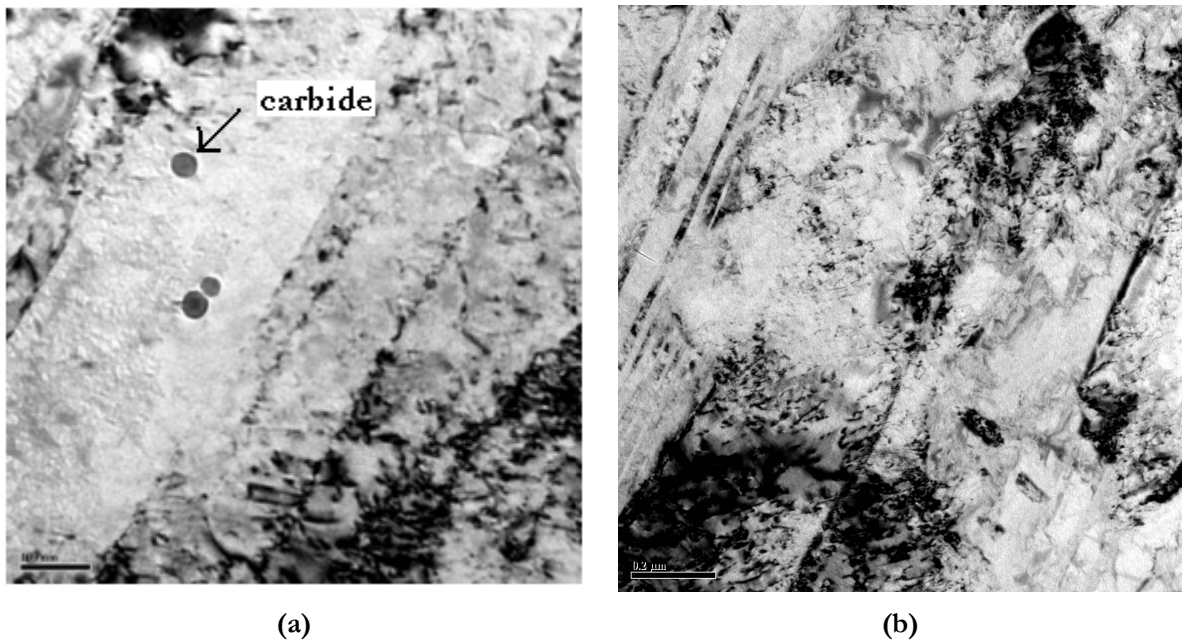


Figure 4.9- (a) and (b) are TEM micrographs of the MA3 sample showing carbide formations and twinning

Figure 4.9 (a) and (b) show fine and large carbide formations in the MA3 sample. 2 variants of martensite were also found, as well as twin martensite.

Figure 4.10 (a) and (b) are the micrographs for the MA4 sample. Retained

austenite was not observed in the sample but 2 variants of martensite were. More twinning is observed within the martensite in the MA4 alloy compared to MA3 alloy.

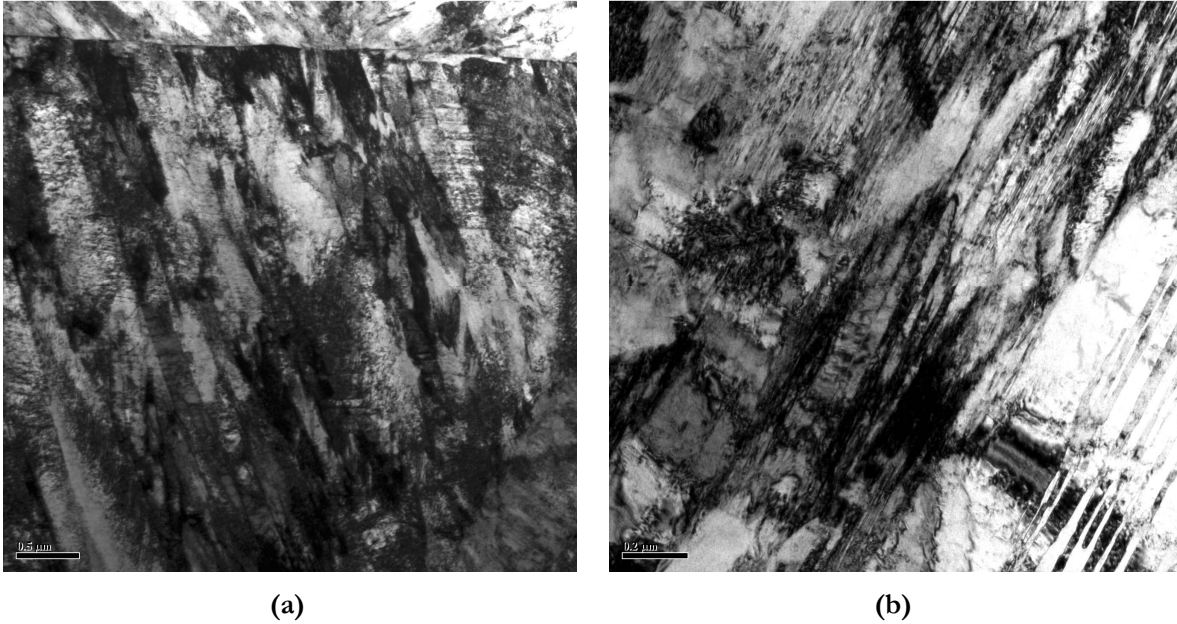


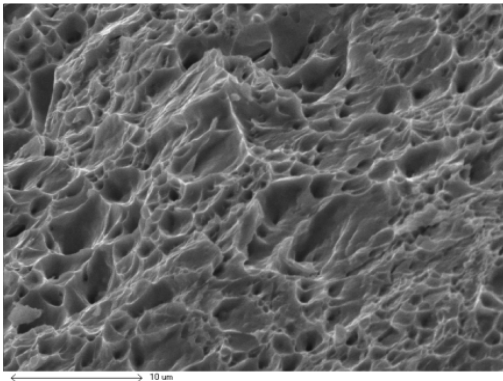
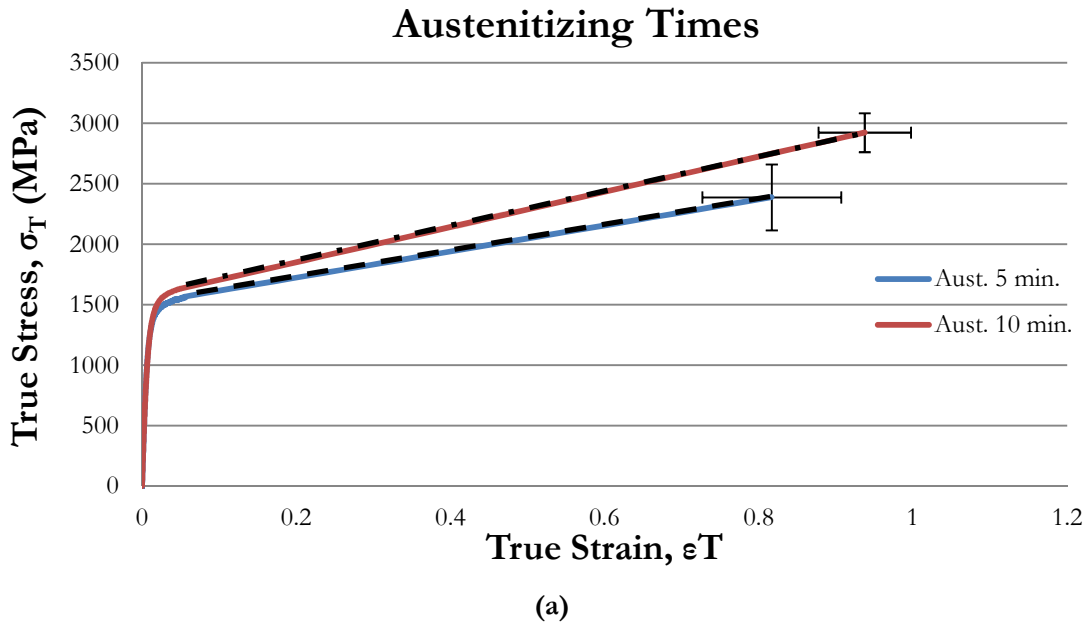
Figure 4.10- (a) and (b) are TEM micrographs of the MA4 sample showing twinning. No retained austenite was observed

4.2 Tensile Testing

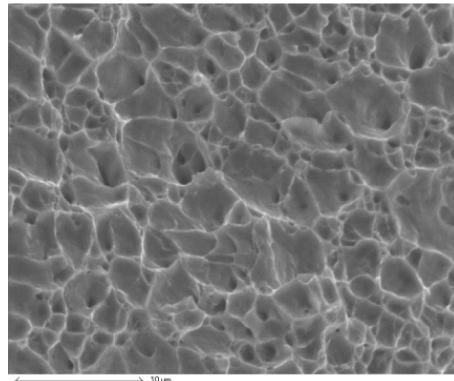
Tensile testing was carried out to evaluate the effect of decarburization of martensitic stainless steel on mechanical properties. This section is organized into two subsections; one on low carbon grades (MA1) and the other on higher carbon grades (MA3 and MA4). All samples had microhardness testing performed on them to ensure an even carbon distribution profile for homogeneous samples and a changing profile for the graded samples.

4.2.1 Lower Carbon Content

- *Effect of Austenitizing Time*



(b)



(c)

Figure 4.11- (a) Tensile curves comparing austenitizing times of 5 and 10 minutes, (b) and (c) are the fracture surfaces of the tensile samples for austenitizing times of 5 and 10 minutes respectively.

The above figure is the true stress-true strain curve that compares the effect of austenitizing time on the tensile properties and the table below. There is a

difference of 500 MPa and a 30% increase in elongation before fracture between the 5 minute and 10 minute samples.

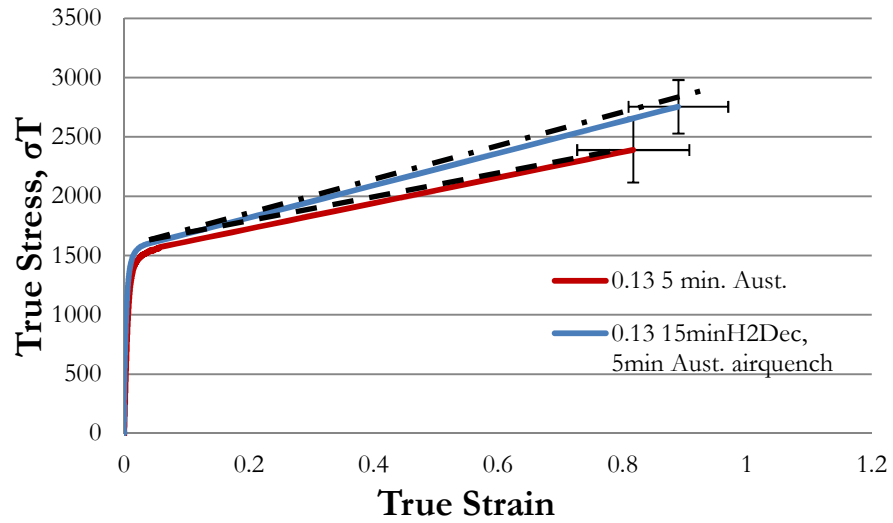
Table 4.1- Summarizes the fracture stress and strains of the MA1 material for different austenitizing times

Austenitizing Time	Fracture Strain (MPa)	Fracture Strain (%)
5 minutes	2390	81
10 minutes	2925	93

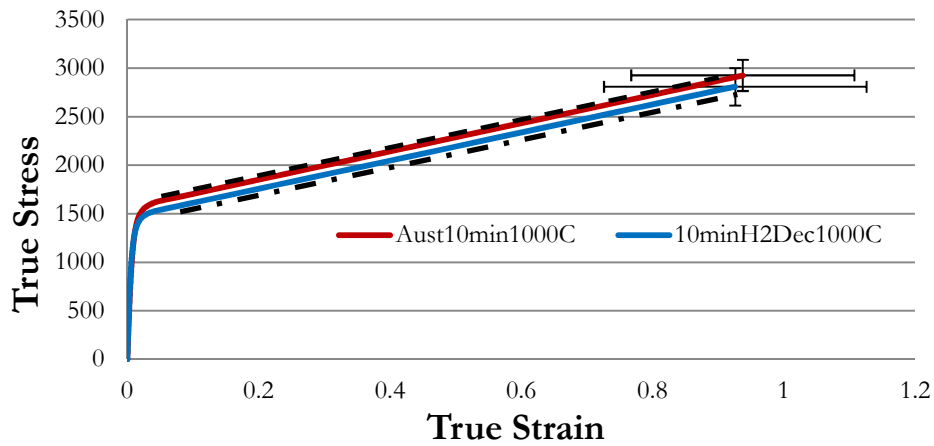
Table 4.1 is a summary of the fracture stress and strain of the different austenitizing times.

A comparison between the homogeneous and graded samples of the same material for the same austenitizing times is shown in Figure 4.12. The curve in Figure 4.12 (a) is for a treating time of 5 minutes and (b) is for 10 minutes. Austenitizing for 5 minutes produces nearly identical results even when the sample has been decarburized and then austenitized.

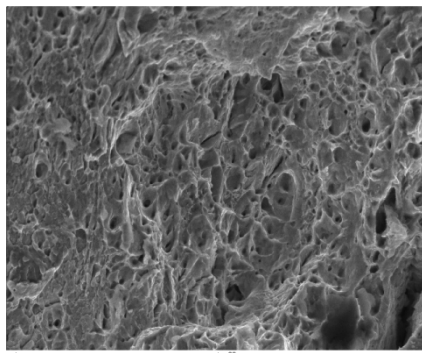
Figures 4.12 (c) and (d) are of the fracture surfaces of the graded samples. The ductile fracture characteristic cup and cone structure is observed in these micrographs. At least 2 samples were tested for each processing condition to verify the results.



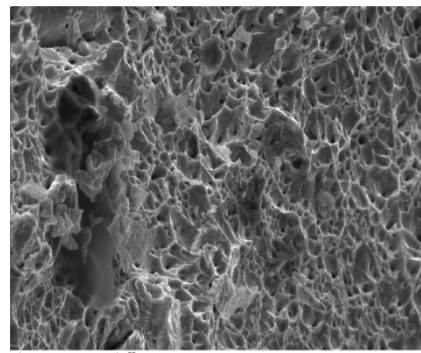
(a)



(b)



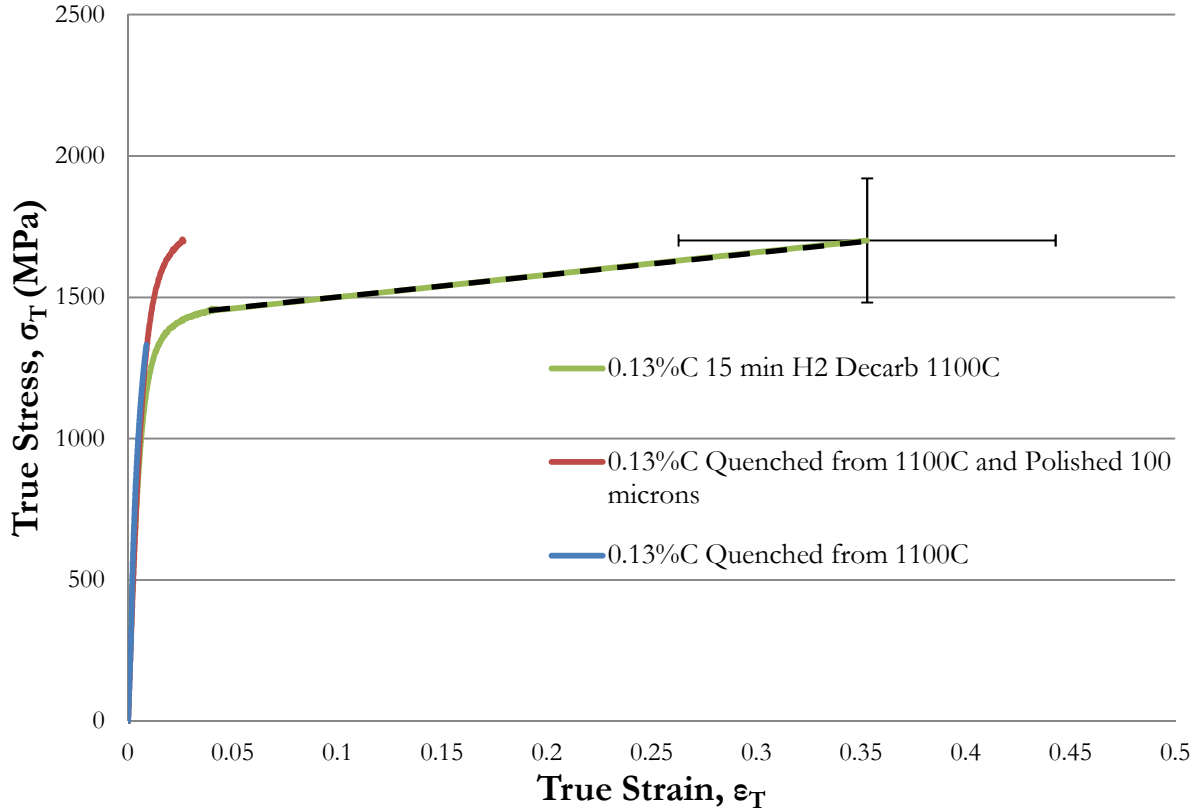
(c)



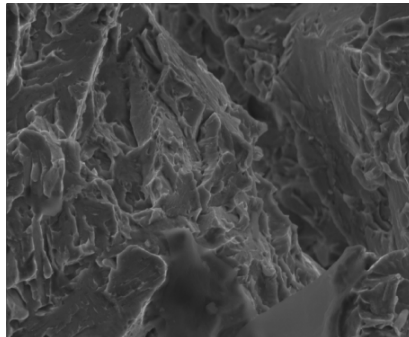
(d)

Figure 4.12- (a) 5 min. austenitization vs. decarburization, (b) 10 min. austenitization vs. decarburization, (c) 15 min wet H₂ decarb, 5 min. re-austenitization and (d) 10 min wet H₂ decarburized fracture surfaces

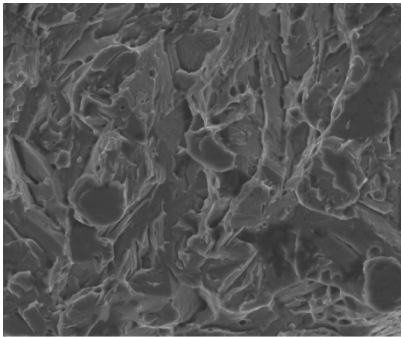
Homogeneous vs. Polished vs. Graded



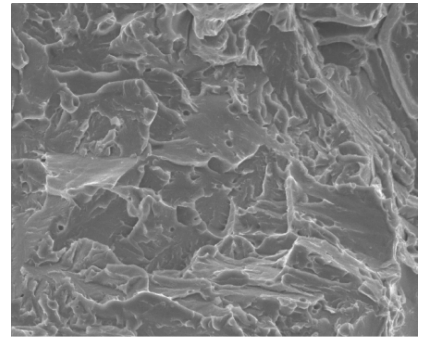
(a)



(b)



(c)



(d)

Figure 4.13- (a) Tensile curves comparing graded, polished and as- quenched samples, (b) Graded, (c) Polished (1620x mag.), (d) Oil Quenched (1550x mag.)

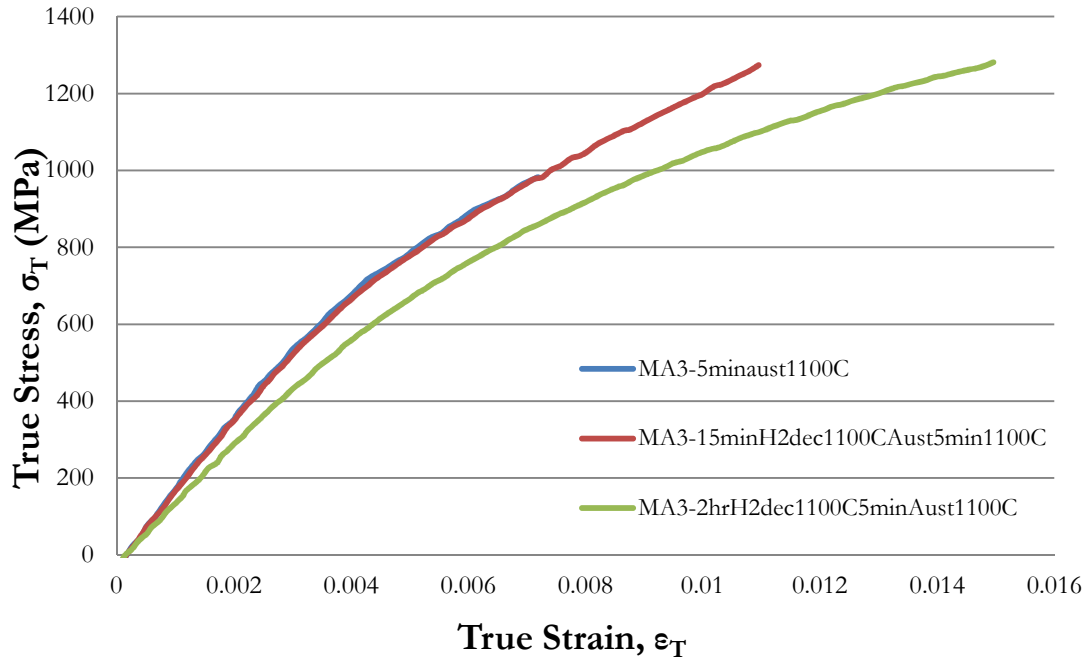
Figure 4.13 (a) is the stress-strain curves that compare oil quenched samples.

The three curves show a decarburized sample, a quenched and polished sample and

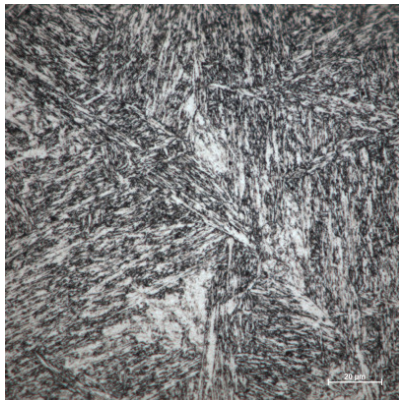
an as quenched sample. Figures 4.13 (b), (c) and (d) are the fracture surfaces for these samples respectively. The as quenched sample did not yield and reached a stress of 1300 MPa before it fractured at 0.9% elongation. The sample that was quenched and then polished 50 μ m on each side yielded and reached a stress of 1700 MPa and fractured at a strain of 2.5%. The polishing that was carried out on the polished samples consisted of successive polishing steps with grits of 320, 800, 1200, 2400 and 4000 μ m. Each step removed 10 μ m of material; this was confirmed through use of a micrometer. The decarburized sample reached a stress of 1700 MPa as well but achieved a much higher fracture strain. It can be seen from the engineering stress-strain curve that the sample started to neck but the fracture mode appears to be intergranular fracture in Figure 4.13 (d).

4.2.2 Higher Carbon Contents (MA3 and MA4)

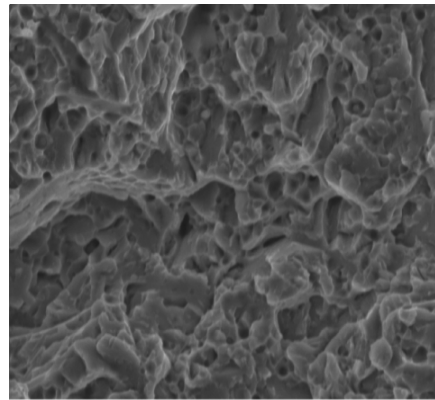
MA3



(a)



(b)



(c)

Figure 4.14- (a) Tensile curves comparing homogeneous MA3 alloy to graded MA3 under 2 different decarburizing conditions, (b) Micrograph of the microstructure of a typical MA3 air quenched sample, (c) Micrograph of the tensile sample fracture surface (3240x)

Figure 4.14 (a) is the tensile curves for a series of air quenched MA3 samples that have all been austenitized for 5 minutes. The blue colour curve is for the homogeneous material, the red curve is for a sample that was decarburized for 5 minutes at 1100°C and the green curve is for a 120 minute decarburization treatment. The homogeneous material reached a true stress of 900 MPa before fracturing at a strain of 0.7%. The graded steels, however, both reached a peak stress of 1300 MPa. The graded sample that was decarburized for 15 min only reached a strain of 1.15% before fracture while the sample that was decarburized for 2 hours reached a strain of 1.5% before fracturing.

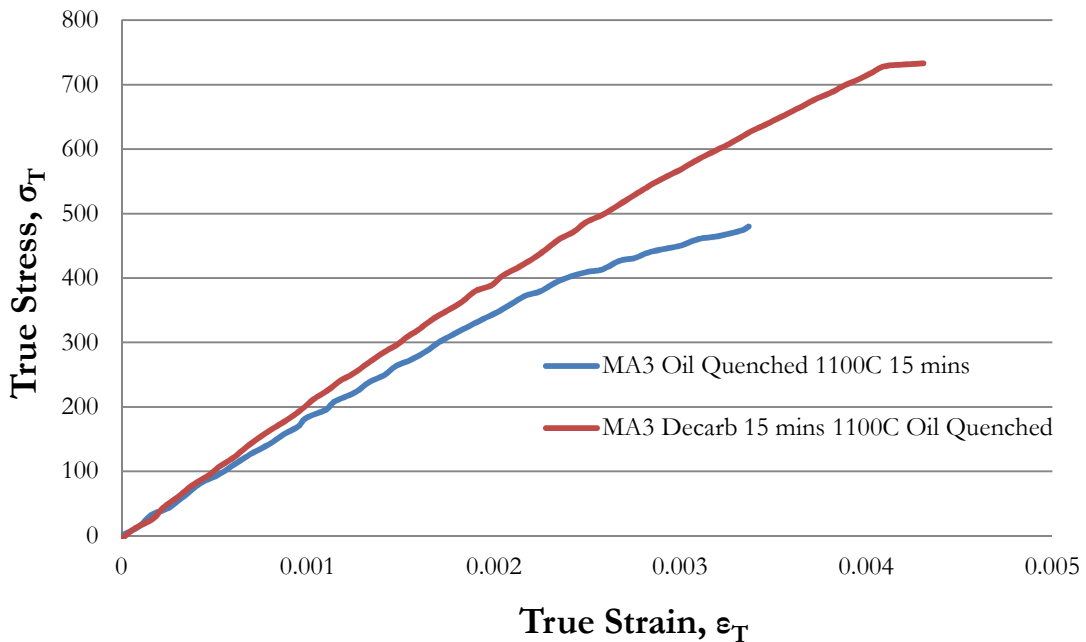
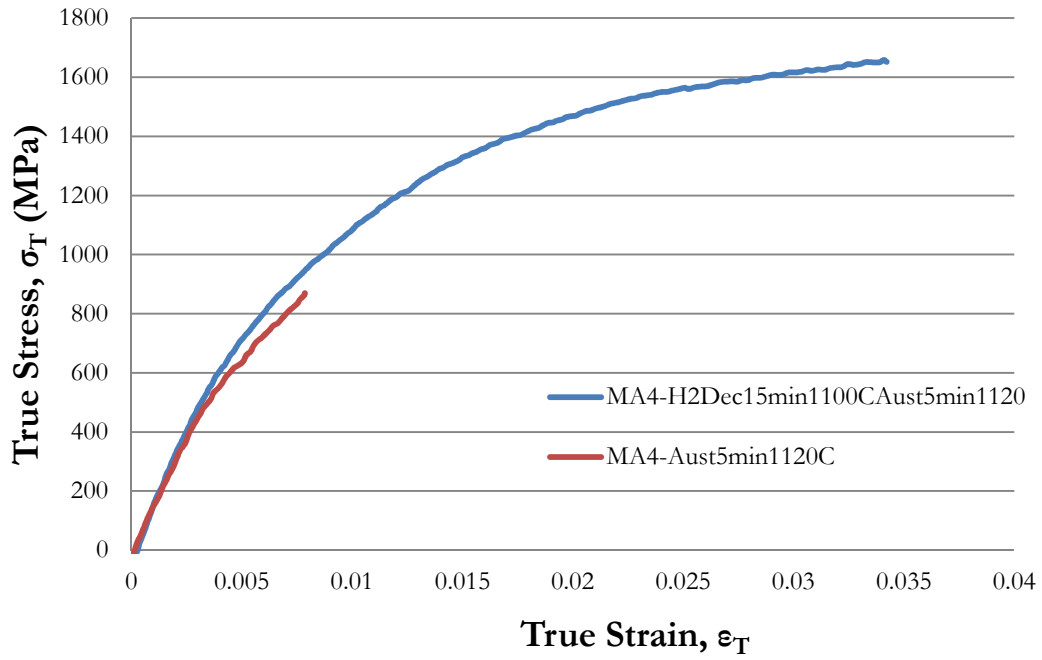


Figure 4.15- Tensile curves for the MA3 homogeneous and graded oil quenched samples

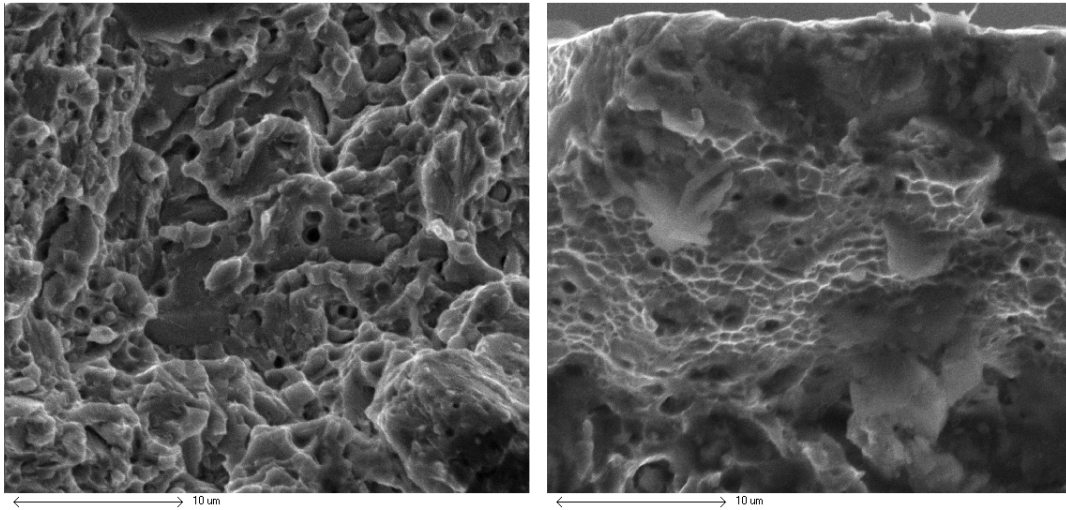
The above curves seen in Figure 4.15 are a comparison between homogeneous sample and graded sample that were oil quenched instead of air

quenched. Again, the graded sample out performs the homogeneous sample both in terms of the level of stress the material reached and the amount of strain it withstood before fracture.

MA4



(a)



(b)

(c)

Figure 4.16- (a) Stress-strain curves for air quenched MA4 homogeneous and graded material, (b) Typical fracture surface of homogeneous and core of graded samples, (c) Fracture surface of the edge of the graded sample

Figure 4.16 (a) is the tensile curves for the MA4 air quenched samples. These samples were cut from a thinner sheet of material to see if thickness of the sample plays a role in the tensile properties of the material. The thin samples clearly deform more and to a higher stress than even the MA3 material, which has a much lower carbon content than the MA4 grade. The MA4 graded material quadrupled the strain achieved by the homogeneous material and achieved a stress of more than double the homogeneous material.

Figures 4.16 (b) and (c) are the fracture surfaces of the MA4 air quenched samples. The homogeneous sample and core of the graded sample show an intergranular fracture surface. However the edge of the graded material shows evidence of some cup and cone formation, as well as intergranular fracture characteristics. Oil quenching was also performed on some MA4 samples to see if decarburization could offer an improvement over a homogeneous. The results are shown below.

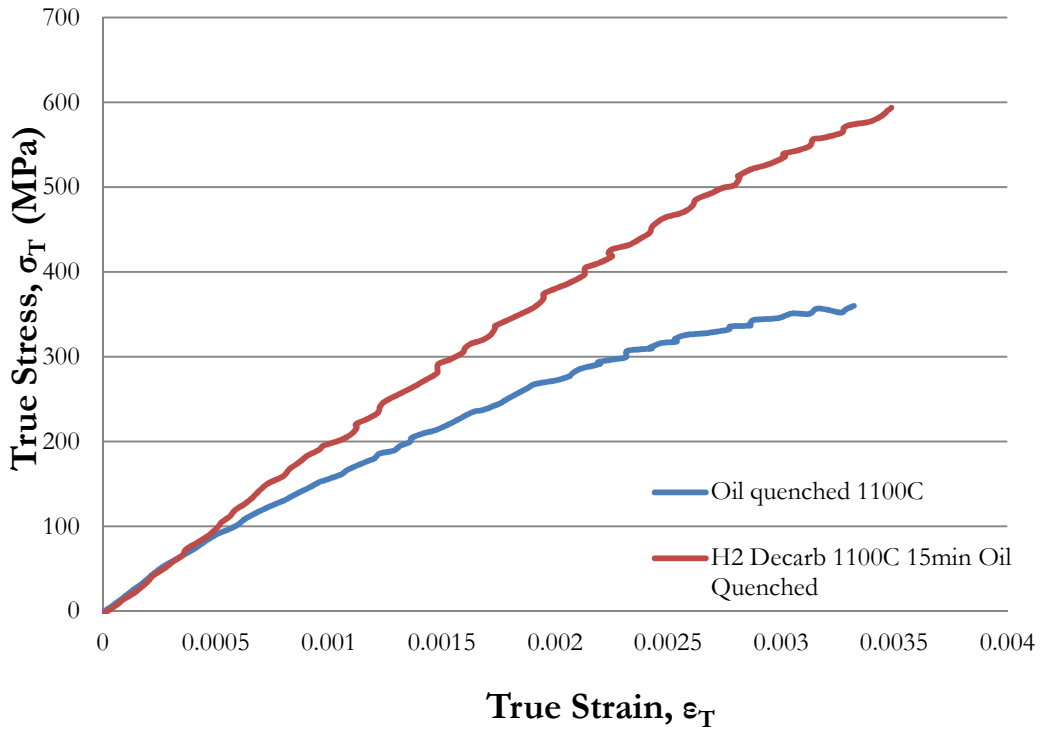


Figure 4.17- Tensile curves for MA4 oil quenched samples

Figure 4.17 is the stress strain curves for the MA4 oil quenched samples. This material achieved a stress level of only 600 MPa in the graded material and 0.34% elongation in the graded and homogeneous samples. These materials are very brittle and showed intergranular fracture as well, like the homogeneous air quenched samples.

4.3 Rolling

Rolling of homogeneous and graded samples was done in order to gauge how decarburization affects the properties of the material under plane strain conditions. Table 5.2 below highlights some of the results obtained from rolling the materials. Decarburization seems to have a profound effect on the rolling properties of the graded material as it increased the percent deformation by more than five times in the oil quenched MA1 samples and 3 times in the air quenched samples. The reduction could have been greater but the samples were too thin to roll with the equipment available. Decarburization also worked well for the higher carbon grades of steel. The material was considered fractured if any part of the sample was cracked (i.e. outer edges or it completely broke apart).

The quenching medium also has an impact on the deformation achieved during rolling for both the homogeneous and graded samples. In all the grades studied the percent increase in reduction is almost exactly two fold in all three cases. This is further evidence that quenching rates play a large impact in the resulting properties of the material.

Table 4.2- Summary of the results of cold-rolling oil quenched and air quenched samples

	MA1 (0.12%)	MA3 (0.33%)	MA4 (0.44%)
Oil Quench	Homogeneous 0.38, Decarburized >1.76	Homogeneous 0.18, Decarburized 0.16	Homogeneous 0.015 Decarburized 0.015
Air Quench	Homogeneous 0.75, Decarburized >1.76	Homogeneous 0.36 Decarburized 0.96	Homogeneous 0.0289, Decarburized with Wet Hydrogen 0.34, Decarburized with 0.1%C on the Surface 0.24, Decarburized with 0.15%C on the Surface 0.146

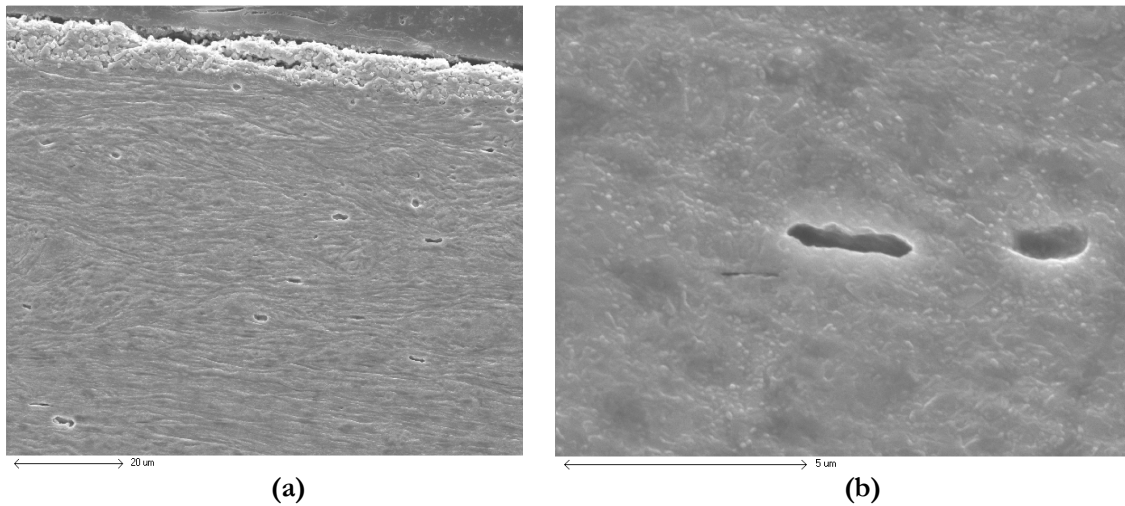


Figure 4.18- (a) and (b) are SEM images of the rolled MA1 samples at 1200x and 9600x magnification, respectively

Figure 4.18 (a) and (b) are SEM micrographs of a rolled MA1 sample to 100% deformation. Cracks in the material can be observed to be forming. It appears from these micrographs that failure in plane strain starts at the surface, as

that is where the most cracks started to appear. Some samples of homogeneous MA1 were rolled past the point of when they started to “break” to strains as high as 1.52. Measurements of how deformation affected microhardness were taken at intervals of 0, 0.25, 0.5, 0.75, 1, 1.25 and 1.52. Figure 4.19 shows the results of these experiments. At a strain of 0.25, the materials hardness reaches a peak of 565 HV. But at a strain of 1.3 there is a big jump in hardness to 607 HV and another increase at a strain of 1.52 to a hardness of 623 HV. This indicates that geometric hardening may in fact be occurring in this material

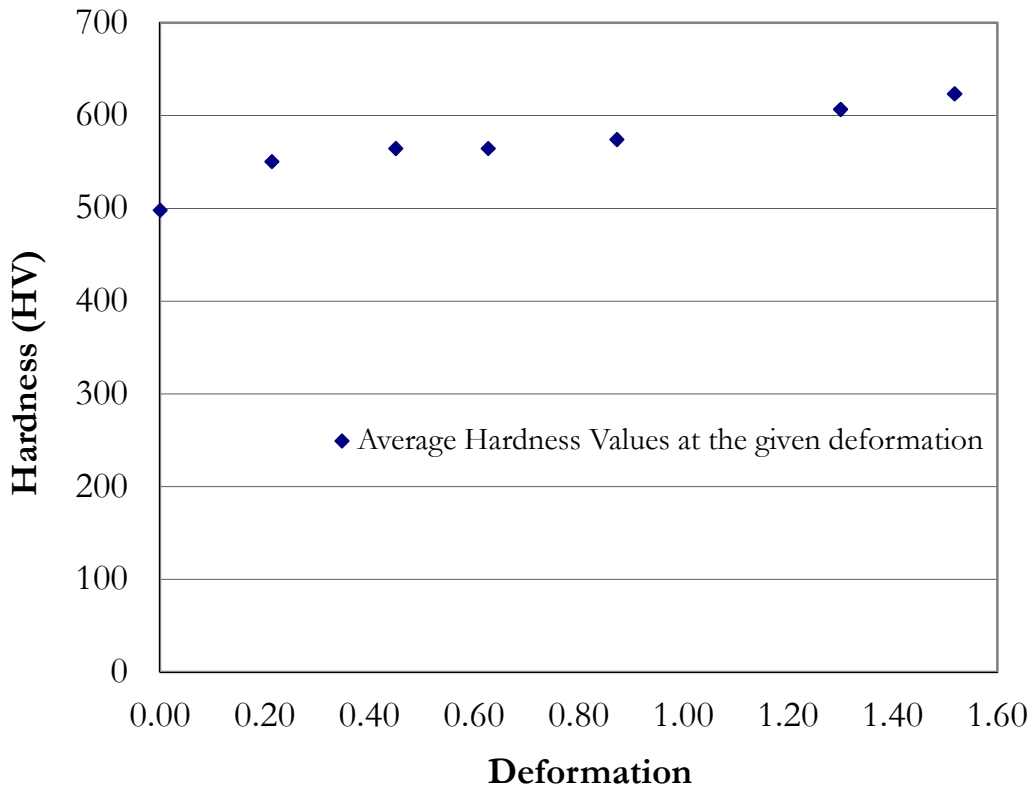


Figure 4.19- Microhardness vs. deformation plot of homogeneous MA1 cold rolled to a high strain

4.4 Charpy Impact Testing

Charpy impact testing was performed on two grades of martensitic stainless steel, MA1 and MA3.

Table 4.3- Summary of the Charpy impact tests performed on homogeneous samples and graded samples of the MA1 and MA3 alloys

	0.12%C Homogeneous (Toughness [J/cm ²])	0.12%C Graded (Toughness [J/cm ²])	0.33%C Homogeneous (Toughness [J/cm ²])	0.33%C Graded (Toughness [J/cm ²])
Oil Quench	11.7 (RT), 6.7 (-40°C)	20.8 (RT), 5.8 (-40°C)	Not Available	Not Available
Air Quench	17.1 (-40°C)	50.7 (-40°C)	7.5 (RT)	9.2 (RT)

Table 4.3 shows the toughness values of the Charpy impact tests. Homogeneous and graded samples were prepared to test how decarburization affected toughness values. Samples were also created to test the effect of quenching medium. Decarburization was shown to have a large effect on the toughness values at room temperature in the oil quenched samples and at low temperature in the air quenched samples for the MA1 grade. It did not offer an improvement in the MA1 oil quenched samples tested at low temperature in the MA1 however. The air quenched MA1 samples were only tested at low temperature because of limited number of samples.

The MA3 grade was only tested using air quenched samples at room

temperature. It can be seen from the table that this did not offer an improvement in toughness. The MA3 was not tested in the oil quenched condition because it was observed from tensile tests that the material was just too brittle, even with decarburization

Figures 4.20 and 4.21 show the microhardness profiles of the impact samples. These show that the graded samples did in fact decarburize.

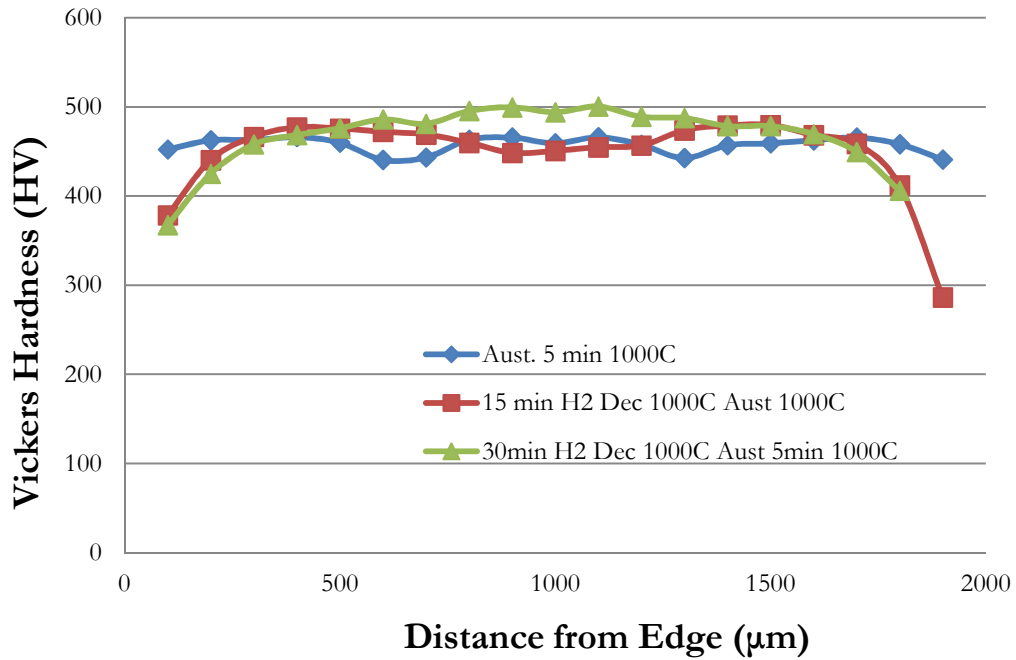


Figure 4.20- Microhardness profiles of the MA1 Charpy impact samples

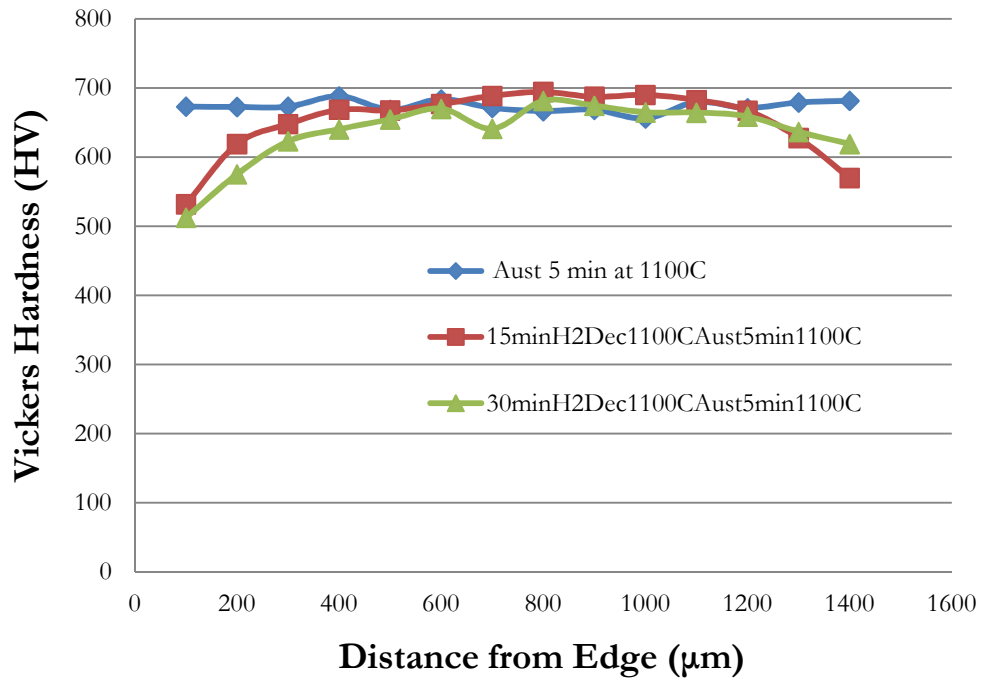


Figure 4.21- Microhardness profiles of the MA3 Charpy impact samples

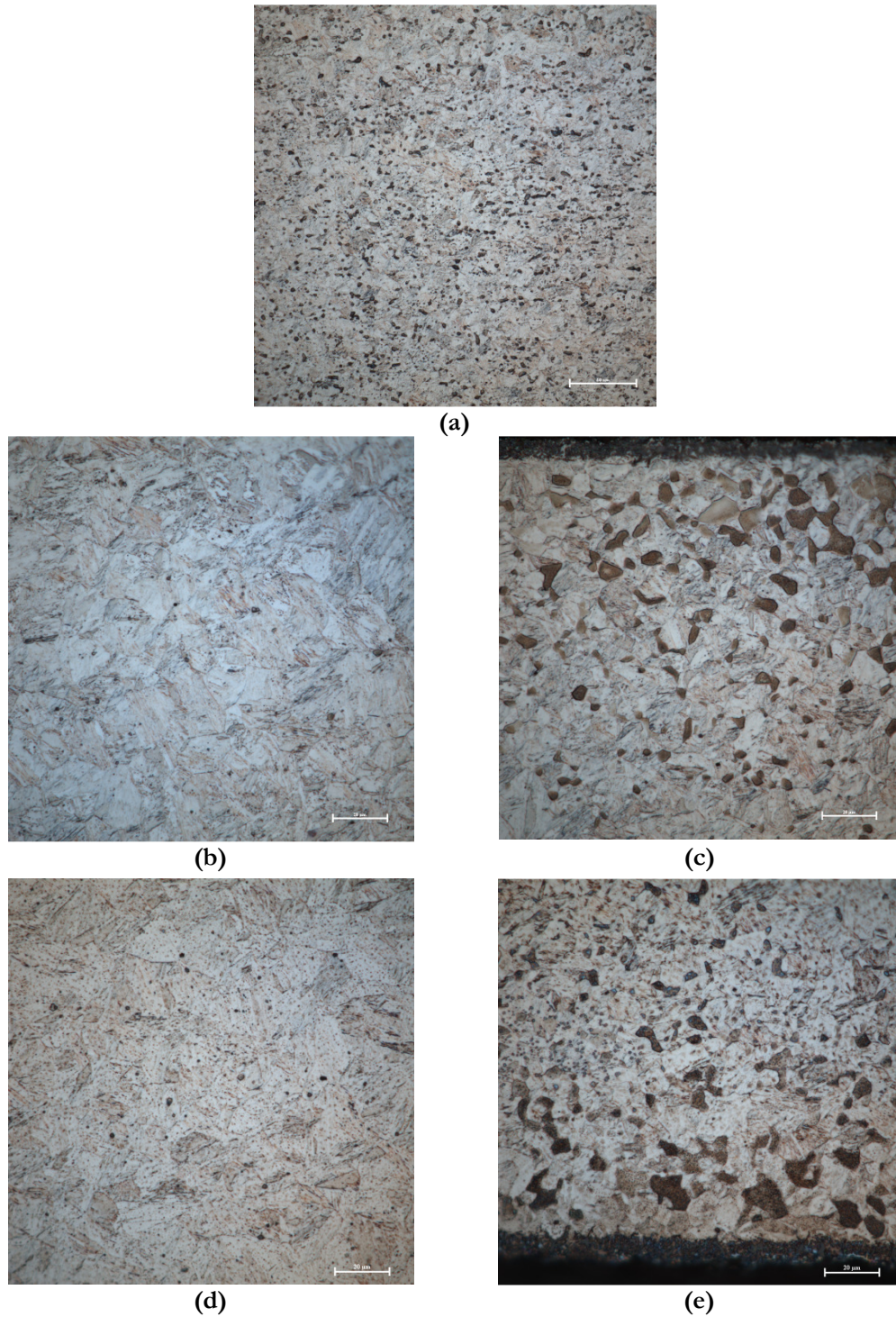
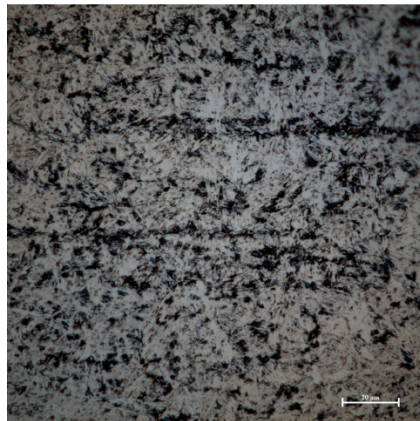
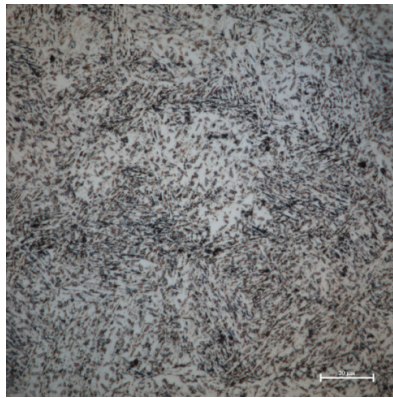


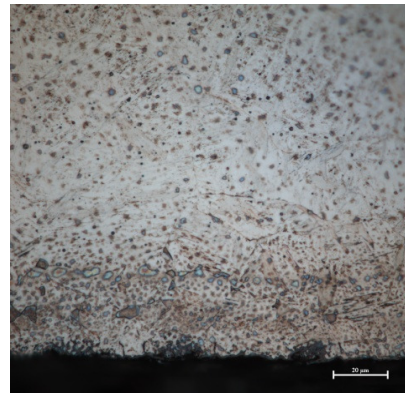
Figure 4.22- (a) MA1 austenitized, (b) MA1 H₂ decarburized 15 min austenitized 5 mins 1000°C centre, (c) MA1 H₂ decarburized 15 min austenitized 5 mins 1000°C Edge, (d) MA1 H₂ decarburized 30 mins 1000°C centre, (e) MA1 H₂ decarburized 30 mins 1000°C edge



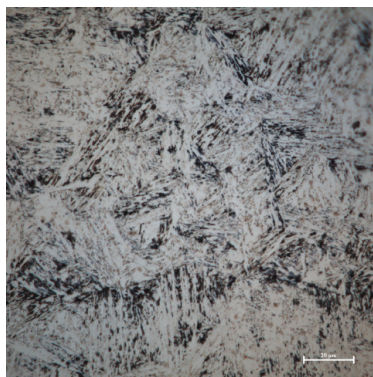
(a)



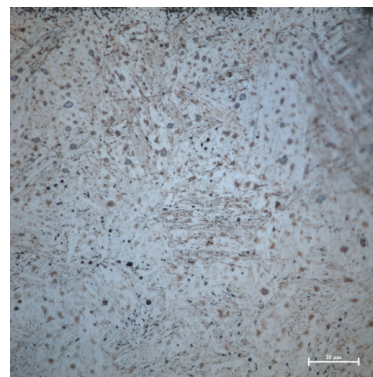
(b)



(c)

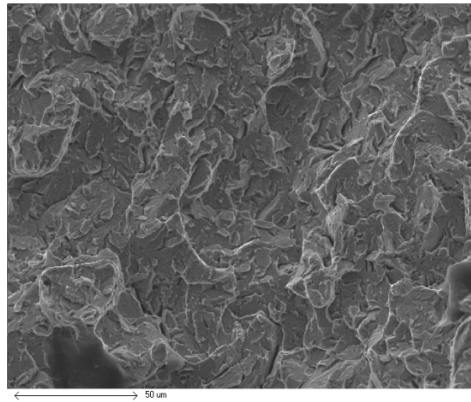


(d)

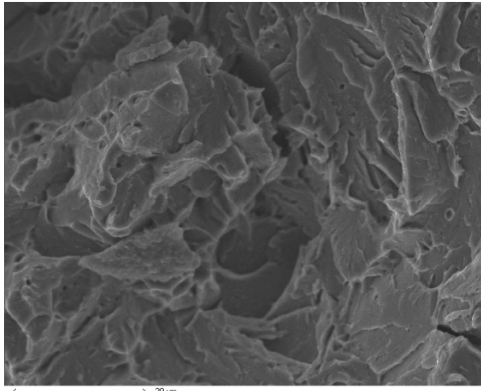


(e)

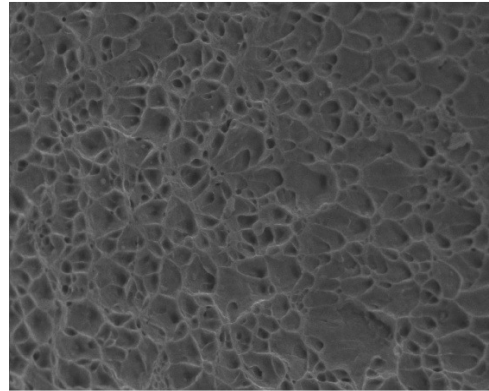
Figure 4.23- (a) aust 5min 1000C, (b) MA3 H₂ decarburized for 15 mins at 1000°C aust. 5 min 1000°C core, (c) MA3 H₂ decarburized for 15 mins at 1000°C aust. 5 min 1000°C surface, (d) MA3 H₂ Decarb 30 mins core (e) MA3 H₂ decarb 30 mins surface



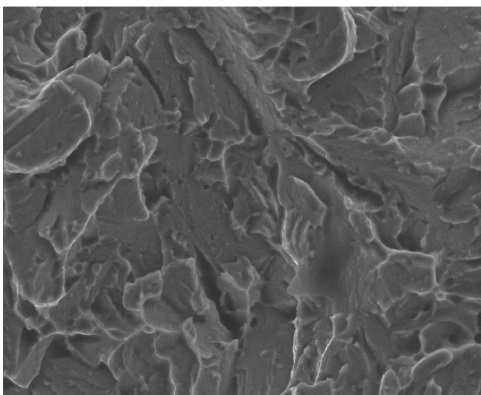
(a)



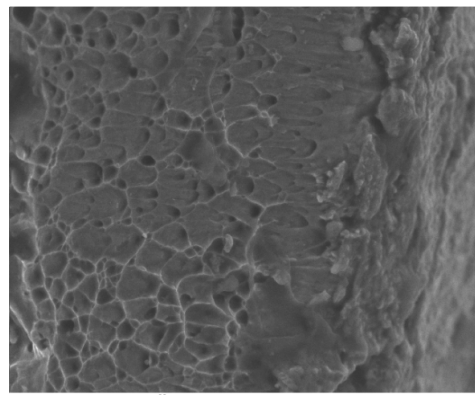
b)



c)



d)



e)

Figure 4.24- (a) aust 5min 1000°C, (b) MA1 H₂ decarburized for 15 mins at 1000°C aust. 5 mins at 1000°C core, (c) MA1 H₂ decarburized for 15 mins at 1000°C aust. 5 min 1000°C surface, (d) MA1 H₂ Decarb 30 mins. at 1000°C core (e) MA1 H₂ decarb 30 mins. at 1000°C surface

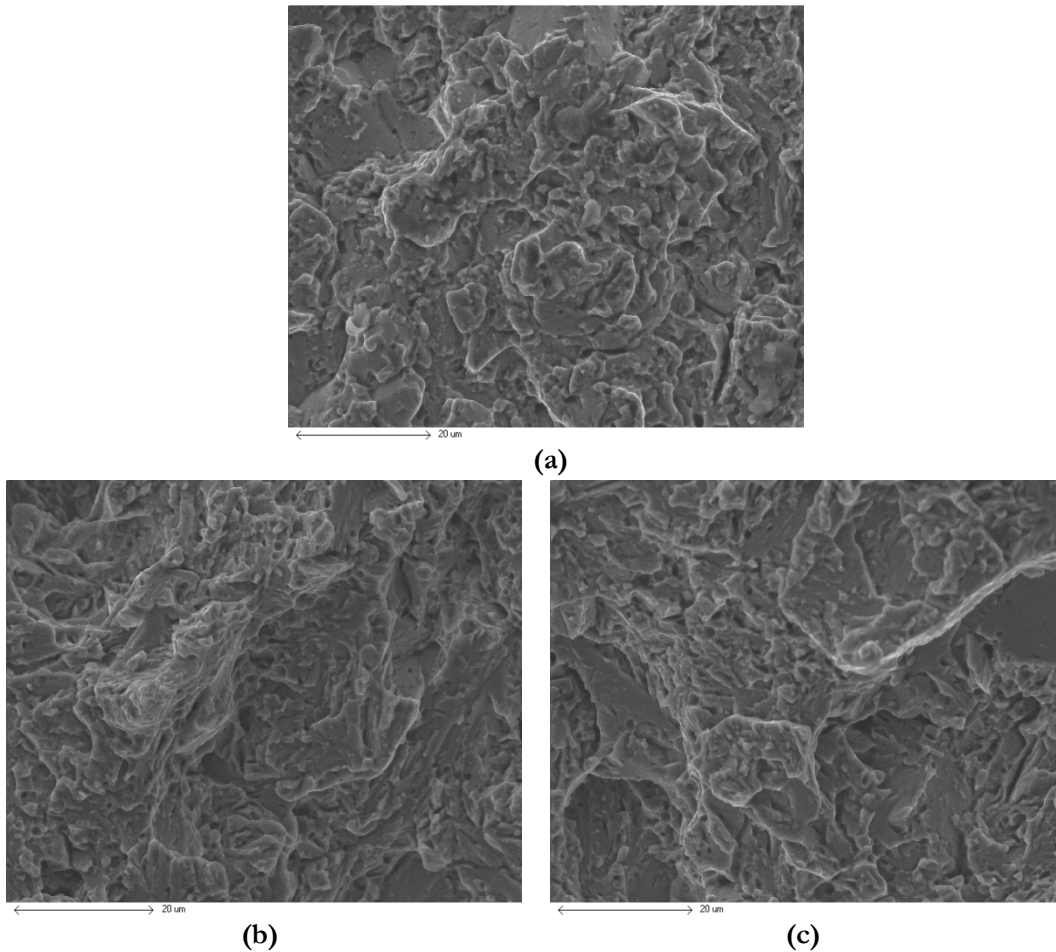


Figure 4.25- (a) MA3 austenitized, (b) MA3 decarburized 15 mins, aust. 5 mins, (c) MA3 decarburized 30 mins.

Figures 4.22 and 4.23 show optical micrographs of the MA1 and MA3 impact samples microstructures, respectively. The micrographs show that there is a layer of ferrite at the surface of the material in the MA1 samples and martensite in the core. There are no visible ferrite grains in the MA3 impact samples but there is an absence of martensite on the surface while martensite is visible in the core.

Figures 4.24 and 4.25 are SEM micrographs of the fracture surfaces of the air quenched MA1 and MA3 Charpy impact samples, respectively. The graded MA1 samples show intergranular fracture in the core of the material and cup and cone

structure, which is indicative of ductile fracture on the surface of the material as seen in Figure 4.23 (c) and (d). The austenitized MA1 samples showed only intergranular fracture in the core and at the surface of the samples, which indicates decarburization has a big effect on the fast fracture properties of the graded material.

The MA3 samples all showed intergranular fracture in the austenitized and decarburized samples. This shows decarburization did not impact the fast fracture properties of the MA3 grade, which is reinforced by the toughness values obtained during the impact tests.

Chapter 5

Discussion

The purpose of the discussion section is to explain the results section and evaluate the validity of the results or point out the strengths and weaknesses of the experimental methods used. Reasons for performing certain experiments are provided and an explanation of a model that was created for this work will be provided as well.

5.1 Characterization

Characterization of the homogeneous and graded materials was performed in order to determine how different processing conditions affected the resulting properties of the materials. Characterization also allowed a comparison between the graded and homogeneous materials. These results provided direction for possible

future experiments and allowed an explanation of results obtained from past experiments.

Different austenitizing times were tested to see if significant decarburization would occur in the MA1 grade at high temperature in an argon atmosphere. Results from these experiments showed that the hardness was essentially the same which indicates that little to no decarburization occurred. This is different from earlier work on low alloy steels. The difference between this work and the previous work on low alloy steels may be due to the oxide layer that forms on the surface of the stainless steel studied in this work.

In highly decarburizing atmospheres, such as wet hydrogen, some of the oxygen reacts with carbon. In previous work the wet hydrogen decarburization removed all the carbon in low alloy steels but in the stainless grades the carbon content at the surface of the graded materials was not zero. This was observed through GDOES and in optical micrographs in which martensite was still found at the surface of the material. This formation of martensite can only occur if carbon is present at the surface. The reason for the difference between the low alloy steels and the stainless steels is that the stainless steel may not have a bulk diffusion controlled reaction but a surface controlled reaction due to the formation of the chromia layer on the surface. This reaction limits the rate at which carbon diffuses out of the material or oxygen diffuses into the material. This is advantageous because the resulting phase that forms is a ferrite and martensite dual phase region. This inhibits the formation of columnar ferrite grains at the surface, which are detrimental to

mechanical properties. Instead, the superior dual phase microstructure that forms provides superior mechanical properties.

Austenitizing was also tried after decarburizing for a couple of reasons. The first was to refine the grain structure of the graded material and to optimize the resulting hardness of the graded materials. The different times and temperatures that were used are based on the work of de Alvares and Garcia [14]. The second reason to austenitize the graded materials is because it allows for control of mechanical properties through a moderation of the carbon gradient through diffusion. This method can be used to re-harden the surface of the material if necessary.

The effect of quenching rate was also investigated using quenching oil and pressurized air. The two different quenching media produced materials with different microhardness, as can be seen in Figure 4.2. The oil quenched materials had a higher hardness profile than the air quenched materials. This may be due to the fact that autotempering and stress relaxation might have occurred in the air quenched samples because of the slower quenching rate. No pre-existing cracks were observed in the oil quenched or air quenched samples, which indicates the benefit of air quenching seen in the mechanical properties are obtained through stress relaxation as opposed to the elimination of quenching cracks.

5.2 Tensile Testing

Tensile testing led to several interesting results. As expected, when longer austenitizing times are used, the ductility of the material increases, as seen in Figure 4.11 (a). Austenitizing for 10 minutes led to an increase in elongation and also an increased fracture stress. This may be due to increased carbide dissolution, which led to the greater ductility observed in the samples that were austenitized for 10 minutes. Because fewer carbides were present on grain boundaries, the material fractured at a larger strain and higher stress. It is well known from [40] that fracture in martensitic stainless steel occurs along grain boundaries, a place where carbides are highly likely to segregate.

It is possible to see in Figure 4.12 (b) that the decarburized samples had a slightly lower yield-strength than the homogenous material, which is to be expected given the fact that removing carbon will decrease the yield stress of the surface layer. Beyond that, it appears that decarburization for 15 minutes had a minimal effect on the tensile behaviour. This is to be contrasted with the great improvement of properties of the decarburized material during rolling and impact testing. This would suggest that in the case of rolling and impact testing the condition at the surface and crack-tip, respectively, control the damage process; the important effect of decarburization on rolling and impact testing is therefore due to its effect on surface properties.. In contrast, the only effect of decarburization on tensile testing was to reduce the yield stress by an amount proportional to the volume of decarburized

material. Given that the decarburized layer was only of the order of 300um compared to sample cross section of 3x1.5 mm² and given that the hardness of the surface was 350 HV vs. 500 HV at the core, one does not expect decarburization for 15 minutes to dramatically change the strength of the sample. Neither does it change the failure mechanism because the material appears to fail in a ductile manner due to defects that initiated on the former austenite grain boundaries in the interior of the sample

The second reason for this increase is that the decarburization creates a residual compressive stress in the core when the sample is quenched. During the test, the material must first break the compressive stress that was created before it can begin tensile deformation. Again this could produce a more pronounced effect in the sample that was austenitized for 10 minutes because of the different grain size. Another processing parameter that has an important impact on the resulting tensile properties is the quenching media used.

In addition to forced air-cooling, oil quenching was examined. The oil-quenched samples failed at much lower stresses and strains compared to the air-cooled samples. This is attributed to quenching stresses that develop during fast quenching in oil but not slow quenching in air. The presence of these large stresses and potentially, the presence of microcracks provided an opportunity to investigate the use of decarburization as a potential method of reducing the negative impact of quenching stresses. Figure 4.13 shows that polishing and/or decarburizing improves/restores the strength and ductility of the oil quenched material. It is

believed that quenching in oil produces large tensile stresses at the surface [30]. Figure 5.1 is a quench crack in AISI 403 stainless steel. This is a very severe crack that occurred after quenching a forged sample.



Figure 5.1- Quench crack in forged AISI 403 martensitic stainless steel [30]

Polishing the samples after oil quenching removes these stresses and eliminates potential crack-formation sites. As a result, the strength and ductility are both improved. Decarburizing also helps by introducing a ductile layer on the surface of the material. This ductile layer is less vulnerable to the nucleation and growth of cracks and helps delay their advancement into the brittle core of the material.

While decarburization did not show a very good improvement in tensile

properties in the low carbon grades compared to the optimal austenitizing condition, good results were seen in the higher carbon content MA alloys. Figures 4.14 and 4.15 show the tensile curves for the MA3 air quenched and oil quenched samples. In both cases of air and oil quenching, decarburization produced improved tensile properties. However, the MA4 showed a big improvement between homogeneous and decarburized materials when thin tensile samples were used, as can be seen in Figure 4.16 (a). The decarburized sample reached a much higher stress and strain. Figure 4.16 (c) also shows some evidence of ductile fracture occurring, whereas the homogeneous sample fractured completely intergranularly. The reason for the large increase in tensile strength and elongation in the MA3 and MA4 alloys is that these alloys are much more brittle due to their high carbon content. Decarburizing the surface leads to a much tougher material which would better resist the nucleation and growth of surface cracks. In addition, the resulting “composite” will carry a lower stress for any given strain compared to the homogeneous material and consequently the graded material/composite will fail at a large strain compared to the homogeneous material. An additional effect might be related to the presence of the carbon gradient which in turn leads to a yield stress gradient. It was shown by Kolednik [32] that the energy absorbed during fracture is increased when the crack grows into a positive yield stress gradient.

Interestingly, the results on the MA3 and MA4 samples seem to suggest that benefit of decarburization is related to the absolute value of the sample thickness. To understand this point, it is worth keeping in mind that the MA4 is expected to be

more brittle than the MA3 due to its higher carbon content. However, the MA4 specimen which was 1 mm thick showed much higher ductility compared to the MA3 specimen that had 3mm thickness. This effect might be related to the change in stress state in the thin sample compared to the thick one. It might also be related to the residual stresses that develop during quenching. The core of a quenched martensitic graded material will usually be under compression. The magnitude of the residual compressive stresses in the thin sample are larger than those of the thick one and this might help delay the fracture of the martensitic core.

5.3 Rolling

Graded martensitic stainless steel showed a great improvement over the homogeneous martensitic steel. The graded samples, for the vast majority of cases, showed an improvement in the strain that could be achieved before the onset of necking. In the more ductile grade (MA1), decarburization had a large impact in both the oil quenched and air quenched samples. However, decarburization did not have an impact at all on the rollability of the high carbon grades (MA3 and MA4) when they were oil quenched. But when the high carbon grades were air cooled there was an incredible improvement in the ductility of the graded samples over the homogeneous samples, as high as 12 times the amount of deformation was achieved in the graded samples. Air quenching the samples produced softer martensite which withstood a higher amount of deformation than the oil quenched samples.

These results also lead to the conclusion that there are two groups of samples that fail. The first group is the one in which the samples experience crack formation on the surface. Thus, decarburization would prohibit the advancement of cracks that formed on the surface because of the ductile layer that forms. This results in a significant increase in the strain that the material could withstand and leads to the vast improvement of the mechanical properties in plane strain. The second group is the samples that saw no improvement in the plane strain mechanical properties. These samples might have failed due to internal crack formation in the martensitic core. Therefore, decarburization would have no impact on the mechanical

properties because the stress that the rolling would have induced on the internal cracks would have been high enough to cause the brittle martensitic core to fracture.

It seems from these results that air quenching produces a martensite that is much softer than the oil quenched samples, as well as martensite that has fewer internal cracks in the core of the material. Figure 4.17 is a micrograph of a rolled oil quenched MA1 sample that has numerous internal cracks in the bulk of the material. These internal cracks would raise the stress level in the material sufficiently to cause fracture in the oil quenched samples before the air quenched samples.

5.4 Charpy Impact

Charpy impact testing was carried out to determine how graded stainless steels behave under very high strain rates and assess their fast fracture properties.

The MA1 grade showed the greatest improvement in impact tests between the homogeneous and graded samples in the air quenched and oil quenched samples as can be seen in Table 5.2. This is because the graded samples had a layer of tough material on the surface around the notch. This allowed for more energy absorption. Decarburization is also shown in the micrographs of the fracture surfaces. The core showed intergranular fracture whereas the edge has cup and cone structure, indicative of ductile fracture.

There is also a large difference between oil quenched and air quenched samples, irrespective of whether they had been decarburized or not. This may be due to the fact that air quenching produces a material with lower internal stress than oil quenching, which would allow for more energy absorption. Another reason is the amount of brittle or the amount of tough phase present on the surface due to the quenching rate. Of course the contrast between oil and air quenching is magnified when the homogeneous and decarburized samples are compared, with the greater difference due to decarburization coming in the air quenched samples than in the oil quenched samples.

A very noticeable difference is seen between energy absorption when the

processing condition are compared at room temperature and low temperature. The decrease in energy absorption occurs in low temperature tests because of martensite and ferrites's ductile to brittle transition temperature. When these phases are cooled below the DBTT, the mechanical phases are drastically affected which leads to the results that have been observed

5.5 Model

This section will discuss a proposed model that will attempt predict the mechanical response of a functionally graded material when a tensile load is applied to the material. This model hopes to find the optimum carbon distribution in the material that yields specific properties. An example of this would be to maximize the strain in the material, while ensuring the stress in the material would not reach the fracture stress. This is achieved by controlling the distribution of carbon in the material.

The section will be broken up into 3 sections. The first two sections describe the formulation of the model and the equations used. The third section will discuss the results of the simulations.

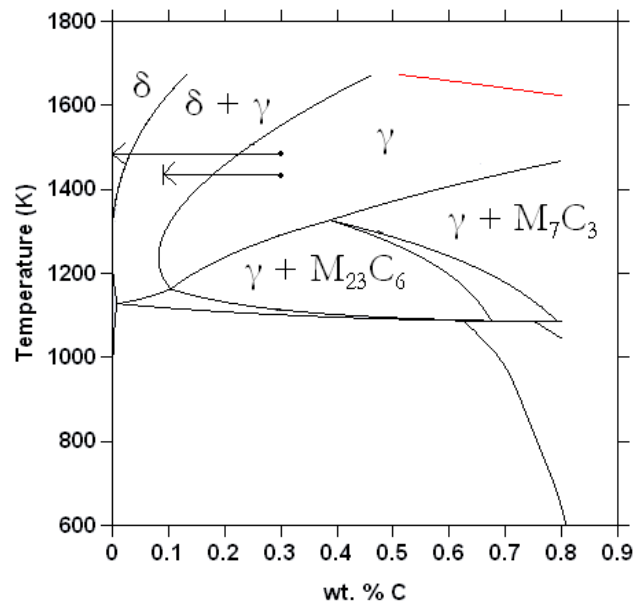
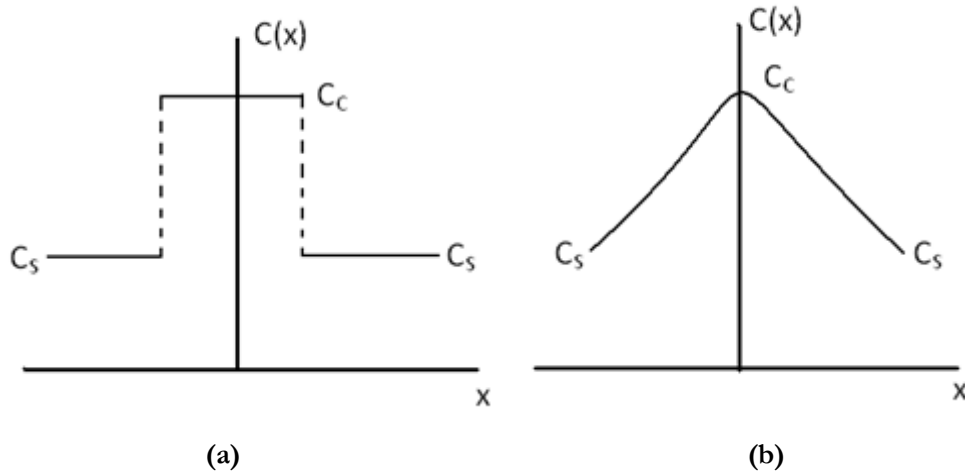


Figure 5.2- Phase diagram of the balance Fe-12.33%Cr-C system

Using the phase diagram in Figure 5.2, which was created using ThermoCalc,

it can be seen that two main resulting microstructural profiles will be apparent. The first profile is a layer of ferrite at the surface of the steel, which does not transform upon quenching and the core is austenitic which transforms to martensite upon quenching. This can be achieved by decarburizing a relatively low carbon content bulk material to 0%C, which is in the ferrite region. This results in a ferrite surface and martensitic core. The second is a smooth transition of phases from the core to the surface of the material. This can be obtained by decarburizing a higher bulk carbon content sample to intermediate carbon contents at a high temperature. This places the material, depending on the starting carbon content in one of two regions, ferrite and austenite or just pure austenite. Upon quenching the amount of ferrite in the material will decrease from the surface to the centre and the amount of martensite will gradually increase until it is all martensite. This results in a continuous microstructure with no sudden change from ferrite to martensite.

This model will explore 2 possibilities. The first is that the carbon content exhibits a so-called sharp interface. This means that the carbon distribution function is discontinuous at the point where the carbon content changes from one value to another. This is demonstrated in Figure 5.3 (a) on the next page.



(a) Sharp interface profile and (b) is an example of a continuous interface profile

The second possibility this model considers is that the carbon distribution profile is a continuous profile as a function of x . This means the profile can follow a linear profile, sinusoidal, an error function etc. This is a much more difficult problem to model than the sharp interface because the material properties are constantly changing depending on the portion of the sample of interest. It would look like Figure 5.3 (b) above.

5.5.1 Sharp Interface

In a composite material there are three possibilities for the deformation paths a material can exhibit [4]. In this graded material the increase in mechanical properties is due to a soft, ductile layer of ferrite on the surface and a hard, brittle martensitic core. Therefore, the three possibilities of deformation are:

1. The surface and the core have not yielded
2. The surface has yielded and is plastically deforming, while the core has not yielded and is elastically deforming
3. Both the surface and the core have yielded and are now plastically deforming

In the sharp interface profile, it is very easy to treat all three deformation regimes but the third possibility is the most important as it allows the material to take advantage of the elastic-plastic transition and begin to work harden. It is in this regime that the stress, strain and energy absorbed by the material will be the greatest and for this reason this model will only consider regime 3.

To treat this problem, the rule of averages for composites [33] can be used to write the equation for stress as a function of strain. Since only two different carbon contents are being used in the sharp interface model, the core and the surface material will have different yield stresses and work hardening rates. They will have the same Young's moduli as they are the same material essentially. Equation 5.1, below, for stress is as follows:

$$\sigma_3(\varepsilon) = (1 - V_m) \left(E \varepsilon_{y,s} + \frac{d\sigma_s}{d\varepsilon} (\varepsilon - \varepsilon_{y,s}) \right) + V_m \left(E \varepsilon_{y,c} + \frac{d\sigma_c}{d\varepsilon} (\varepsilon - \varepsilon_{y,c}) \right) \quad (5.1)$$

Where V_m is the volume fraction of martensite in the material, E is the Young's Modulus, ε is the strain in the material and ε_y is the yield strain of the core/surface of the material and $d\sigma/d\varepsilon$ is the work hardening rate of the material

The volume fraction of martensite can easily be converted to the width of the ferrite layer by:

$$W_f = \frac{t_{sample}(1 - V_m)}{2} \quad (5.2)$$

where t_{sample} is the thickness of the sample.

The values used for the above materials properties used are listed in Table 5.1.

Table 5.1- List of values for constants used in the sharp interface profile

Constants	Values
$\sigma_{y,s}$	150 MPa
$\sigma_{y,c}$	1000 MPa
$d\sigma_s/d\varepsilon$	200 MPa
$d\sigma_c/d\varepsilon$	1100 MPa
$\varepsilon_{y,s}$	0.000714
$\varepsilon_{y,c}$	0.004762
Surface Crack Length	0.0001 m
Internal Crack Length	0.000005 m

With the stress in the material as a function of strain, the next logical question to ask is when this material will become unstable (i.e. neck or fracture). To handle the question of necking, Considere's criterion is used to determine the strain at which necking occurs. This value obtained from Considere's criterion can then be used to find the necking stress. Considere's criterion for this model is given below:

$$\sigma_3 = \frac{d\sigma_3}{d\varepsilon} \quad (5.3)$$

Using Equation.'s 5.1 and 5.3 yields 5.4 for the critical strain at which necking occurs:

$$\varepsilon_c = \frac{(1 - V_m) \left(\frac{d\sigma_s}{d\varepsilon} - \sigma_{y,s} + \frac{d\sigma_s}{d\varepsilon} \varepsilon_{y,s} \right) + V_m \left(\frac{d\sigma_c}{d\varepsilon} - \sigma_{y,c} + \frac{d\sigma_c}{d\varepsilon} \varepsilon_{y,c} \right)}{(1 - V_m) \frac{d\sigma_s}{d\varepsilon} + V_m \frac{d\sigma_c}{d\varepsilon}} \quad (5.4)$$

which can be back substituted into Eqn. 1 to yield the stress in the material at

necking, represented mathematically as:

$$\sigma_c = \sigma_3(\epsilon_c) \quad (5.5)$$

The next issue to address is the failure of the material by fracture. Using the knowledge that grades of steel similar to the one addressed in this model develop micro cracks on their surface when quenched and that materials have internal cracks, the fracture stress can be calculated.

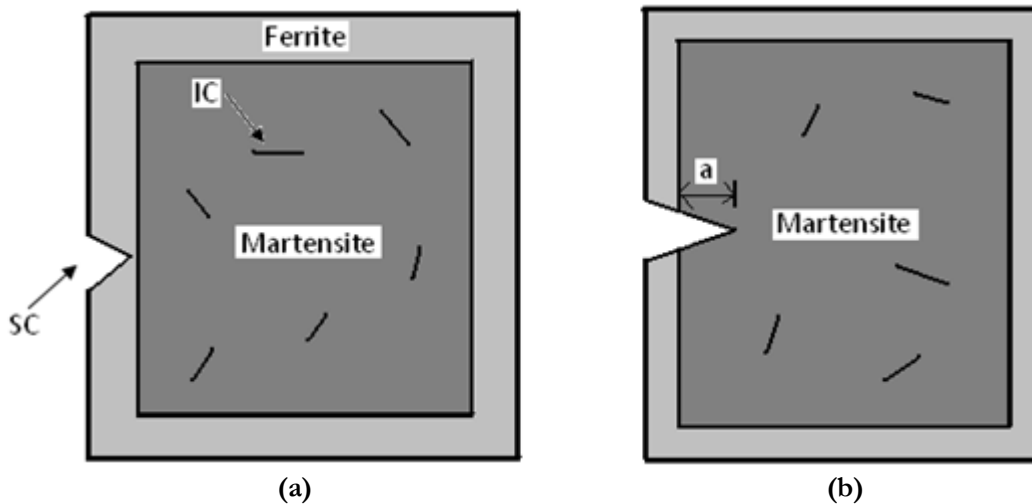


Figure 5.4- (a) Surface crack completely contained within a ductile ferrite layer, (b) Surface crack extending through ferrite layer and into the brittle martensitic core

Figures 5.4 (a) and (b) above can be used to visualize how fracture due to micro cracks was handled in this model. If there is a surface crack in the material and the ferrite layer is thick enough, as in Figure 5.4 (a), to contain the surface cracks than the internal cracks become the operating crack length that is used to calculate the fracture stress. Here it is assumed that the ferrite phase is so ductile that a surface crack will not cause the ferrite to fracture and that the fracture would occur

in the martensite or the material would reach the critical strain given by Considere's criterion and fail due to necking. If the situation is as can be seen in (b) in Figure 5.4, than the crack length is potentially different than the internal crack length. Here, the surface crack penetrates into the martensite which is much more brittle. A new effective crack size may result because of this and this crack length must be calculated.

$$a_{eff} = a_{sc} - W_f \quad (5.6)$$

Where a_{eff} is the effective crack size, a_{sc} is the length of the surface crack, a_{ic} is the length of the internal crack, and W_f is the width of the ferrite layer. If a_{eff} is greater than the length of the internal crack then a_{eff} becomes the crack length used to calculate the fracture stress. Otherwise it is the largest crack length found in the martensite. From elementary mechanics, the fracture stress in a material is given by:

$$\sigma_f = \frac{K_{IC}}{\sqrt{\pi a_{eff}}} \quad (5.7)$$

where K_{IC} is the fracture toughness of the material in $\text{MPa}\cdot\text{m}^{1/2}$. For martensite it is a value of $10 \text{ MPa}\cdot\text{m}^{1/2}$ as taken from [33]. Crack propagation should not have to be taken into account in this model because it is more important in stress cycling than in just pure tension. This allows a major simplification of the fracture mechanics in the model. Using values taken from literature [references?], the fracture toughness of martensite as a function of the Ultimate Tensile Strength (UTS) can be calculated by

the following empirical relationship:

$$K_{IC} = 3022.1 - 392.04 \cdot \ln(UTS) \quad (5.8)$$

There can be two outcomes when the stress in the material reaches the fracture stress:

- 1) The martensite fractures after it has yielded and
- 2) The fracture stress in the material is so low due to a large crack size that it fractures before the martensite has yielded.

Using these two possibilities, the critical strain which fracture occurs can be calculated. The strains will be calculated only for martensite as it is assumed that ferrite will always fail due to necking before its fracture stress is reached. Using case 1 yields a fracture strain, ϵ_f :

$$\epsilon_f = \frac{\sigma_f - \sigma_{y,c}}{\frac{d\sigma}{d\epsilon}} + \epsilon_{y,c} \quad (5.9)$$

And case 2, the simple case is:

$$\epsilon_f = \frac{\sigma_f}{E} \quad (5.10)$$

However this problem is still not finished. The mode of fracture must be determined. As mentioned previously, the material will fail by strain induced necking or stress induced fracture. Which comes first depends on the amount of martensite

in the material. To determine this, the two different instability strains were compared and the smallest strain is the mode that determines failure. If the calculated necking strain is smaller than the calculated fracture strain then failure occurs by necking, for example. When the mode of failure is determined and the strain it occurs, the stress at fracture can then be determined using Equation 5.5. The results of this model are plotted and examined in the 5.4.3.

Another property of the material that is of interest is absorbed energy. Absorbed energy is useful to know in applications that involve high deformations of the materials used in the application, such as automobiles that are involved in car accidents. Engineers would find it useful to determine the composition of a material that maximizes the absorbed energy in a material, while achieving a given strain, all while keeping the fracture stress in the material as low as possible. In the auto industry, having the material deform as little as possible while maximizing absorbed energy and not inducing fracture is the ultimate goal.

In the sharp interface model, the energy absorbed by a material to fracture can be calculated in a straightforward manner by integrating Equation 5.3 from a strain of zero:

$$U = \int_0^{\varepsilon_c} \sigma_3(\varepsilon) d\varepsilon \quad (5.10)$$

Because the material is in regime 3 and stress can be written as a simple

function of ϵ , the calculation is negligible using a spreadsheet. The resulting equation is not shown as it is quite large. The energy absorbed by a material at a given strain, ϵ^* can also be calculated by integrating Eqn. 3. However the limits of the integral (value of strain) are whatever is desired by the engineer:

$$U = \int_0^{\epsilon^*} \sigma_3(\epsilon) d\epsilon \quad (5.11)$$

The major difference between in implementation between Eqns. 5.10 and 5.11 is that when calculating the absorbed energy at fracture, the failure criterion is necessarily reached, while using a prescribed strain the failure criteria might be reached or it might not. The logical functions (IF, AND, OR) in Excel make it easy to maximize the absorbed energy for a given martensite volume fraction while adhering to boundaries of fracture stress and necking strain given by the problem. The results of the absorbed energy calculations are shown and discussed in section 5.5.3.

The sharp interface model does yield results that allow one to see what carbon profile gives the maximum stress, strain and absorbed energy for the material. It is a very easy situation to model, however it is not a very realistic carbon distribution. The next phase of the model is to introduce a carbon distribution that is attainable in the real world and yields more accurate solutions.

5.5.2 Continuous Profile

The continuous profile is much more complicated than the sharp interface profile. This problem can be tackled in a couple of ways. The first is to analytically or numerically determine a carbon distribution using the calculus of variations. The second is to break the graded material into sections and use a brute force method of calculating the carbon contents, their resulting stress, strains, absorbed energy, etc. and determine the optimal carbon profile that way.

While the first way is much more elegant and will yield the optimal carbon distribution more efficiently, this method is much more difficult mathematically and requires the use of MAPLE or MatLab. With the powerful computers of today, the problem can be cut down into many smaller parts and still solved, while keeping the mathematics of the problem simple. Each of these slices or sections has its own carbon content that is determined by a carbon distribution that can be changed. In this model, a linear carbon profile was initially chosen but this can very easily be changed for a sinusoidal or parabolic carbon distribution. For this reason the brute force method was chosen and used to model a material that has a continuous distribution of carbon. Another goal of this model is to calculate stress-strain curves that can be used to predict the behaviour of the graded materials.

Fundamentally, this model is the exact same as the sharp interface in that the material can undergo one of three deformation modes, as mentioned previously. The difference is that in the continuous profile the yield stress and work hardening

vary with position. This adds a minor complication to the problem in that relations for yield stress and work hardening must be determined as a function of carbon content. Arcelor-Mittal has compiled data from many different grades of low alloy steels and used this data to fit an empirical relationship that describes the stress of low alloy steels as functions of alloying contents and strain. This relationship is shown Equation 5.12.

$$\sigma = f(\varepsilon, \%C, \%Mn, \%Si, \%Cr, \%Mo)$$

$$\sigma = A + 3000 \cdot \%C^{0.78} \left(1 - \exp \left(- \left(179 + \frac{0.000752}{\%C^5} \right) \varepsilon \right) \right) \quad (5.12)$$

$$A = 682 + 33\%Mn + 81\%Si + 58(\%Cr + \%Mo)$$

The advantage of having a relation like this is that it captures the yielding and deformation behaviour of the alloys. By using the model to vary the carbon content, the behaviour of a graded material can be captured.

The yield stress as a function of carbon content can be determined from this equation by using the offset method of calculating the yield stress of a material. An offset of 0.1% strain will be used to calculate the yield stress of the material for each of the different “slices” that have different carbon contents. Plugging in 0.001 into Equation 5.12 and varying the carbon content will give an approximation of the yield stress. The offset method is shown in Figure 5.5 [41] below.

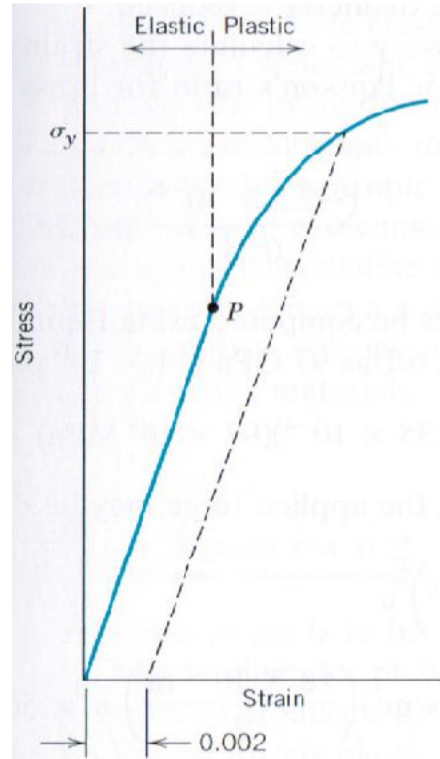


Figure 5.5- Schematic of how the offset method of calculating the yield stress of a material from its stress-strain curve works [41]

Simply plugging in 0.001 will yield the stress at 0.001 strain but not the stress where at which a line drawn through the strain axis at 0.001, running parallel to the curve in its elastic zone intersects the stress strain curve once it has yielded. Therefore it should be noted that this yield stress is not entirely accurate but a rough approximation.

The work hardening rate of this material can also be calculated by differentiating Equation 5.12 with respect to strain., as shown below:

$$\frac{\partial \sigma}{\partial \varepsilon} = 3000 \cdot \%C^{0.78} \cdot \left(179 + \frac{0.000752}{\%C^5}\right) \exp\left(-\left(179 + \frac{0.000752}{\%C^5}\right)\varepsilon\right) \quad (5.13)$$

For materials where an empirical relationship that describes the deformation

behaviour of material is not known, Equations (5.14) and (5.15) would have to be used. These are general equations and can be used for any material. A relation for how the yield stress and the work hardening rate vary with carbon concentration would have to be known if (5.15) is to be used.

$$\sigma = E\varepsilon \quad (5.14)$$

if the section had not yielded and

$$\sigma = \sigma_y + \frac{d\sigma}{d\varepsilon}(\varepsilon - \varepsilon_y) \quad (5.15)$$

if it has yielded.

In this model a carbon distribution is being assumed and the optimal surface concentration and bulk concentration is determined. This distribution is linear. The following formula is used to calculate the concentration of carbon of the section when the section is not in the bulk concentration:

$$C_s + \frac{C_b - C_s}{W_T - W_b} \quad (5.16)$$

Where C_s is the surface concentration, C_b is the bulk concentration, W_T is the thickness of the sample and W_b is the width of the bulk. Of course this linear relationship can be changed to whatever is desired.

The basis for this formulation is to create a ratio of the areas of each individual section to the total area of the sample. Assume each section of material has a thickness of Δd . The total thickness of the sections combined is given by $d = \Delta d \cdot n$, where n is the number of sections. From the geometry in Figure 5.6 (b) it can be observed that in the L direction and W direction that there is a total change of $2 \Delta d$ and that the thickness of the decarburized region is $W - 2 \Delta d \cdot n$ and $L - 2 \Delta d \cdot n$. Using these relations allows a calculation of the areas of the sections in the L and W directions, as well as the total area of the sample:

$$\frac{A_{section}}{A_{Total}} = \frac{2\Delta d(W - 2\Delta d \cdot n) + 2\Delta d(L - 2\Delta d \cdot n)}{WL}$$

There is a problem with the above formula. With this formulation some of the areas are being double counted, as can be seen in Figure 8 b). The area that is being double counted is the area that is common to the sections in the L direction and W direction. 2 of these areas, equal to $2\Delta d^2$, must be subtracted from the area above. This yields:

$$\frac{A_L + A_W}{A_{Total}} = \frac{2\Delta d(W - 2\Delta d \cdot n) + 2\Delta d(L - 2\Delta d \cdot n) - 2(\Delta d)^2}{WL} \quad (5.17)$$

The equation for stress remains the same except the law of averages does not apply in this model because the stress is being calculated for each section of material that is the same composition. In other words the stress calculated is not the bulk stress of the material, just a component of the stress in the material. The average of the

stresses in each section will give the bulk stress in the material

Another difference that arises in the continuous profile from the sharp interface is the calculation of the failure criteria. Fracture in a material is a local phenomenon while necking is a global phenomenon. To determine if the material has fractured the stress in each of the slice of the material is calculated under a given strain. The fracture stress of that slice is also calculated. Equation (5.7) still applies for each slice and the idea of the effective crack length remains the same. When the first section fractures then the material fails.

Necking is quite different than in the sharp interface profile. The first steps are to calculate the stresses and work hardening rates in each of the sections and average those. This becomes the global work hardening rate and stress of the material. The strain at which the global stress is greater than the global work hardening is when the material fails due to necking.

The absorbed energy was also calculated in this model. To calculate the absorbed energy as a function of deformation Equations (5.11) and (5.12) can be used.

$$U = \int_0^{\varepsilon^c} \left(A + 3000 \cdot \%C^{0.78} \left(1 - \exp \left(\left(179 + \frac{0.000752}{\%C^5} \right) \varepsilon \right) \right) \right) d\varepsilon$$

This was also different from the sharp interface model in that there was no continuous stress function that depended on strain to analytically integrate; it had to

be numerically integrated. The trapezoidal rule was picked as the integration for its ease and relative accuracy. The absorbed energy was calculated for each section and then summed together with each of the previous sections to obtain the total absorbed energy in the material up to that strain. The plots for maximum stress, maximum strain and the absorbed energy are discussed in the next section.

5.5.3 Results and Discussion

5.5.3.1 Sharp Interface

The first results presented from the model are for sharp interface profile. As can be seen from Figures 5.7- 5.10, the optimal martensite volume fraction occurs at around 0.9, when necking and fracture are both considered. At 0.9 martensite volume fraction, the stress and absorbed energy are both maximized, where as the strain is not at the maximum. In fact, the strain at a volume fraction of 0.9 is 60% smaller than if the sample was 100% ferrite. This makes sense because in order to maximize ductility, the amount of ferrite would have to be maximized. Having a maximum stress value with 90% martensite is reasonable because martensite is what gives the material its strength. However, if it were any higher the brittleness of the phase would not be able to accommodate the high stress in the material induced from the surface or internal cracks present in the material. If the % martensite were any lower, the amount of ferrite in the material would decrease its strength but increase its ductility.

Maximizing the strain a material can handle requires using as much of the

most ductile phase as possible. In this case ferrite is the most ductile, so having a material that is all ferrite would maximize this property. This is also confirmed through real world observations

Maximizing absorbed energy in a material requires careful control over the amount of each phase that is present in a material. This means a fine balance between stress and strain accommodation must be found in order to absorb the most energy in material. Figure 5.9 demonstrates that even though the strain at the volume fraction of martensite that maximizes absorbed energy is 60% lower than the material can obtain at its optimal fraction for strain, the material is able to absorb high amounts of stress because of the martensite present.

Figure 5.10 demonstrates how the model can predict the volume fraction of martensite that maximizes the absorbed at a given strain, ensuring that the material does not reach critical stress or strain. As an example, a maximum strain of 15% is desired for a given application. Figure 5.10 predicts that at a 24% volume fraction of martensite, the absorbed energy in the material is around 58 MJ/m³. Anything beyond this strain and the material will fail. These charts can provide very useful insight into the trends of the properties of a material and allow engineers to pick a material with the optimal properties desired for a specific application.

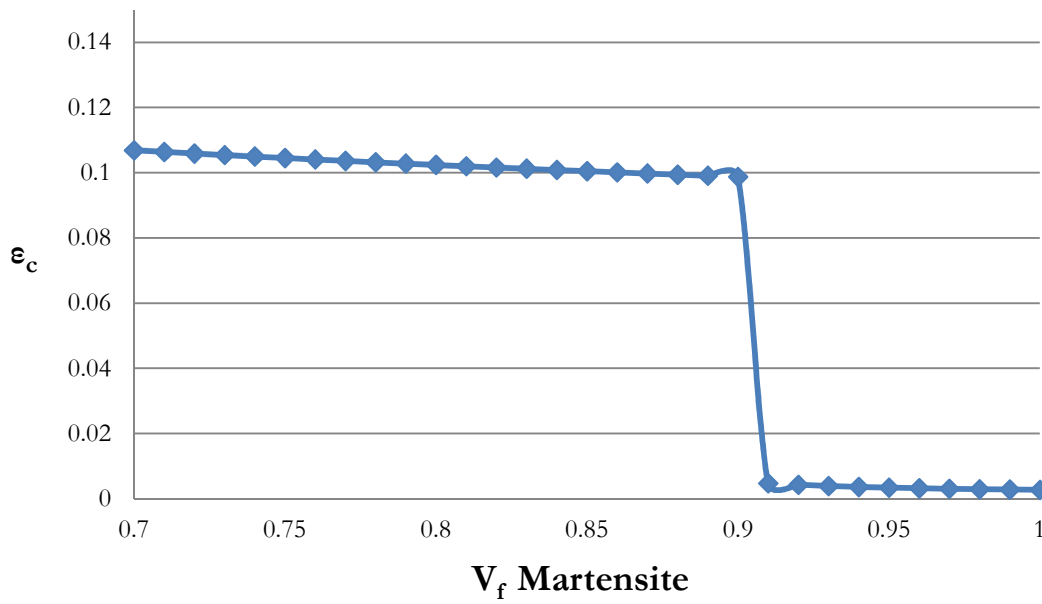


Figure 5.7- Failure strain as a function of volume fraction of martensite for a sharp interface

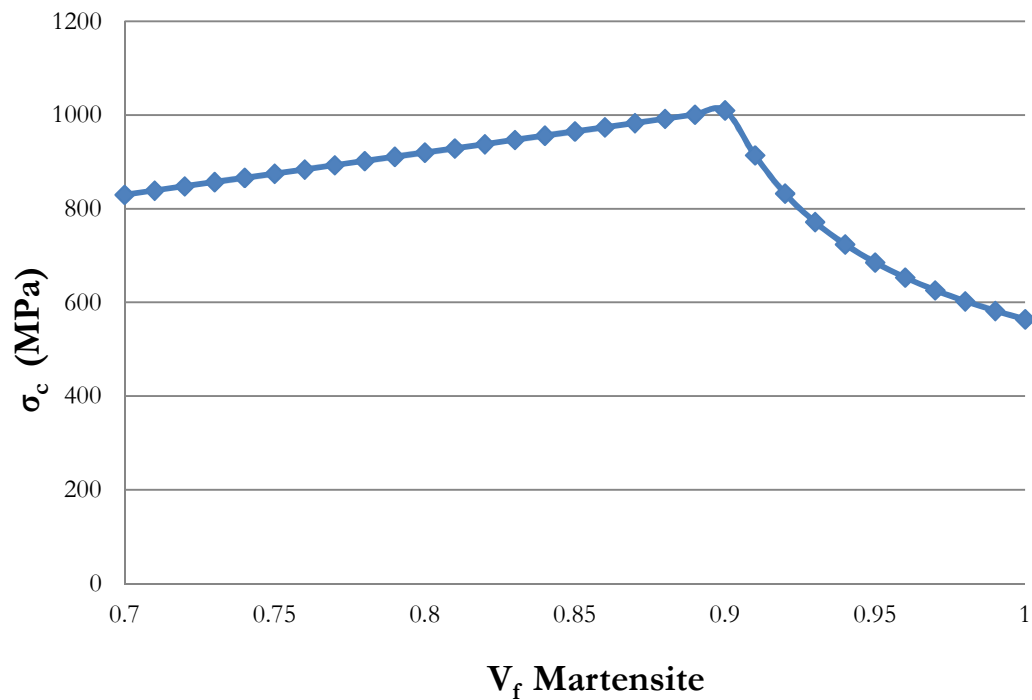


Figure 5.8- Failure stress as a function of volume fraction of martensite, assuming a sharp interface profile.

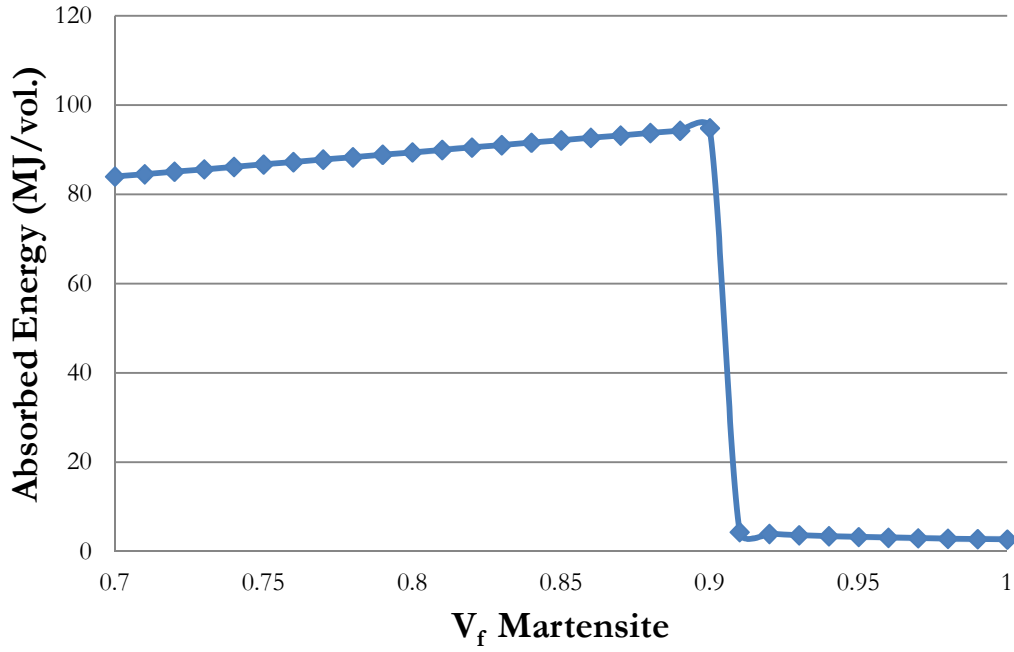


Figure 5.9- Absorbed Energy at critical strain as a function of volume fraction of martensite

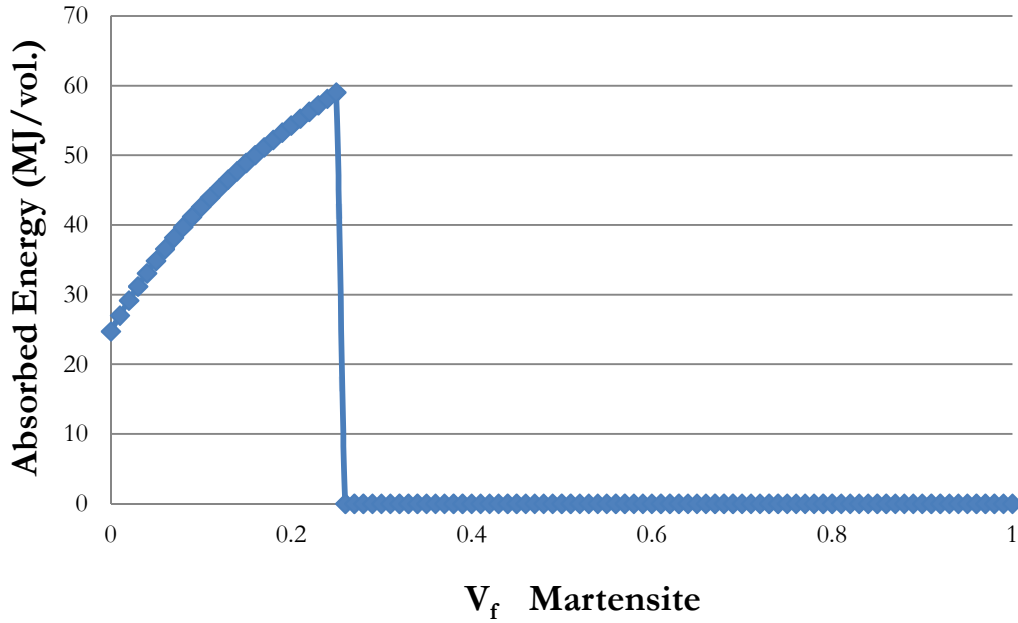


Figure 5.10- Absorbed energy at prescribed strain as a function of volume fraction of martensite

Continuous Profile

Three different situations will be tested to determine if the model with a continuous profile provide reasonable results. The first situation to be tested was to maintain a constant bulk carbon concentration, along with a decarburization layer equal to 1/3 the thickness of the sample. The carbon content at the surface of the sample was then changed from 0 wt.%C to 0.4 wt.%C with a bulk content of 0.4 wt.%C. The second simulation run was to set the core to 0.13%C and the surface to 0 wt.%C. The decarburization depth was then changed to determine which level of decarburization offers the best properties. The third simulation ran had a constant surface concentration of zero at the surface and a constant decarburization depth but with a changing bulk carbon concentration that ranged from 0.4 to 0.1%C. These simulations are represented graphically in the Figures 5.11 (a), (b) and (c).

It is important to remember that the absolute values are not what are important when analyzing the results from this model, or many models in fact. It is the trends that they predict that are the most important. These situations tested did not use the relationship for stress provided by Arcelor. They used data from [33] and [34] that was thought to provide reasonable values of K_{IC} , YS and work hardening for martensitic steels. The empirical relationship will be used to compare this model against experimental results.

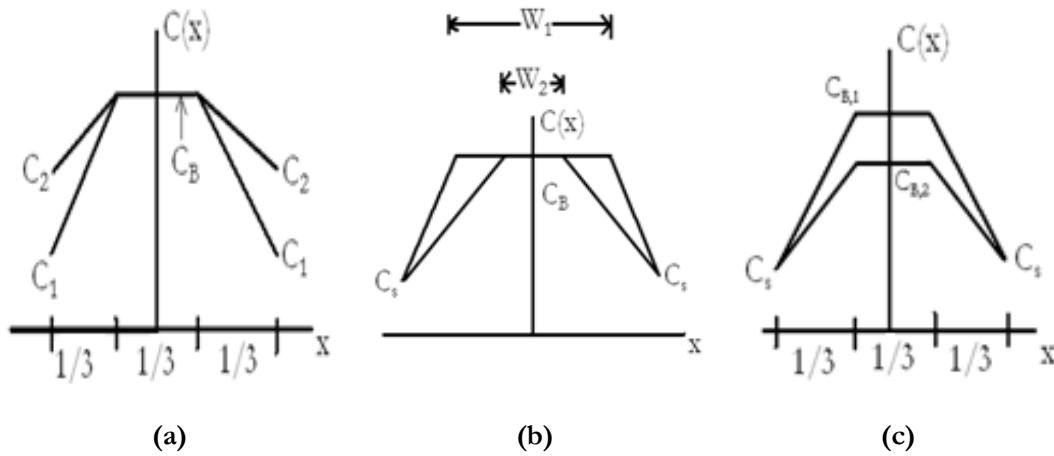


Figure 5.11- Carbon distributions of the different simulations run for a continuous profile

5.5.3.2 Continuous Interface

Constant Bulk Carbon Concentration, Varying Surface Concentraion

The first situation presented is for a constant bulk concentration of 0.4%C and varying surface carbon concentration. The result for the fracture strain as a function of surface concentration is given in Figure 5.12. When looking at the fracture strain as a function of C_s , it is intuitive that the lowest concentration of carbon at the surface should offer the greatest ductility. This is what the model shows. It should also be intuitive that above a certain C_s , decarburization does not improve ductility and the material begins to behave as if it were no decarburized. From the plot in Figure 14 it can be seen that around a C_s of 0.2% is where the ductility is significantly reduced if the initial concentration is increased significantly. Without viewing any other graphs or data related to the simulation, one can conclude that this is the transition point that the material moves from one with some ductility to one that is very brittle.

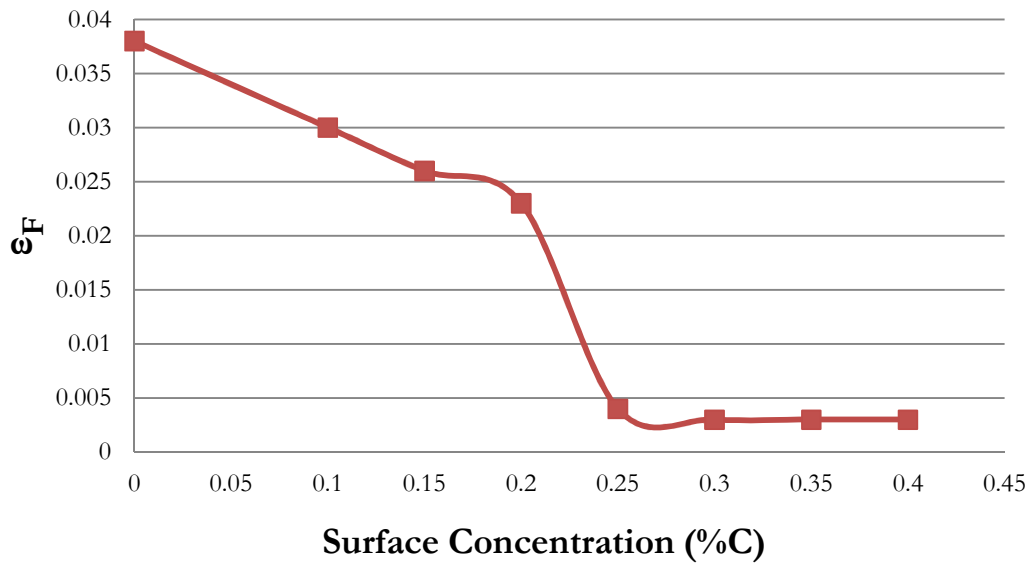


Figure 5.12- Fracture strain as a function of surface concentration for a continuous carbon distribution

When examining Figure 5.13, it can readily be seen that at a carbon content of 0.2% on the surface is optimal for maximizing stress. This can be explained physically very easily. With C_s of less than 0.2%, the decarburized layer has a lower yield stress and work hardening rate and cannot accommodate as high as stress. Above 0.2% the material has too high a K_{IC} . This makes it more susceptible to fracture from surface cracks or internal cracks, especially at such a high carbon content as 0.4%C. When the material is loaded, it reaches the fracture stress at small strains and fails.

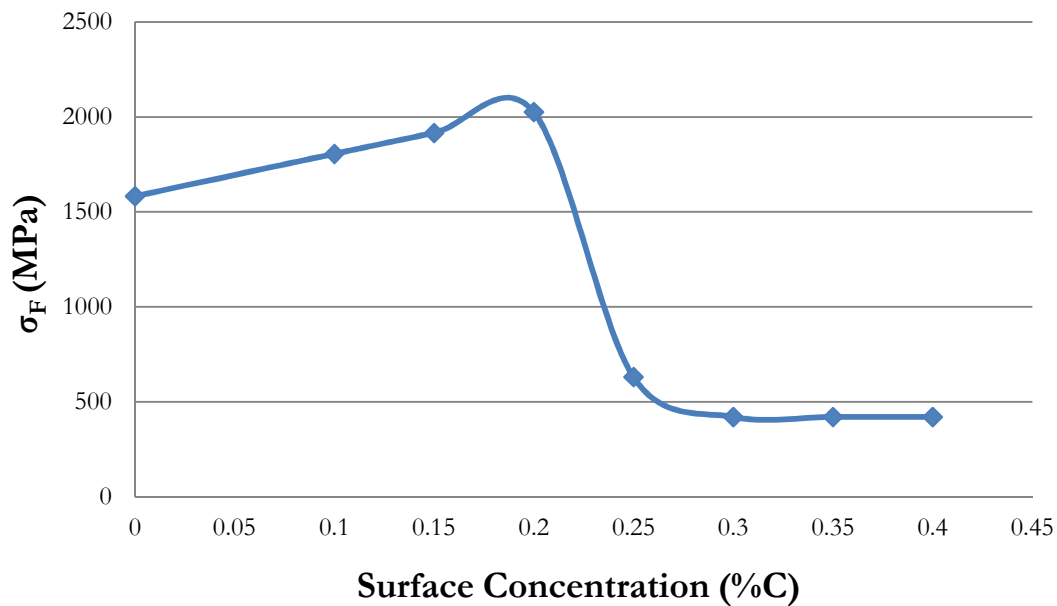


Figure 5.13- Fracture stress as a function of fracture strain

Absorbed energy follows the same basic pattern as the fracture strain, as seen in Figure 5.14. With absorbed energy there is always a tradeoff between brittleness and ductility. In this case, it is better to have a more ductile material to get the most plastic deformation to absorb the most energy. But again, 0.2%C is the transition between high energy absorption and a very quick deterioration to a low energy absorption.

To finally conclude that 0.2%C as the surface concentration is the best concentration to use, the fracture stress was plotted against the fracture strain in Figure 17. 0.2%C has the fracture highest stress at its strain. While its fracture strain is 20% lower than the C_s of 0%, it can accommodate much higher stress and has better work hardening characteristic. A decision would have to be made that is tailored to the application- is ductility or strength more highly prized?

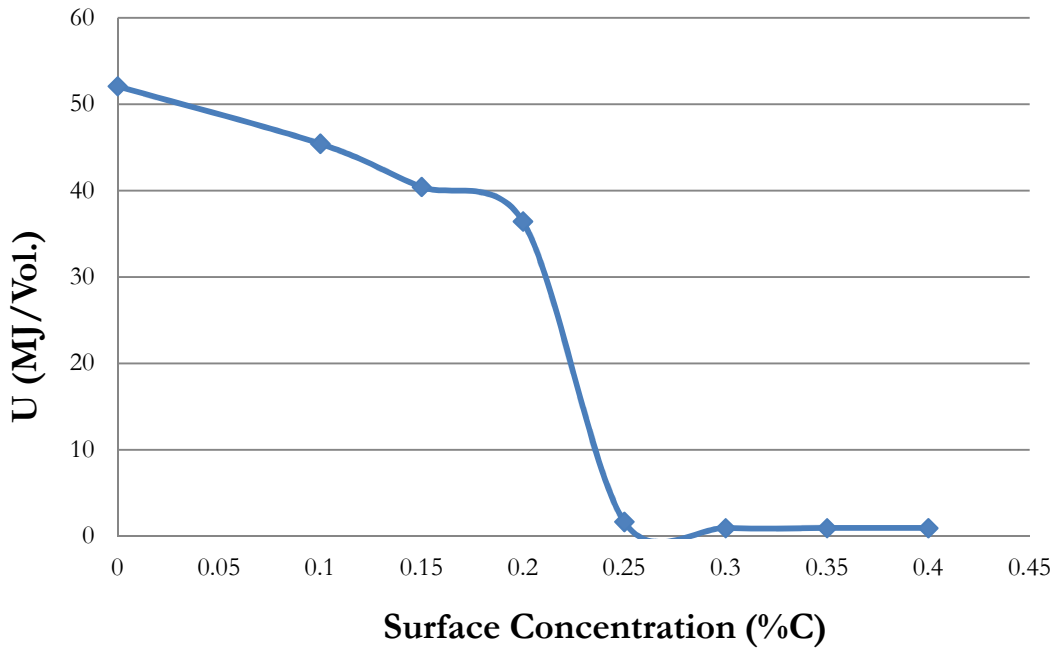


Figure 5.14- Absorbed energy as a function of surface concentration for a continuous profile

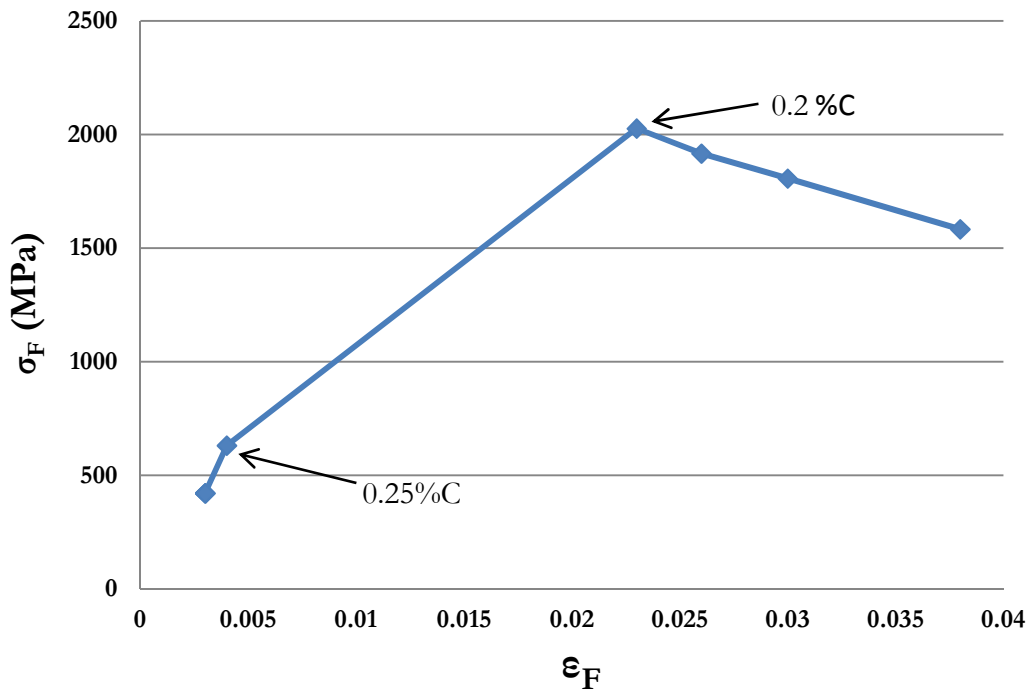


Figure 5.15- Fracture stress vs. fracture strain for the different surface concentrations modeled

Figures 5.16 and 5.17 is the carbon distribution and stress-strain curve for $C_s=0.2\%C$, respectively. The stress strain curve is of particular interest. Notice in Figure 5.17 at the yield stress, the shape of the curve changes abruptly and follows the work hardening rate, which is very flat. A smoother transition from the elastic region to plastic regime is expected. This could, potentially, be due to the internal stress that forms when the material undergoes the martensitic transformation. More data about the work hardening of martensitic steels would be required to achieve a work hardening rate that is more realistic.

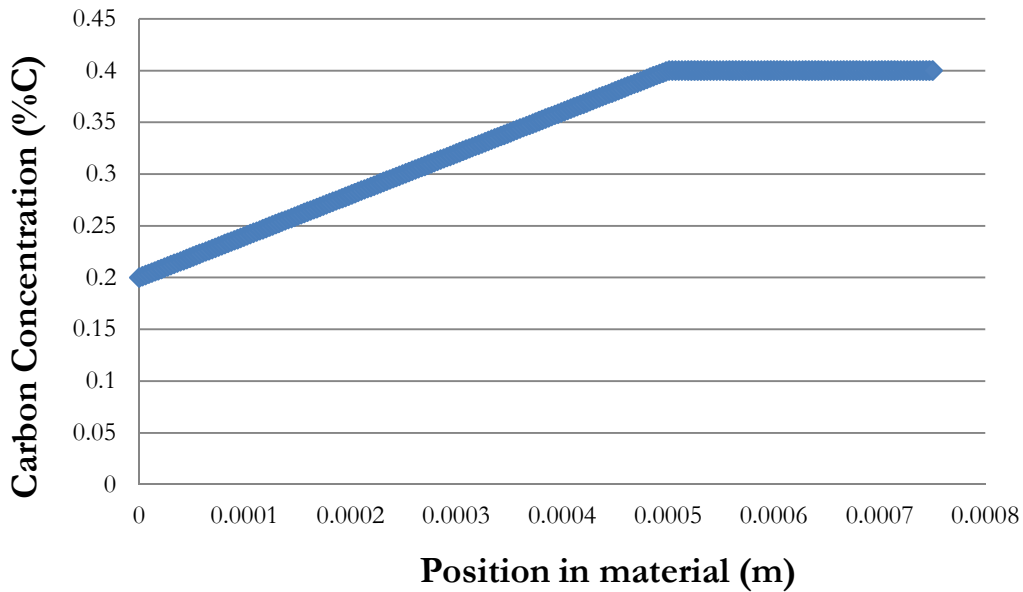


Figure 5.16- Carbon distribution profile for $C_s = 0.2\%C$

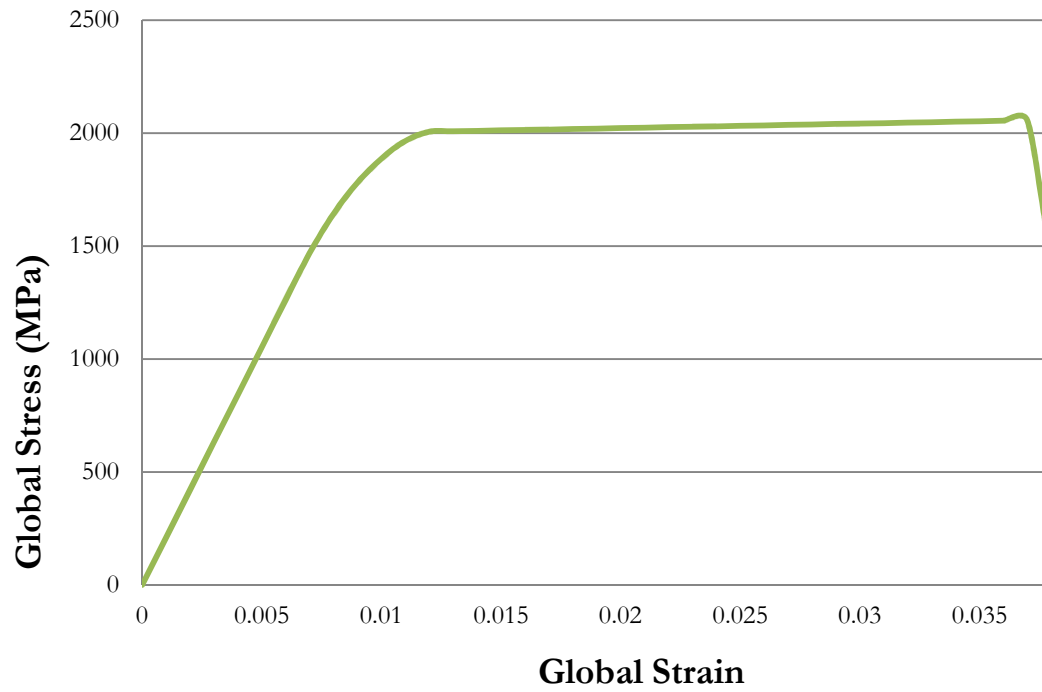


Figure 5.17- Global stress vs. strain for the optimum carbon content

Constant Bulk and Surface Concentration, Varying Decarburization Depth

The results for this simulation, represented by Figure 5.11 (b), can be found in Figures 5.18, 5.19 and 5.20. The results of this simulation were a little surprising. There is no distinct maximum for the stress, strain and absorbed energy. But the trends shown in the figures make sense. To maximize the stress a decarburization width should be minimized- or zero. To maximize the strain, the decarburization layer should be maximized- or the entire width of the sample. The absorbed energy follows the same trend as the strain but shows more variation than in the stress or strain trends. The curves in the stress and strain vs. decarburization depth follow a smooth, exponential-like curve whereas the absorbed energy does not follow the same curve and shows some deviation from the same curve.

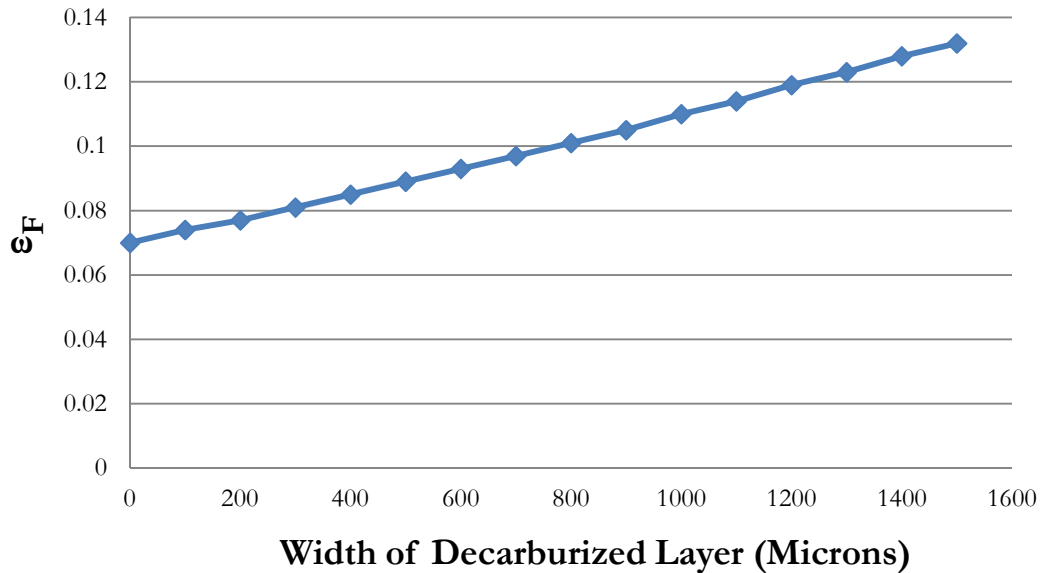


Figure 5.18- Fracture strain as a function of decarburization of width

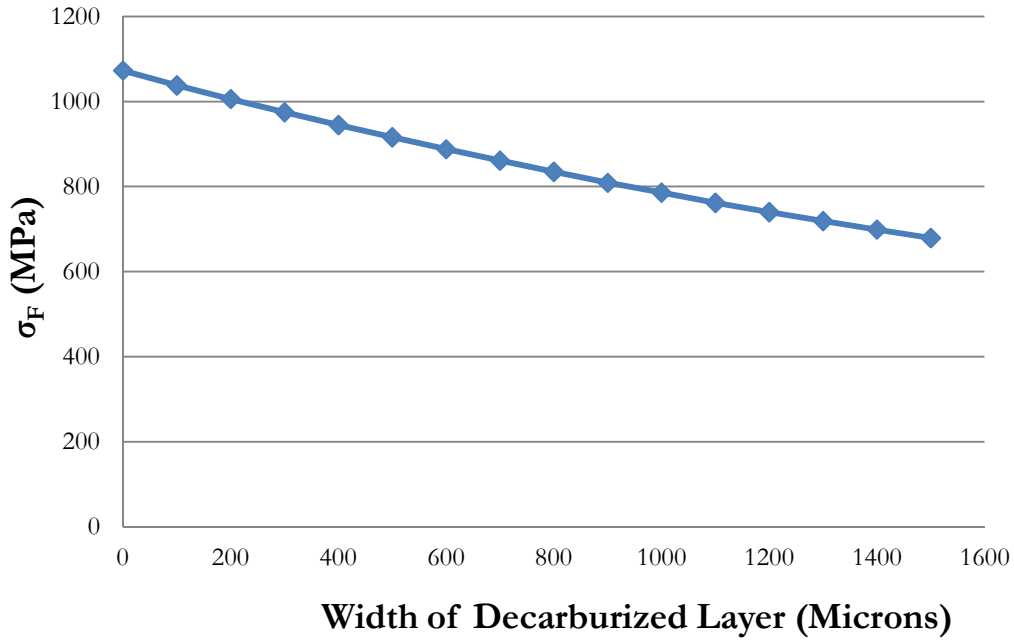


Figure 5.19- Fracture stress as a function of decarburization width

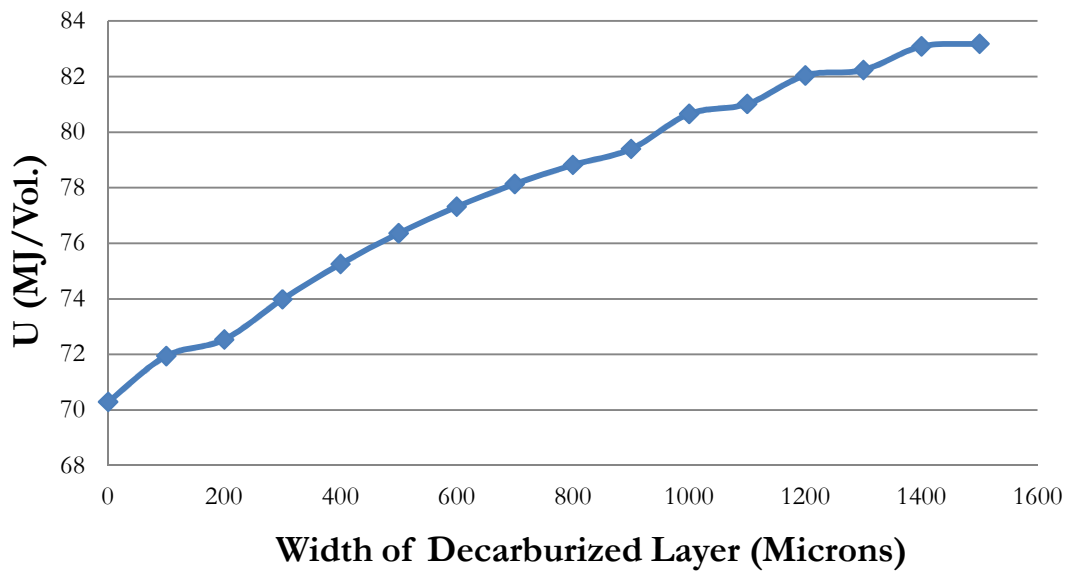


Figure 5.20- Absorbed energy as a function of decarburization width

Constant Surface Concentration and Decarburization Depth, Varying Bulk Concentrations

The results for this simulation are shown in Figures 5.21 to 5.23. Again they show the same trends as the previous situation presented. Decreasing the bulk carbon content increases the maximum strain and energy absorption. However the stress in the material did reach a maximum at around 0.3%C. This is due to the fact that at this carbon content the material still retains enough ductility that it can accommodate the stress caused in the material from either surface cracks or internal cracks. However, the maximum stress is only at 1288MPa when the bulk is at 0.3%C. When this is compared to the 0.4%C bulk concentration with a surface concentration 0.2%C it is much lower than the 2026 MPa stress that this sample attained. This due to the fact that with such a low carbon content at the surface in the $C_B=0.3\%C$, $C_S=0\%C$ material, the work hardening in this material is not very good and it cannot achieve a very high stress as the other material can. This is confirmed within the model that this material fails by necking and not fast fracture from the internal or surface cracks present in the material.

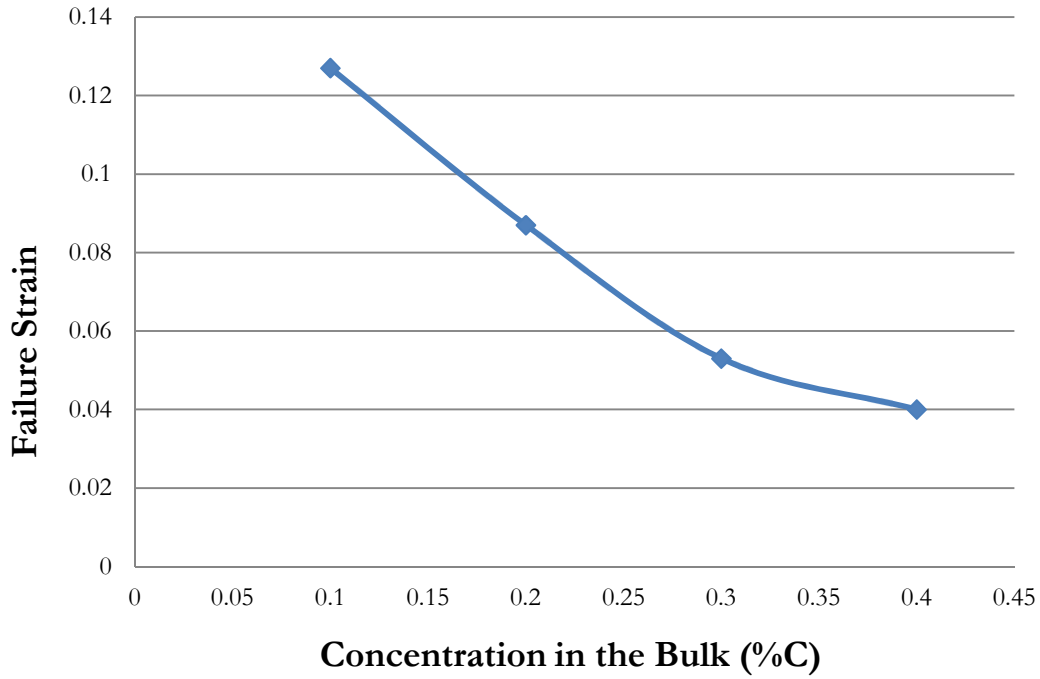


Figure 5.21- Failure strain as a function of the bulk carbon content

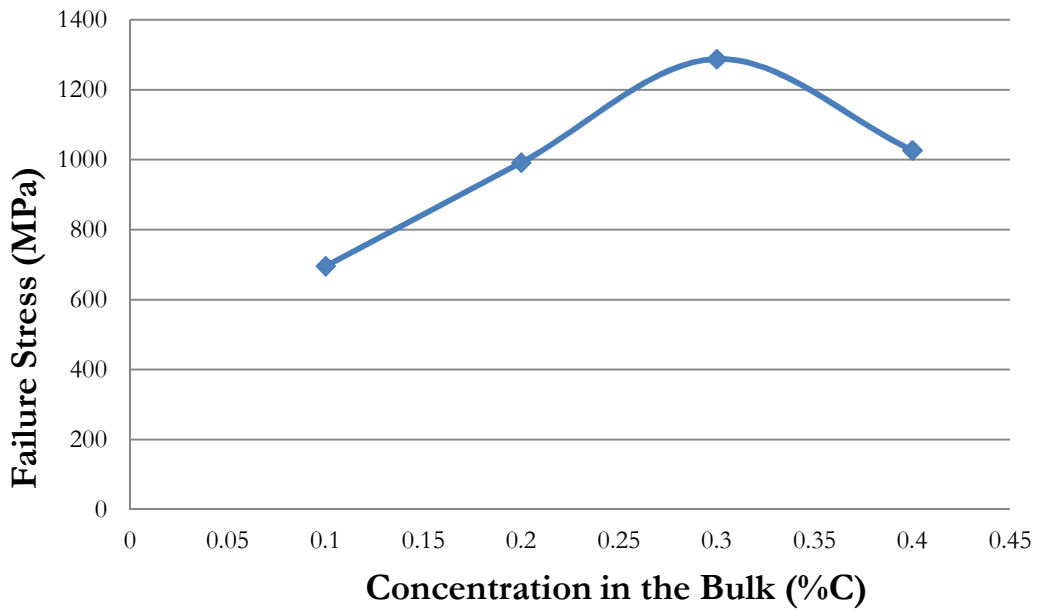
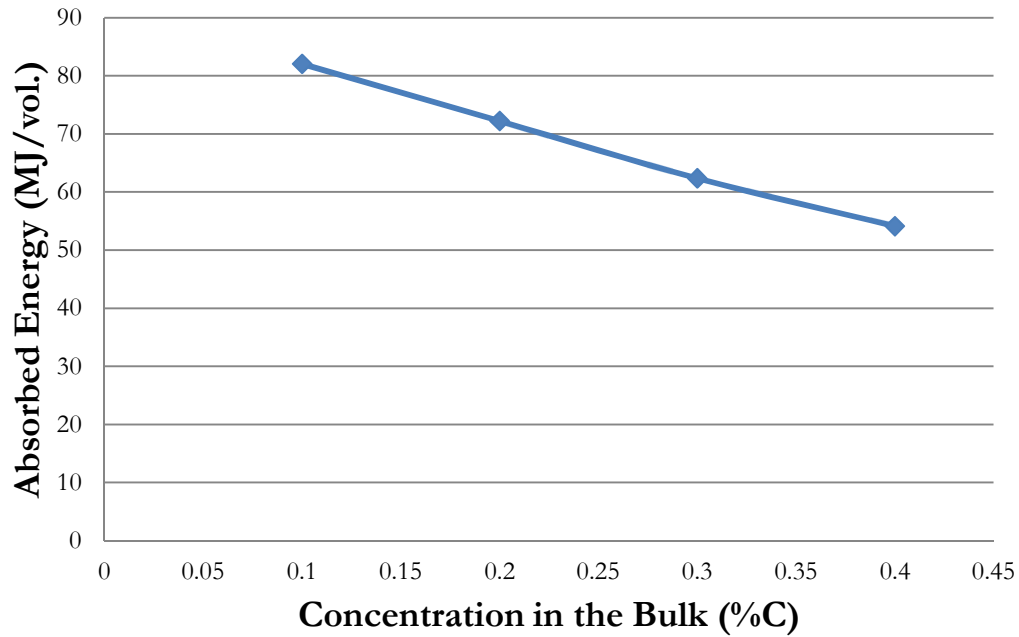


Figure 5.22- Failure stress as a function of the bulk carbon content



5.23- Absorbed energy as a function of the bulk carbon concentration

The results of the sharp interface profile reveal that the optimal carbon content is 0.9% to maximize almost all the properties of the material.

From the results of the continuous profile simulations it can readily be seen that material with a bulk concentration of 0.4%C and surface concentration of 0.2%C provides the best combination of strength ductility and energy absorption due to its higher work hardening rate in the core and the surfaces ability to absorb the stress increase in the material due to cracks. The desired material will always depend on the desired properties for any application. Using the plots provided by the sharp profile and continuous profile, the desired composition can be determined and the proper material can be created for the application.

This model can also be used to compare different quenching media. Oil

quenching samples should lead to larger surface and internal cracks than air quenching. So by adjusting the internal and surface crack sizes different quenching media can be simulated.

After determining the best profiles for 3 situations one can conclude that using the traditional methods of variational calculus would have provided the solution in a much more straightforward manner. Using the brute force method many different situations must be tested and compared to one another to determine which profile yields the best properties. Variational calculus yields a profile directly as a solution to a partial differential equation but the solution of this equation is most likely very difficult and time consuming. The brute force method allows a solution to this problem quickly but it is not very efficient. Both methods have their pros and cons but should yield similar results.

Chapter 6

Conclusions and Future Work

6.1 Conclusions

Based on the experimental and modeling results, the following conclusions and observations can be made:

1. Decarburization of stainless steel is indeed possible through a gas reaction at high temperature. It was initially thought that decarburization would be hindered because of the protective chromia layer that forms on the surface of the material. Decarburization experiments were performed on three grades of martensitic stainless steel. Microhardness measurements and GDOES were used to determine if decarburization did in fact occur. The result for both methods of analysis led to the conclusion that decarburization does in fact occur in all grades for decarburization times as short as 5 minutes.

2. Mechanical testing carried out on homogeneous and graded samples was used to determine whether decarburization has a positive impact on the mechanical properties of the grades that were under study. The results from these tests show that decarburization has a very positive effect on the results during plane strain rolling and Charpy impact tests. The graded samples also performed better during tensile tests when the samples were oil quenched. When the samples were air quenched, decarburization did not offer any advantages during tensile deformation in the MA1 grade. The tensile curves were identical between the homogeneous and graded samples. With these materials, the temperature and time of heat treatment seems to be the most important factor that determines the resulting properties. In the MA3 and MA4 grades decarburization did offer offer improvement in tensile properties.
3. Quenching rate is also very important. During this study, it was found that oil quenched samples performed very poorly compared to air quenched samples. It is thought that small micro cracks form on the surface of samples when oil is used as a quenching medium. These cracks are very detrimental to the mechanical properties. The fast quenching rate of oil also produces a more brittle martensite which decreases ductility of the material. Again, this conclusion leads to the realization that for these grades of martensitic steels, processing plays a more critical role in determining the resulting properties when compared to other steels.
4. A model was created that attempted to capture the behaviour of a graded

material. Specific data with relation to mechanical response was not available for the grades studied here but data on low alloy steel was available so the model was tested against results from work produced by Brick Kung.

6.2 Future Work

There is still much work that can be done on this topic as FGMs are a class of materials that have not sufficiently been explored to date.

The corrosion resistance of functionally graded martensitic stainless steels can be tested and compared to the response of homogeneous martensitic stainless steel to see if there is indeed an improvement in corrosion resistance. Attempts to create samples were tried but due to size constraints, proper dimensions required were unable to be achieved. Attempts in the future could focus on this aspect.

Work on creating functionally graded nanomaterials through deformation and recrystallization can also be carried out. The tensile properties of deformed material and deformed and recrystallized materials were also investigated but the results were unreliable due to sample preparation. A different method of sample preparation could be used to obtain reliable results. This method involves taking a sheet of material, decarburizing it to a desired amount, deforming it to 100% and machining a sample for tensile testing. Deformation and recrystallization has been used to obtain materials of very high strength and ductility. It is hoped this method can be used with martensitic steels to achieve the same effect. TEM can be used to characterize the microstructure and grain size of these materials to determine how they affect the mechanical properties. Results from other experiments performed by the author of this work have shown what the optimum temperature and time for recrystallization is.

Another area that can be explored is the possibility of the creation of a TRIP steel. By increasing the carbon content of the material, the martensitic start and finish temperatures can be lowered. Theoretically this should increase the amount of retained austenite after quenching. This retained austenite would then transform in martensite, increasing the strength of the material. However, the carbon content at which the amount of retained austenite in the material becomes significant may be prohibitively high and result in poor mechanical properties due to the brittleness of the resulting martensite.

Further modeling can also be performed that investigates the effect of gradual yielding and how the different layers of the graded material affects crack propagation. This would include an aspect that accounts for the internal stresses that the material develops when the material transforms to martensite. This can be accomplished by introducing a statistical probability that would determine if individual grains are in tension or compression. With this included in the model, the elasto-plastic transition can be captured better and a more accurate representation of the actual tensile curves can be captured.

Another interesting avenue to look into is to turn this model into one that captures a functionally graded material in plane strain. Experimentally this material has shown a much better ability to deform under plane strain conditions. This condition is the condition that is found during rolling. It is still not clearly understood why this graded material exhibits an excellent ability to accommodate deformation during rolling when compared to material that is not graded. It can also

help unveil why the material deforms well in rolling but its properties in tension are not very good and why there is such a small improvement in properties when the material is in tension as compared to compression in a graded sample.

One thing that this model lacks is the ability to predict carbon distribution for different decarburization times. This can be added with relative ease through the use of a diffusion equation. The tricky part lies in determining the diffusion coefficient. Models exist that calculate the diffusion coefficient of carbon in austenite or ferrite as a function of carbon. But in this material there is a gradual transition from austenite to ferrite at high temperature, so a method that could properly calculate the diffusion coefficient in such a microstructure would have to be determined.

Bibliography

- [1] I. El-Mahallawi, R. Abdel-Karim, and A. Naguib. Evaluation of effect of chromium on wear performance of high manganese steel. *Materials Science and Technology*, Volume 17, Number 11, November 2001 , pp. 1385-1390(6), Print.
- [2] P. Claude. Etude de l'influence des éléments d'alliage Ni, Nb et Mo sur les propriétés mécaniques et de résilience de nuances martensitiques et d'une nuance Maraging. *Internal Presentation*. Arcelor-Mittal Research Group, Isbergues, France. 7 July 2010.
- [3] W. Bleck and P.O. Kriangyut. Microalloying of Cold-Formable Multi Phase Steel Grades. *Materials Science Forum* 500-501 (2005): 97-114. Print.
- [4] B. Chehab, H. Zurob, D. Embury, O. Bouaziz, and Y. Brechet. Compositionally Graded Steels: A Strategy for Materials Development. *Advanced Engineering Materials*, v 11, n 12, p 992-999, December 2009, Print.
- [5] F. Lefevre-Schlick, O. Bouaziz, Y. Brechet, and J. Embury. Compositionally Graded Steels: The Effect of Partial Decarburization on the Mechanical Properties of Spherodite and Pearlite. *Materials Science and Engineering: A* 491.1-2 (2008): 80-87. Print.
- [6] Y. Cao. Surface Hardening of Austenitic Stainless Steels via Low-temperature Colossal Supersaturation. *Thesis. Case Western Reserve University*, 2003. Print.

[7] R. Roumina, G. Xu and B. Chehab. Mechanical Properties of Graded 4340. McMaster University, *Graded Materials Workshop*, 9 October 2010. Speaker: Hatem Zurob.

[8] J.P. Masse. Part III : Architected Materials. McMaster University, *Internal Report*, September 2009.

[9] E. Baerlecken, et al. Investigations Concerning the Transformation Behaviour, the Notched Impact Toughness and The Susceptibility to Intercrystalline Corrosion of Iron-Chromium Alloys with Chromium Contents to 30%. *Stahl Eisen*, vol. 81, no 12, pp. 768-778, 8 June 1961. Print.

[10] C.R. Johnson, and S.J. Rosenberg. Constitution Diagram for 16% Cr-2%Ni Stainless Steel. *Trans. Am. Soc. Met.*, vol. 55, pp. 277-286, 1962. Print.

[11] K. Bungardt, E. Kunze and E. Horne. Structure of the System Fe-Cr-C. *Archiv Eisenhuettenwes*, vol. 29, pp. 193-203, March 1958. Print.

[12] P.T. Lovejoy. Structure and Constitution of Wrought Martensitic Stainless Steels. In *Handbook of Stainless Steels*. D. Peckner, I.M. Bernstein, Eds.; McGraw-Hill Companies: New York, 1977. Print.

[13] M. Yaso, S. Morito, T. Ohba, K. Kubota. Microstructure of martensite in Fe-C-Cr steel *Materials Science and Engineering: A*, vol. 481-482, pp.770-773, May 2008. Print.

- [14] C. Garcia de Andres and L.F. Alvarez. Optimization of the properties obtained by quenching in martensitic stainless steel X30-40Cr13 and X40-60CrMoV14. *Journal of Materials Science*, vol. 28, pp. 1264-1268, 1993. Print.
- [15] C. Garcia de Andres, G. Caranua and L.F. Alvarez. Control of $M_{23}C_6$ carbides in 0.45C-13Cr martensitic stainless steel by means of three representative heat treatment parameters. *Materials Science and Engineering: A*, vol. 241, pp.211-215, 1998. Print.
- [16] S. Floreen. The Properties of Low Carbon Iron-Nickel Chromium Martensites. *Trans. Am. Inst. Min. Metall. Pet. Eng.*, vol. 236, pp. 1429-1440, 1966. Print.
- [17] L.C. Lim, M.O. Lai, et al. Tempering of AISI 403 Stainless Steel. *Materials Science and Engineering: A*, vol. 171, pp. 13-19, 1993. Print.
- [18] B. Miao, D.O. Northwood, et al. Microstructure of tempered AISI 403 stainless steel. *Materials Science and Engineering: A*, vol. 171, pp. 21-33, 1993. Print.
- [19] D.V. Malakhov. Mathematics of Decarburization. *Lecture: Mats 3T04*, CNH 106, Faculty of Engineering, McMaster University, Hamilton, Ontario, 2007. Electronic.
- [20] D.V. Malakhov and G.R. Purdy. Thermodynamic aspects and kinetic modeling of decarburization of steels in walking-beam furnaces. *5th ASM Heat Treatment and Surface Engineering Conference in Europe*, Göteborg, Sverige, 2000.

[21] A. Van der Ven and L. Delaey. Models For Precipitate Growth During The $\gamma \rightarrow \alpha + \gamma$ Transformation in Fe-C and Fe-C-M Alloys. *Progress in Materials Science*, vol. 40, pp 181-264, 1996.

[22] H. Oikawa, J.F. Remy and A.G. Guy. Decarburization of Alloy Steels. *Transactions of the ASM*, vol. 61, pp. 110-114, 13 November 1967. Print.

[23] I.Pyyry and P. Kettunen. Decarburization of Plain Carbon Steels. *Scandinavian Journal of Metallurgy*, vol. 2 pp. 265-268, 1973. Print.

[24] D.S. Wilkinson. *Mass Transport in Solids and Fluids*. Cambridge: Univeristy Press, 2000, pp. 60–65. Print.

[25] J.J. Hoyt. *Phase Transformations*. McMaster Innovation Press, 2010. ISBN: 978-1-926633-28-2

[26] A.R. Marder, S.M. Perpetua, J.A. Kowalik and E.T. Stephenson. The Effect of Carbon Content on the Kinetics of decarburization in Fe-C Alloys. *Metallurgical Transactions A*, vol. 16A, pp. 1160-1163, June 1985. Print.

[27] ArcelorMittal - Stainless Europe. Table of Stainless Grades. *Website: <http://www.arcelormittal.com/stainlesseurope/>*, April 2008. Electronic Resource.

[28] D. Radisson. Study of Graded Martensitic Stainless Steel. *Unpublished Internship Report*, McMaster University, 2010.

- [29] X. Liang. Structural and mechanical properties of fe-mn alloys. *Master's thesis*, McMaster University, 2008.
- [30] R.R. Blackwood, L.M. Jarvis et al. Conditions Leading to Quench Cracking Other Than Severity of Quench. *Heat Treating 1998: Proceedings of the 18th Conference (ASM International)*, pp. 575-585, 1999.
- [31] A. Beche. Study of ferrite growth in Fe-C-X alloys by decarburisation, *Final Project Report*, 2007.
- [32] O. Kolednik. The yield stress gradient effect in inhomogeneous materials. *International Journal of Solids and Structures*, vol. 37, pp.781-808, 2000. Print.
- [33] M.F. Ashby and David R. H. Jones. *Engineering Materials 1: an Introduction to Properties, Applications and Design*. 3rd ed. Amsterdam: Elsevier Butterworth-Heinemann, 2005. 177. Print.
- [34]H. Bhadeshia. *Bainite in Steels: Transformations, Microstructure and Properties*. 2nd ed. London: IOM Communications, 2001. 304. Print.
- [35] D.A. Jones. *Principles and Prevention of Corrosion*. 2nd ed. Upper Saddle River, NJ: Prentice Hall, 1996. Print.
- [36] S. Suresh and A. Mortensen. *Fundamentals of Functionally Graded Materials: Processing and Thermomechanical Behaviour of Graded Metals and Metal-ceramic Composites*. London: IOM Communications, 1998. Print.

- [37] B. Kung. Influence of decarburization on mechanical properties of Fe-Mn-C alloys. *McMaster University: Internal Report*, 2008.
- [38] S. Crawford. Modeling Decarburization of Fe-C alloys. *Internal Report: McMaster University*, 2010.
- [39] S. Crawford. Optimizing Carbon Distribution in a Functionally Graded Material. *Internal Report: McMaster University*, 2010.
- [40] G.A. Roberts., George Krauss, and Richard Kennedy. *Tool steels*. 5th ed. Materials Park, OH: ASM International, 1998. Print.
- [41] W.D. Callister. *Materials Science and Engineering: an Introduction*. 6th ed. New York: John Wiley & Sons, 2003. Print.
- [42] K. Hashiguchi, J.S. Kirkaldy, T. Fukuzumi and V. Pavaska. *Prediction Of The Equilibrium, Paraequilibrium and No-Partition Local Equilibrium Phase Diagrams for Multi-Component Fe-C Base Alloys*, CALPHAD Vo1.8, No.2, pp. 173-186, 1984.
- [43] G.R. Purdy, D.H. Weichert, J.S. Kirkaldy. *The growth of proeutectoid ferrite in ternary iron-carbon-manganese austenite*, Transactions of the metallurgical society of AIME, volume 230, pp.1025-1034, 1964.
- [44] R. Adharapurapu, and D. Kumar, et al. *Chromia-Assisted Decarburization of W-Rich Ni-Based Alloys in Impure Helium at 1273 K*, Metallurgical and Materials Transactions A, volume 42A, 1229-1244, 2011. Print.